Long-Baseline Neutrino Experiment (LBNE) Project

Conceptual Design Report

Volume 3: Detectors at the Near Site

March 13, 2012

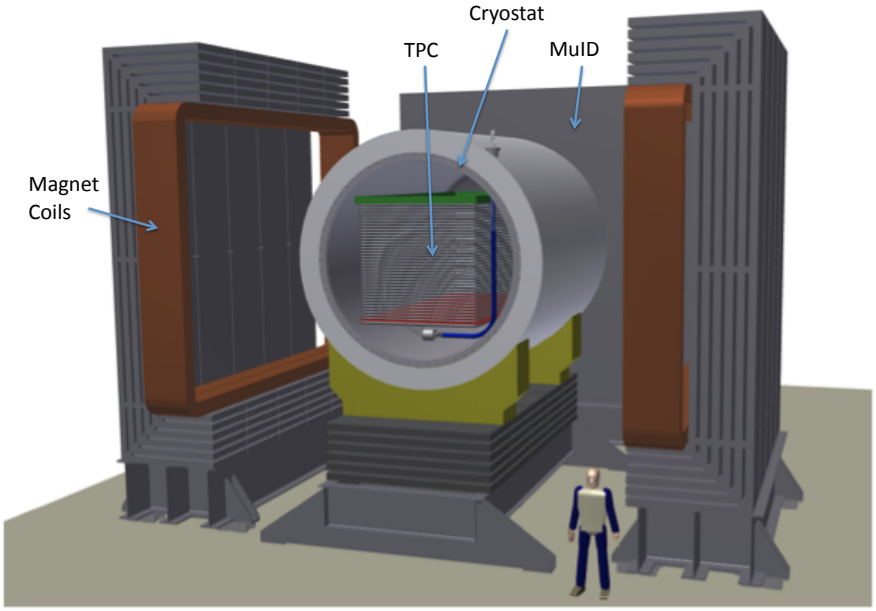

Contents

Acronyms, Abbreviations and Units

ADC	analog-to-digital converter
ASIC	application-specific integrated circuit
B-GDAQ	beamline global data acquisition
BEB	back-end board
BLM	beamline-measurement system
CC	charged current (interaction)
CCQE	charged current quasi-elastic (interaction)
CDR	Conceptual Design Report
CERN	European Organization for Nuclear Research
CNGS	Neutrino Beam to Gran Sasso (at CERN)
CP	charge parity
DAQ	data acquisition
DOE	Department of Energy
DUSEL	Deep Underground Science and Engineering Laboratory
ECAL	electromagnetic calorimeter
ESH	Environment, Safety and Health
eV	electron-Volt, unit of energy (also keV, MeV, GeV, etc.)
FEB	front-end board
FGT	Fine-Grained Tracker
FPGA	field-programmable gate array

FRA	Fermi Research Alliance
g-2	the New Muon g-2 Experiment at Fermilab
GDAQ	global data acquisition
GPS	Global Position System
HEP	high energy physics
ICARUS	Imaging Cosmic And Rare Underground Signals (experiment at LNGS)
K2K	"From KEK to Super–Kamiokande," long-baseline neutrino-oscillation experiment
LANL	Los Alamos National Laboratory
LAr	liquid argon
LAr-FD	(LBNE) Liquid Argon Far Detector
LAr1	one-kiloton LAr prototype for LAr-FD
LArTPC	Liquid Argon Time Projection Chamber
LArTPCT	Liquid Argon Time Projection Chamber Tracker system
LBNE	Long-Baseline Neutrino Experiment
LHC	Large Hadron Collider (at CERN)
LNGS	Gran Sasso National Laboratory
m	meter (also nm, micron, mm, cm, km)
M-GDAQ	master global data acquisition
MicroBooNE	A 100-ton LArTPC located along Fermilab's Booster neutrino beamline
MINERvA	A neutrino-scattering experiment that uses the NuMI beamline at Fermilab
MiniBooNE	Booster Neutrino Experiment (at Fermilab)
MINOS	Main Injector Neutrino Oscillation Search experiment at Fermilab
MIPP	Main Injector Particle Production Experiment (at Fermilab)
MPPC	multi-pixel photon counter
MuID	muon-identification detector

N-GDAQ	neutrino global data acquisition
NA61	NA61/SHINE, experiment at CERN that studies hadron production in hadron-nucleus and nucleus-nucleus collisions
NC	neutral current (interaction)
ND	(Near Site) neutrino detector
NDC	Near Detector Complex; refers to the subproject
NOMAD	Neutrino Oscillation Magnetic Detector, experiment at CERN
NOvA	NuMI Off-Axis Neutrino Appearance experiment at Fermilab
NuMI	Neutrino beam to MINOS
P5	Particle Physics Project Prioritization Panel
PMT	photomultiplier tube
QE	quasi-elastic (interaction)
STT	straw-tube tracker
Super-K	Super-Kamiokande, a neutrino detector in Japan
T	Tesla; unit of magnetic field strength
T2K	Tokai-to-Kamioka, a long-baseline neutrino oscillation experiment in Japan
T2K ND280	Near Detector of the Tokai-to-Kamioka (T2K) experiment, located 280m from the beamline target
TDC	time-to-digital converter
TFB	T2K front-end board
TPC	time projection chamber
TR	transition radiation
TRIP-t	Trigger and Pipeleine with timing (full custom ASIC designed at Fermilab)
UA1	Experiment at CERN that ran from 1986 to 1993
UV	ultra-violet
V	Volt
W	watt (also mW, kW, MW)

WBS	Work Breakdown Structure
WLS	wavelength shifter

List of Figures

List of Tables

1 Introduction

1.1 Introduction to the LBNE Project

The Long-Baseline Neutrino Experiment (LBNE) Project team has prepared this Conceptual Design Report (CDR) which describes a world-class facility to enable a compelling research program in neutrino physics. The ultimate goal in the operation of the facility and experimental program is to measure fundamental physical parameters, explore physics beyond the Standard Model and better elucidate the nature of matter and antimatter.

Although the Standard Model of particle physics presents a remarkably accurate description of the elementary particles and their interactions, it is known that the current model is incomplete and that a more fundamental underlying theory must exist. Results from the last decade, revealing that the three known types of neutrinos have nonzero mass, mix with one another and oscillate between generations, point to physics beyond the Standard Model. Measuring the mass and other properties of neutrinos is fundamental to understanding the deeper, underlying theory and will profoundly shape our understanding of the evolution of the universe.

1.1.1 About this Conceptual Design Report

The LBNE Conceptual Design Report is intended to describe, at a conceptual level, the scope and design of the experimental and conventional facilities that the LBNE Project plans to build to address a well-defined set of neutrino-physics measurement objectives. At this Conceptual Design stage the LBNE Project presents a *Reference Design* for all of the planned components and facilities, and alternative designs that are still under consideration for particular elements. The scope includes

- an intense neutrino beam aimed at a far site
- detectors located at the near site just downstream of the neutrino source

- a massive neutrino detector located at the far site
- construction of conventional facilities at both the near and far sites

The selected near and far sites are Fermi National Accelerator Laboratory (Fermilab), in Batavia, IL and Sanford Underground Laboratory at Homestake (Sanford Laboratory), respectively. The latter is the site of the formerly proposed Deep Underground Science and Engineering Laboratory (DUSEL) in Lead, South Dakota.

This CDR is organized into six stand-alone volumes, one to describe the overall LBNE Project and one for each of its component subprojects:

- Volume 1: The LBNE Project
- Volume 2: The Beamline at the Near Site
- Volume 3: Detectors at the Near Site
- Volume 4: The Liquid Argon Detector at the Far Site
- Volume 5: Conventional Facilities at the Near Site
- Volume 6: Conventional Facilities at the Far Site

Volume 1 is intended to provide readers of varying backgrounds an introduction to LBNE and to the following volumes of this CDR. It contains high-level information and refers the reader to topic-specific volumes and supporting documents, also listed in Section 1.1.5. Each of the other volumes contains a common, brief introduction to the overall LBNE Project, an introduction to the individual subproject and a detailed description of its conceptual design.

1.1.2 LBNE and the U.S. Neutrino-Physics Program

In its 2008 report, the Particle Physics Project Prioritization Panel (P5) recommended a world-class neutrino-physics program as a core component of the U.S. particle physics program [1]. Included in the report is the long-term vision of a large detector at the Sanford Laboratory and a high-intensity neutrino source at Fermilab.

On January 8, 2010, the Department of Energy (DOE) approved the Mission Need for a new long-baseline neutrino experiment that would enable this world-class program and firmly establish the U.S. as the leader in neutrino science. The LBNE Project is designed to meet this Mission Need.

With the facilities provided by the LBNE Project, the LBNE Science Collaboration proposes to mount a broad attack on the science of neutrinos with sensitivity to all known parameters in a single experiment. The focus of the program will be the explicit demonstration of leptonic CP violation, if it exists, by precisely measuring the asymmetric oscillations of muon-type neutrinos and antineutrinos into electron-type neutrinos and antineutrinos.

The experiment will result in the most precise measurements of the three-flavor neutrino-oscillation parameters over a very long baseline and a wide range of neutrino energies, in particular, the CP-violating phase in the three-flavor framework. The unique features of the experiment – the long baseline, the broad-band beam, and the high resolution of the detector – will enable the search for new physics that manifests itself as deviations from the expected three-flavor neutrino-oscillation model.

The configuration of the LBNE facility, in which a large neutrino detector is located deep underground, could also provide opportunities for research in other areas of physics, such as nucleon decay and neutrino astrophysics, including studies of neutrino bursts from supernovae occuring in our galaxy. The scientific goals and capabilities of LBNE are outlined in Volume 1 of this CDR and described fully in the LBNE Case Study Report (Liquid Argon TPC Far Detector) [2] and the 2010 Interim Report of the Long-Baseline Neutrino Experiment Collaboration Physics Working Groups [3].

1.1.3 LBNE Project Organization

The LBNE Project Office at Fermilab is headed by the Project Manager and assisted by the Project Engineer, Project Systems Engineer and Project Scientist. Project Office support staff include a Project Controls Manager and supporting staff, a Financial Manager, an Environment, Safety and Health (ES&H) Manager, a Computing Coordinator, Quality Assurance and Risk Managers, a documentation team and administrative support. The Beamline, Liquid Argon Far Detector and Conventional Facilities subprojects are managed by the Project Office at Fermilab, while the Near Detector Complex subproject is managed by a Project Office at Los Alamos National Laboratory (LANL).

More information on Project Organization can be found in Volume 1 of this CDR. A full description of LBNE Project management is contained in the LBNE Project Management Plan [4].

1.1.4 Principal Parameters of the LBNE Project

The principal parameters of the major Project elements are given in Table 1–1.

Table 1–1: LBNE Principal Parameters

Project Element Parameter	Value
Near- to Far-Site Baseline	1,300 km
Primary Proton Beam Power	708 kW, upgradable to 2.3 MW
Protons on Target per Year	6.5×10^{20}
Primary Beam Energy	60 – 120 GeV (tunable)
Neutrino Beam Type	Horn-focused with decay volume
Neutrino Beam Energy Range	0.5 – 5 GeV
Neutrino Beam Decay Pipe Diameter × Length	4 m × 200 m
Near Site Neutrino Detector Type	Liquid Argon Time Projection Chamber (LArTPC) Tracker
Near Site Neutrino Detector Active Mass	18 ton
Far Detector Type	LArTPC
Far Detector Active (Fiducial) Mass	40 (33) kton
Far Detector Depth	1480 m

1.1.5 Supporting Documents

A host of information related to the CDR is available in a set of supporting documents. Detailed information on risk analysis and mitigation, value engineering, ES&H, costing, project management and other topics not directly in the design scope can be found in these documents, listed in Table 1–2. Each document is numbered and stored in LBNE's document database, accessible via a username/password combination provided by the Project. Project documents stored in this database are made available to internal and external review committees through Web sites developed to support individual reviews.

Table 1–2: LBNE CD-1 Documents

Title	**LBNE Doc Number(s)**
Acquisition Plan	5329
Alternatives Analysis	4382
Case Study Report; Liquid Argon TPC Detector	3600
Configuration Management Plan	5452
DOE Acquisition Strategy for LBNE	5442
Integrated Environment, Safety and Health Management Plan	4514
LAr-FD Preliminary ODH Analysis	2478
Global Science Objectives, Science Requirements and Traceback Reports	4772
Preliminary Hazard Analysis Report	4513

Preliminary Project Execution Plan	5443
Preliminary Security Vulnerability Assessment Report	4826
Project Management Plan	2453
Project Organization Chart	5449
Quality Assurance Plan	2449
Report on the Depth Requirements for a Massive Detector at Homestake	0034
Requirements, Beamline	4835
Requirements (Parameter Tables), Far Detector	3747 (2843)
Requirements, Far Site Conventional Facilities	4408
Requirements, Near Detectors	5579
Requirements, Near Site Conventional Facilities	5437
Risk Management Plan	5749
Value Engineering Report	3082
Work Breakdown Structure (WBS)	4219

1.2 Introduction to the LBNE Near Detectors

The LBNE Near Detector Complex (NDC) subproject consists of the detectors and program to make the measurements relevant to minimizing the systematic uncertainties on the long-baseline oscillation program and to thus maximize the oscillation-physics potential of the Far Detector.

In addition to the technical components, the work needed to define the baseline design is crucial as the LBNE NDC has several design alternatives that will be carried beyond CD-1. Unlike the Far Detector, the task of the Near Detectors is not to maximize their own capability, but rather design the technical components to meet the requirements of the long-baseline neutrino-oscillation analyses for the lowest possible cost. With that in mind, it is also important that the Near Detectors not limit the sensitivity of LBNE's long-baseline neutrino-oscillation measurements. They should, therefore, be useful for analyzing electron-neutrino appearance, the primary oscillation channel and muon-neutrino disappearance.

1.2.1 Reference Design

The set of detector systems for the Near Detectors reference design consists of a beamline-measurements system (BLM) and a neutrino-detection system (ND for "neutrino detectors"). The Near Detectors will be located at the Near Site (Fermilab), downstream of the beamline. The BLM will be located in the region of the Absorber Complex at the downstream end of the decay region to measure the muon fluxes from hadron decay. The absorber itself is part of the Beamline subproject and is discussed in Volume 2 of this CDR. The neutrino detector will be placed in the Near Detector Hall, 450 m downstream of the target, and underground. Figure 1–1 shows an aerial-view layout of the Beamline and Near Detectors on the Fermilab site. The conventional facilities for the Near Site are described in Volume 5 of this CDR.

This BLM system is intended to determine the neutrino fluxes and spectra and to monitor the beam profile on a spill-by-spill basis, and will operate for the life of the experiment.

Figure 1–2 shows the downstream side of the absorber and a conceptual layout of the BLM muon systems. The first set of muon measurement devices, from left to right, is the 5 $\times$ 5 ion-chamber array that is mounted directly to the rear wall of the absorber. Following that, a set of three variable-pressure, gas Cherenkov counters, and finally a set of stopped-muon counters interspersed between walls of steel "blue blocks". The blue blocks are there to provide several depths at which to monitor the stopped muons as they range out in the material.

The reference-design Neutrino Measurements system technology is a liquid-argon-filled time projection chamber tracker (LArTPCT), matching the interaction material in the LAr-FD

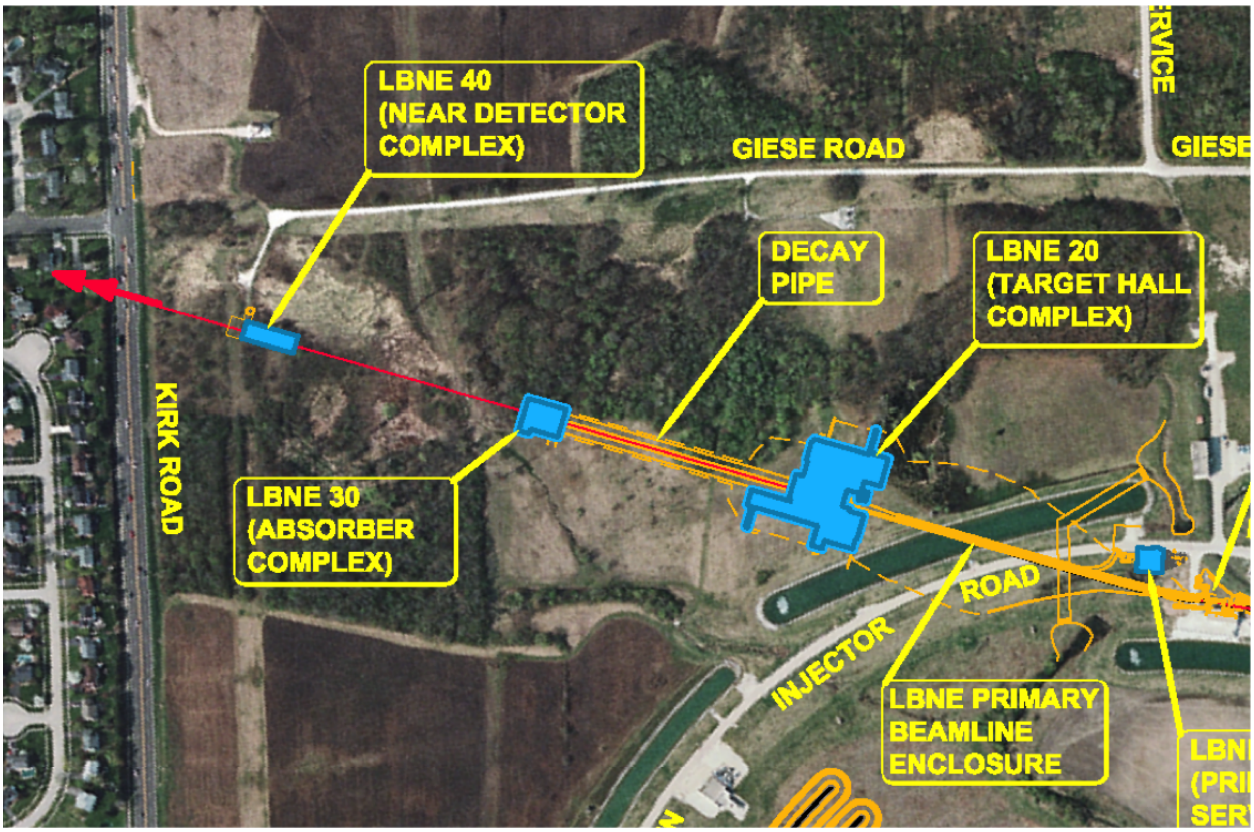

Figure 1–1: Layout of the LBNE Near Detector Complex

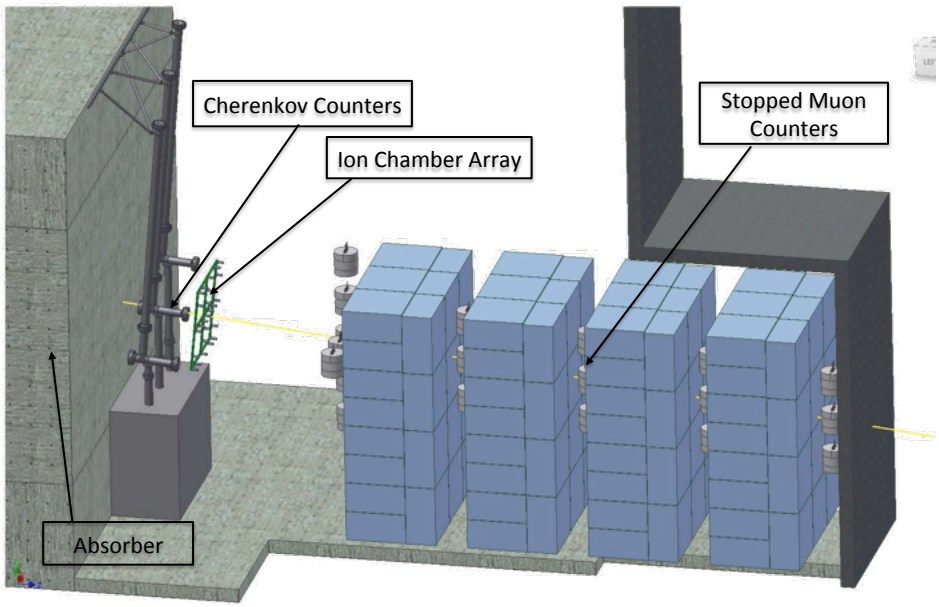

Figure 1–2: A model of the beamline-measurement systems showing the conceptual layout of the three muon subsystems downstream of the absorber. The beam enters from the left.

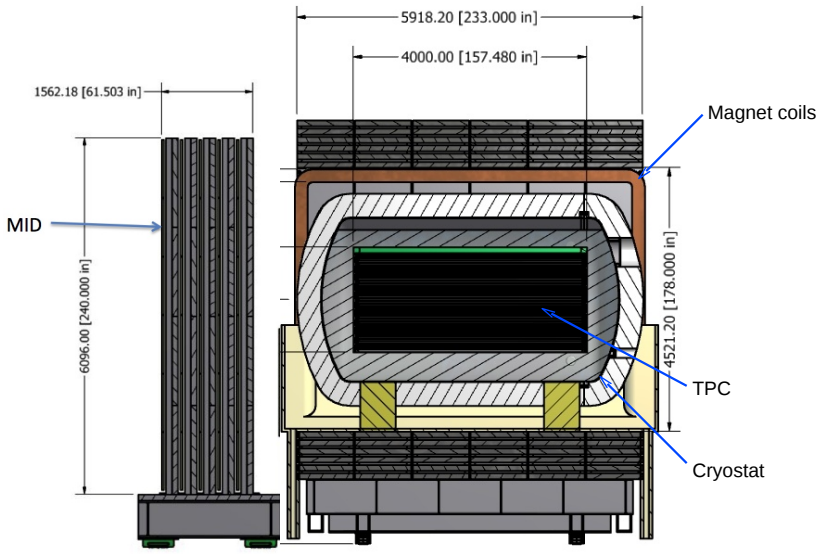

Figure 1–3: A schematic drawing of the liquid argon TPC tracker, the neutrino-detection system reference design

(described in Volume 4 of this CDR). The LArTPCT will consist of a 1.8-m × 6-m × 1.8-m × 4-m TPC and a 2.7-m-diameter × 5-m-long LAr cryostat inside of a large dipole magnet.

This system is intended to constrain (place limits on) or measure the various neutrino fluxes and spectra and to measure the neutrino-interaction channels important for predicting the signals and backgrounds at the Far Site. Deficits or enhancements of expected interaction-channel rates (measured at the LAr-FD), will constitute evidence of neutrino appearance, disappearance or oscillation.

1.2.2 Motivation

LBNE will measure neutrino oscillations by making high-statistics and high-precision measurements in the Far Detector. In order to achieve the ultimate neutrino oscillation sensitivity, the LBNE neutrino-detector group must be able to accurately and precisely predict signal and background events in the Far Detector. If neutrino event rates observed in the Near Detectors are different in the Far Detector, it will be evidence of neutrino oscillations. Due to large neutrino cross section uncertainties in the few-GeV energy regime where LBNE will operate, predicting the signal and background in the Far Detector is a challenge. It is, therefore, crucial to measure the neutrino fluxes and interaction channels at a near site – before the fluxes have been affected significantly by neutrino oscillations. A key challenge is

addressing any differences in rate and topology between neutrino and antineutrino events. In addition, the neutrino-detection system must measure the intrinsic ν_e background in the beam with sufficient precision to subtract it at the Far Site. Hadron production models important for simulating hadron propagation and interaction in the target and horn materials are not well constrained, making measurements of particles in the decay region as well as external measurements of hadron production and propagation in the target and horn materials desirable.

TPCs are the detectors of choice for low-rate, large-volume, high-precision particle physics experiments due to their excellent 3D position resolutions and particle identification capabilities in large volumes. In addition to generating detailed event topologies and measurements of particle kinematics, dE/dx (energy loss as a function of distance in material) measurements allow an LArTPCT to distinguish electrons, muons, photons, kaons, pions and protons over a wide range of energies.

Before discussing how detectors respond, it is useful to explain the terminology of neutrino event types. Neutrino events detected in experiments like LBNE are often categorized according to the particle mediating the interaction. The classification terminology arose from terms used in the Standard Model, for example to discuss the participation of heavy bosons in interactions. So the term (used below, and throughout this document) "neutral current process" (NC) refers to an interaction which is mediated by the neutral boson Z^o. Similarly, a "charged current" (CC) interaction involves a postive or negative charged W boson. A "quasi-elastic" (QE) event is one in which the neutrino scatters from a nucleon in a nucleus, making the kinematics of the collision more complex. Further, event categories combining these features, such as "charged current, quasi-elastic" (CCQE) are of great interest, as discussed below.

A primary science objective of LBNE is to make precise measurments of the parameters that govern $\nu_\mu \rightarrow \nu_e$ oscillations. These parameters probe CP violation in the neutrino sector and determine the neutrino mass hierarchy. The LArTPCT at the near site must measure NC, CC, CCQE, etc., events in the range of 200 MeV to 6 GeV. NC events containing π^0s are the dominant source of background from NC interactions. The π^0 decays to two gammas which convert to e^+e^- pairs and initiate an electromagnetic shower that can be difficult to distinguish from an electron shower. Excellent μ/e separation is required to enable the distinction of ν_μ and ν_e CC interactions. In addition to measurements of the CP parameters, LBNE will search for physics beyond the standard model with high precision measurements of the parameters Δm^2_{32} and $\sin^2 2\theta_{23}$ in ν_μ and $\bar{\nu}_\mu$ long baseline oscillations. These measurements require high-purity identification of ν_μ CC interactions for which high-precision separation of $\mu/\pi/p^+$ is necessary. The strength of the LArTPCT is the ability to use detailed event topology, particle kinematics, and dE/dX to differentiate ν_e, ν_μ CC and NC π^0 event classes with high purity and efficiency.

The LArTPCT will be able to detect low-momentum charged pions, enabling it to access an energy region below the Cherenkov production threshold (a primary advantage of LArTPC

technology over water Cherenkov detectors). If a pion absorbed in a nucleus causes baryons to be ejected from the nucleus, then the TPC should be able to measure the protons. How strong a correlation one can make between the outgoing baryon momenta, the charged lepton momentum and the neutrino energy is not yet clear. However, if any of the outgoing baryons are neutrons, it will be difficult to measure their momenta with precision (if at all). As research and development progresses, this issue and its impact on oscillation analyses must be studied in more detail.

Not only are there many CC and NC processes that can generate background for oscillation analyses in liquid argon detectors, but the uncertainties in their cross sections and momenta of the outgoing particles are large. Pion production in the resonance regime is a prime example. Although the uncertainties on pion production are large, it is at least known that these processes exist. However, there also might be surprises. MiniBooNE is a short-baseline oscillation experiment that measures neutrinos in a similar energy regime to LBNE. MiniBooNE measures an excess of electron-like events for reconstructed neutrino energies of below 475 MeV. Because the experiment detects neutrinos predominantly by Cherenkov light in oil, it cannot distinguish between electrons and gamma rays.

At present, it is not known whether this unexplained excess of electron-like events is due, for example, to a ν_e charged-current interaction or to a ν_μ neutral-current interaction with an outgoing photon; however, it will be very important for the neutrino detector to be able to distinguish these event types.

The difficulties discussed above can be mitigated by a thorough near-detector program of measurements in order to be able to predict the neutrino spectra at the Far Site under all interesting oscillation scenarios as well as the corresponding event rates and topologies.

1.2.3 Historical Precedents

The conceptual design draws heavily on the design and experience of other long-baseline neutrino experiments. The K2K [5] experiment was the first long-baseline experiment constructed with a man-made muon-neutrino beam. It finished running in December of 2004. There are three long-baseline neutrino experiments in the world currently running, MINOS [6], T2K and CNGS [7]. All are horn-focused, predominantly muon (anti)neutrino beams. The beam for MINOS is produced at Fermilab and aimed at an underground site in Minnesota, the beam for T2K is produced in Tokaimura, Japan and directed towards the Super-Kamiokande detector in Gifu Prefecture, Japan, and the beam for CNGS is produced at CERN in Switzerland and pointed at detectors in the Gran Sasso National Laboratory in Italy. In addition, the MiniBooNE [8] and Minerνa [9] experiments collect data that are useful for planning the LBNE ND.

These prior long-baseline experiments inform the design of the LBNE neutrino detector in

two ways. First, the neutrino-detector group has analyzed their approaches to neutrino-oscillation analysis to understand how they used near-detector data in their analyses.

Secondly, this group uses topologies from these experiments to better determine what background processes the neutrino detector must measure. The designs we are developing are based on the best information in hand at the moment. It is important to understand that results anticipated from T2K and Minerνa may reduce the uncertainties on some of the problematic processes that will be measured.

1.2.4 Challenges of Searching for Neutrino-antineutrino Asymmetries

Unlike experiments that simply look for ν_e appearance, LBNE will endeavor to measure the difference in probability of electron-neutrino appearance in a predominantly muon-neutrino beam and electron-antineutrino appearance in a largely muon-antineutrino beam. Antineutrino beams are generated with the same beam components as neutrino beams: protons impinge on a target generating showers of mesons that are magnetically focused down a decay pipe. To generate an antineutrino beam, the magnetic horns are pulsed with opposite polarity – focusing mesons of the opposite sign as for the neutrino-beam case. Ideally, one might wish to generate the antineutrino beam by focusing antiprotons on an antimatter target, but the technical challenges of such an enterprise are left for future projects.

The resultant neutrino beams and antineutrino beams therefore have slightly different energy spectra from one another and rather different quantities of wrong-sign background, as well as a different energy dependence of the wrong-sign background. Neutrinos and antineutrinos have different charged-current cross sections with matter. When one convolves the fluxes with the charged-current cross sections, the interaction rates of signal and background events differ significantly. The energy dependence also changes. As such, it is critical that the near neutrino detectors be able to predict the signal and background for neutrino and antineutrino events separately in each beam mode.

1.2.5 Structure of this document

In the following pages, the conceptual design for the LBNE Near Detectors is introduced.

Chapter 2 *Measurement Strategy* discusses the simulations required to understand what background and signal processes must be measured to optimize the sensitivity of the electron-(anti)neutrino appearance analyses and the muon-(anti)neutrino disappearance analyses. In addition, work to understand the impact of the non-flat far/near ratio of neutrino spectra is discussed. The work will lead to firm requirements on our measurements of the muon-(anti)neutrino and electron-(anti)neutrino fluxes. Additionally, detailed requirements on the

measurement of neutrino cross sections and the kinematic distributions of hadrons after final-state interactions will be derived.

The focus of the technical system described in Chapter 3 *Near Detector Beamline Measurements* is on measuring muons after the absorber at the end of the decay region. The muons are created in the same meson decays as the neutrinos. As such, the profile of the muon beam and the profile of the neutrino beam are strongly correlated. One of the technical subsystems described here is designed to measure muon intensities after the absorber to obtain a spill-by-spill profile of the neutrino beam. Additionally, the muon-energy spectrum and the neutrino-energy spectrum are correlated. Two detector systems described here are designed to measure the muon-energy spectrum and thus extract the neutrino-energy spectrum.

The central focus of the NDC subproject is on neutrino measurements. The subsystems described in Chapter 4 *Neutrino Detectors* are designed to make a plethora of neutrino measurements. We present the LArTPCT reference design, similar to MicroBooNE's, for the neutrino detector. The detector apparatus will be enclosed in a wide-aperture dipole magnet based on the design of the CERN UA1 [10] magnet. The magnetic field will enable charge-sign determination of particles from their bend direction as they traverse the detector. Interspersed in the magnet yoke and surrounding the magnet will be a plastic-scintillator muon-identification system (MuID). A fine-grained tracker with water or argon target material is discussed as an alternative.

The magnet described in Chapter 5 *Near Detector Magnet* is the UA1-design large-aperture magnet, and can be used for either the reference-design LArTPCT or the alternative fine-grained tracker (FGT).

Each subsystem in the NDC will have its own data acquisition (DAQ) system. The system described in Chapter 6 *Near Detector Global DAQ and Global Computing*, on the other hand, is what ties all of the subsystems together. The Global DAQ collects data, builds events, applies clock and GPS time-stamps and communicates with the rest of the experiment. It receives and transmits global triggers to each near-detector subsystem.

The computing needs for the slow control will be developed after CD-1. Offline computing needs for simulation are provided by Fermilab, Brookhaven, LANL and several university groups.

1.3 Participants

The design for the LBNE Near Detector Complex (NDC) is being carried out by an LBNE subproject team, headed at Los Alamos National Laboratory (LANL) but also with participants from universities, in conjunction with outside contractors. The Near Detectors (for beamline and neutrino measurements) are planned for construction at the Fermilab site,

which is managed by the Fermi Research Alliance (FRA).

The LBNE NDC is managed by the Work Breakdown Structure (WBS) Level 2 Manager for the Near Detector Complex subproject. The supporting team includes a WBS Level 3 Manager for each of the NDC's principal systems, Measurement Strategy, Beamline Measurement System and Neutrino Measurements, Magnets, Global Data Acquisition and Computing, as illustrated in Figure 1–4.

The Conventional Facilities Level 3 Near Site Manager is the LBNE Project liaison with the NDC subproject to ensure the subproject's requirements are met; this person is responsible for all LBNE conventional facilities scope at the Near Site.

Interaction between Fermilab facility engineers, LBNE NDC design teams, and design consultants has been done via weekly telephone conferences, periodic design interface workshops, and electronic mail. An integration document resulting from these discussions will allow the NDC subproject team to coordinate activities and ensure that the design efforts remain on track and that requirements are met.

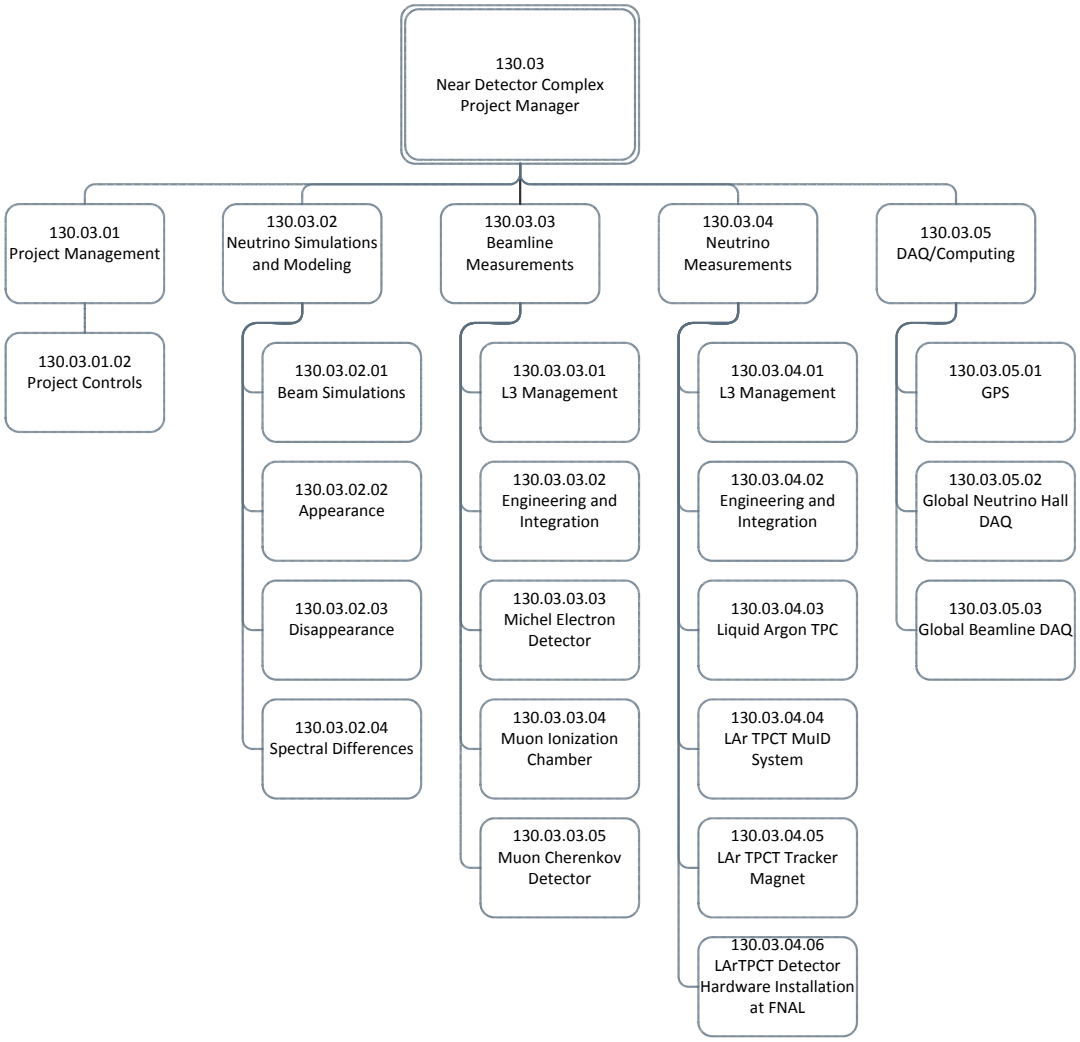

Figure 1–4: Organization chart for the Near Detector Complex subproject

2 Measurement Strategy (WBS 130.03.02)

2.1 Introduction

The main purpose of the LBNE Near Detectors is to minimize systematic uncertainties present in the analysis of far detector data and provide a direct measurement of the unoscillated event spectrum, independent of Monte Carlo prediction. The Near Detectors should therefore be capable of sufficiently measuring, constraining and understanding signal and background processes relevant for the ν_e appearance and ν_μ disappearance analyses such that their uncertainty is not a dominant source of error. This chapter describes the strategy for such measurements.

2.2 Design Considerations

In addition to neutrino detectors the Near Detectors include beamline monitor (BLM) detectors that measure the tertiary muon flux in order to reduce the inherent neutrino flux and cross-section uncertainties that impact the oscillation-physics potential of the Far Detector. Because the neutrino energies at the Near and Far Detectors are different and cross sections are energy dependent, careful consideration of their contributions is required. The BLM detectors provide information on the LBNE neutrino flux and are discussed in Chapter 3. The neutrino detectors (ND) provide constraints on the neutrino cross sections (as well as the neutrino flux for certain interaction processes) and are discussed in more detail in Chapter 4. Generically, the neutrino detectors at the Near Site must:

- Include the same nuclear target as the Far Detector (This is to ensure that unnecessary uncertainty is not accrued from extrapolation between nuclei. Such extrapolations can be potentially large depending on the process and the nuclei involved.)
- Provide a sufficient mass of the nuclear target material to allow detailed study of backgrounds; matching Far Detector event rates would require only about 100 kg of material in the Near Detector, so greater amounts would serve to increase the rate of

rare or poorly understood events, which would be especially important for background processes

- Possess sufficient containment, resolution and tracking capability to separately identify classes of events of interest for the Far Detector analyses (This includes ν_μ and ν_e quasi-elastic (QE), ν_μ and ν_e charged current (CC), ν_μ non-QE, ν_μ neutral current (NC) π^0, and ν_μ NC γ interactions, in addition to their antineutrino counterparts.) Event containment implies an active detector volume several meters long.

- Include the means to separately identify neutrino and antineutrino interactions. (The fluxes and cross sections are different for neutrino and antineutrino scattering, so both must be known to ensure a successful measurement of CP-violating effects in the Far Detector. This will be particularly important for antineutrino running where the wrong-sign (neutrino) contamination is sizable.)

Together, this means that the Near Detectors must be able to separately identify and measure $\mu^\pm$, $e^\pm$ and photons with high precision over a broad energy and angular range. Furthermore, it is evident that the nuclear species (nucleus, isotopic species or nuclide) creating these events be clearly identified. These attributes will ensure few-%-level measurements of relevant processes in the LBNE Near Detectors for use in the Far Detector analyses.

2.3 Electron-neutrino Appearance (WBS 130.03.02.03)

One of the main goals of LBNE will be the identification of $\nu_\mu \rightarrow \nu_e$ and $\bar{\nu}_\mu \rightarrow \bar{\nu}_e$ oscillations. Measurement of this appearance rate will require identification of ν_e and $\bar{\nu}_e$ interactions as a function of neutrino energy in the Far Detector. The dominant backgrounds in such appearance searches arise from three main sources: intrinsic electron-neutrinos in the beam, neutral-current (NC) processes that can mimic an electron-neutrino signal and misidentified CC ν_μ interactions. The unprecedented precision of LBNE requires that these backgrounds be known at an extremely high level. Each of these three contributing backgrounds is discussed in further detail below.

Intrinsic electron-neutrinos in the beam are particularly threatening because they form an irreducible background to the ν_e and $\bar{\nu}_e$ appearance analyses. Uncertainty in their contribution to the beam can thus lead to a direct degradation of the oscillation sensitivity of the experiment. Electron-neutrinos are expected to comprise $\sim$1% of the LBNE beam and arise from three main sources: muon decays, charged-kaon decays and neutral-kaon decays. These sources populate different energy regions, with electron-neutrinos from muon decays typically contributing at lower energies than those from kaon decays. The Near Detectors will make a precise measurement of the ν_e and $\bar{\nu}_e$ content in the beam, hence directly constraining their content. In addition, information from high-statistics samples of muon-neutrino interactions in the Near Detectors can provide complementary information on the ν_e contamination in

the beam. Muon-neutrinos from pion decays can be used to constrain electron-neutrinos from muon decays, while higher-energy muon-neutrino events can provide additional information on electron-neutrinos from kaons.

Measurement of intrinsic electron-neutrinos is one of the most important functions of the Near Detector complex, as it is specific to the LBNE beam and constraints on the intrinsic electron-neutrino content cannot be obtained from other beamlines.

A second background to the ν_e- and $\bar{\nu}_e$-appearance measurements in LBNE arises from NC processes. The largest contribution comes from NC π^0 production, a process that historically has not been well measured at LBNE energies and is affected by poorly characterized final-state interactions. Reducing uncertainties on the NC π^0 contribution to the Far Detector analyses will require information from the Near Detectors.

NC events containing π^0s are the dominant source of background from NC interactions. The π^0 decays to two gammas which convert to e^+e^- pairs and initiate an electromagnetic shower that can be difficult to distinguish from an electron shower. Excellent μ/e separation is required to enable the distinction of ν_μ and ν_e CC interactions. In addition to measurements of the CP parameters, LBNE will search for physics beyond the standard model with high precision measurements of the parameters Δm^2_{32} and $\sin^2 2\theta_{23}$ in ν_μ and $\bar{\nu}_\mu$ long baseline oscillations. These measurements require high-purity identification of ν_μ CC interactions for which high-precision separation of $\mu/\pi/p^+$ is necessary. The strength of the LArTPCT is the ability to use detailed event topology, particle kinematics, and dE/dx to differentiate ν_e, ν_μ CC and NC π^0 event classes with high purity and efficiency.

One final background that must also be considered is that of misidentified CC ν_μ interactions. Although the potential to misidentify a ν_μ CC event as a ν_e signature is small, the high rate of ν_μ CC interactions means they will comprise an additional background to the ν_e-appearance searches and must be accounted for. Measuring the energy-dependence of ν_μ CC interactions in the Near Detectors will ensure that their content is predicted with high reliability at the Far Detector.

2.4 Muon-neutrino Disappearance (WBS 130.03.02.04)

Precise measurements of Δm^2_{32} and θ_{23} will be performed in the LBNE Far Detector by measuring distortions in the muon-(anti)neutrino spectra due to oscillations in both neutrino and antineutrino running. The level of precision required on the energy dependence of both signal processes (either CC or QE interactions) and potential background will eventually be determined by information from the Far Detector. These energy spectra are heavily influenced by nuclear effects that are unfortunately not well known at LBNE energies. To mitigate this, the Near Detectors will provide a direct measurement of the un-oscillated spectrum of CC ν_μ and $\bar{\nu}_\mu$ interactions on the same target material as the Far Detector. This ensures

that nuclear effects impacting the energy spectrum are the same between the Near and Far Detectors. Careful attention must be paid to both signal and background processes.

In order to reconstruct the energy of the incoming neutrino from the product of its interactions, QE interactions are usually chosen as the signal sample for ν_μ disappearance measurements. This is because the energy of the neutrino can be established to within 10% solely using the outgoing lepton. To verify the signal rate prior to oscillations, the Near Detectors will precisely measure the un-oscillated spectrum of muon-(anti)neutrino QE interactions on the relevant nuclear target. Backgrounds to the QE sample typically arise from other CC processes – the largest of which includes CC pion production channels in which the final state pion is absorbed in the initial target nucleus and is therefore not detected. Backgrounds from such non-QE interactions are particularly problematic, as they will lead to an incorrect neutrino energy. Because a larger fraction of energy is invisible in such interactions, the inferred neutrino energy can be significantly lower than the true neutrino energy, thus directly impacting the ability to measure oscillation parameters. For this reason, the number of non-QE interactions must be characterized in the LBNE beam over the appropriate energy range for the ν_μ disappearance measurement. Here, it is also important that background processes be constrained for the relevant nucleus because the fraction of non-QE events will vary according to the target material.

Thus, measurements of QE and non-QE interactions as a function of neutrino energy will be important for the Far Detector. It should be noted that an inclusive CC sample can also be potentially utilized as the signal sample for a ν_μ-disappearance measurement. This has the benefit of ensuring a higher-statistics, higher-purity signal sample; however, the determination of the incident neutrino energy will be less certain in this case. If such a sample is used, NC charged-pion interactions will form the dominant background and thus must be measured in the Near Detectors. In either case, the Near Detector Complex must have the capability to accurately measure both ν_μ non-QE and NC charged-pion interactions in order to respond to whatever measurement strategy the Far Detector may potentially employ.

Lastly, an additional background arises from the "wrong-sign" content in the beam. The term "wrong-sign" refers to antineutrinos in the neutrino beam or neutrinos in the antineutrino beam. For the determination of antineutrino-disappearance parameters, specific attention must be paid to the sizable contamination of neutrinos in the sample, a feature that every antineutrino beam must contend with. In LBNE, the event rate in antineutrino mode is predicted to be roughly half ν_μ and half $\bar{\nu}_\mu$ prior to oscillations. The sign-selection capabilities present in the Near Detectors will ensure proper constraint on this "wrong-sign" content. Given that the Far Detector will not be able to separate ν_μ from $\bar{\nu}_\mu$ and the fact that the ν_μ contamination results from unfocused meson decays in the beam (i.e. different meson production phase space than "right-sign" neutrinos), a Near Detector measurement of their content is essential.

3 Near Detector Beamline Measurements (WBS 130.03.03)

3.1 Introduction

This chapter defines the LBNE strategy for measurements of secondary beam particles in the decay tunnel, in the decay tunnel shielding, in the beam absorber, and behind the beam absorber. Those measurements are designed to provide constraints on the neutrino flux at the near and far detectors, and data on the pulse-to-pulse variation of the beam for beam diagnostic purposes. A description of equipment for monitoring the proton beam's interaction with the proton target can be found in Volume 2: The LBNE Beamline.

The measurements and apparatuses described in this chapter fall into two broad categories: equipment designed specifically for LBNE to detect muons exiting the decay tunnel, and external measurements of hadron production in support of the LBNE Project. The latter measurements are assumed to use hardware not part of the LBNE Project, although there could be significant use of normal DOE High Energy Physics (HEP) operational funds in support of the effort. Those measurements are connected to the near detector only in the assumptions of how well the neutrino flux is known.

3.2 Design Considerations

3.2.1 General

The requirements for the beamline measurements, as discussed in the NDC requirements documentation [11], are intimately related to how well the neutrino flux must be known. Given that LBNE does not have the luxury to construct identical Near and Far Detectors, a near-far comparison is more complicated than it was in the MINOS experiment [12], for example. Our working assumption is that the hadronic production will be measured at the 4–5% level in a separate experiment similar to MIPP-II [13] or NA61 [14].

While external hadron-production measurements can place strong constraints on the pion and kaon production in the target, they do not provide any confirmation of the simulation of other key features, such as the horn focusing, secondary interactions, and the pion scattering and absorption in the air-filled decay volume.

In addition to the external measurements, covered in Section 3.7, in order to confirm the simulation of the thick target, horn material, decay tunnel and absorber, it is desirable to constrain the flux by making independent measurements, again at the 4–5% level, of the muons that penetrate the absorber. It would not be practical to do this for all penetrating muons, but sufficient measurements at a few positions can be done in a cost-effective way.

The measurements of the absolute neutrino flux using muons are also very valuable to physics measurements in the Near Detector (such as cross section measurements or short baseline physics) since they provide a constraint on the neutrino flux that is independent of the neutrino-interaction cross sections. It also may be possible to measure the ratio of positive and negative muons at several depths or muon ranges. The goal is to constrain the ratio of neutrinos to antineutrinos at the 4-5% level.

3.2.2 Muon Measurements

The dominant, two-body decays of pions and kaons that produce neutrinos also result in the creation of a daughter muon. Monitoring the muons exiting the decay volume can provide information about the direction, size, shape and flux of the neutrino beam. The daughter muon and neutrino energies in those two-body decays are completely anti-correlated. For example, a $\pi^+ \rightarrow \mu^+ \bar{\nu}_\mu$ decay will result in a $\bar{\nu}_\mu$ with an energy, E_ν, between zero and $0.43E_\pi$ plus a μ^+ with an energy of $E_\mu = E_\pi - E_\nu$ between $0.57E_\pi$ and E_π. This has the effect that the muon takes 79% of the pion energy on average, leaving the neutrino with only 21%. Thus, on average, the muon energy is 3.75 times that of the neutrino.

Because muons and neutrinos come from the same parent pion and kaon decays, a measurement of the absolute muon flux in conjunction with the energy spectrum seen in the muon monitors can confirm the absolute neutrino flux. The goal for the LBNE muon monitors is to determine the absolute muon flux to an accuracy of 5% above a muon energy of 6 GeV (which corresponds to a neutrino energy of 1.6 GeV) in the central part of the absorber. Figure 3–1 shows the total simulated neutrino flux at the Far Detector overlaid with the flux from only neutrinos having pion or kaon parents that contribute to the signal seen in the muon monitor. The simulation shows that between 3 GeV and 10 GeV, more than 90% of the neutrinos in the Far Detector come from this subset.

It is essential to monitor the stability of the beam direction over time. Figure 3–2 shows the effect on the muon-neutrino flux in the Far Detectors when the beam is misaligned by 0.4 mrad. For example, above 6 GeV, the ratio of the Far Detector flux over the Near Detector

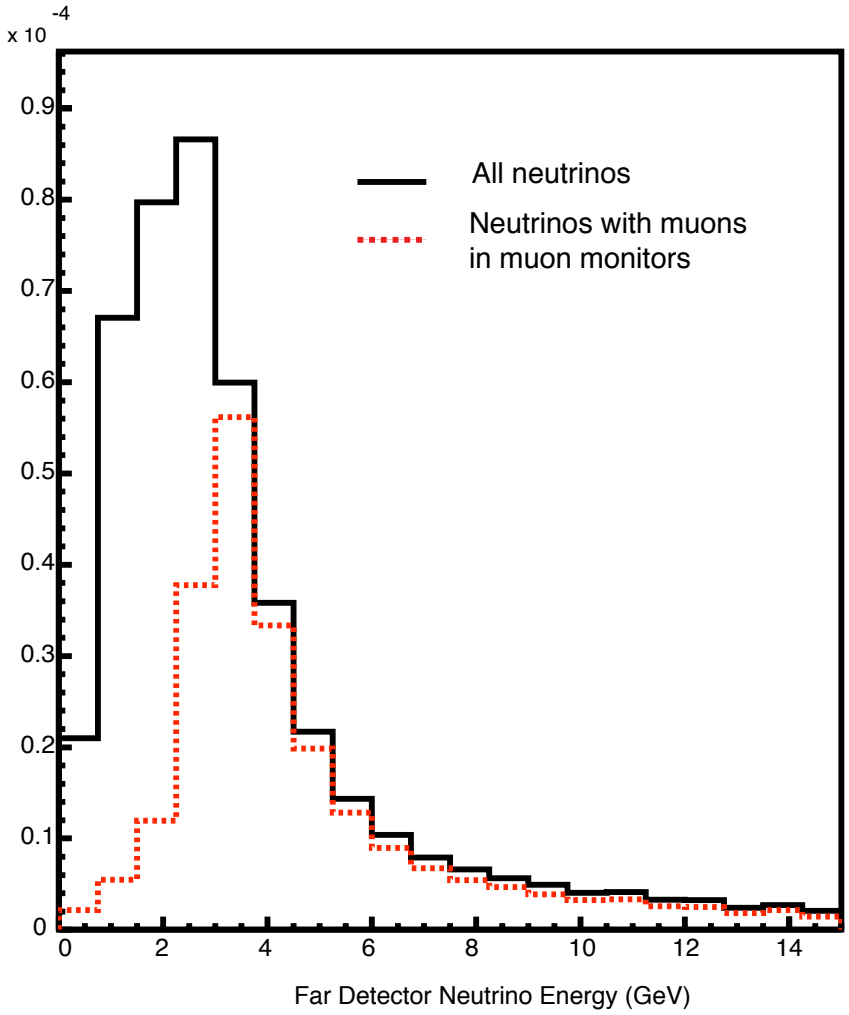

Figure 3–1: The total simulated neutrino flux at the Far Detector (black solid) overlaid with the neutrino flux, also at the Far Detector, coming from neutrinos with pion or kaon parents that contribute to the muon-monitor signal (red dashed).

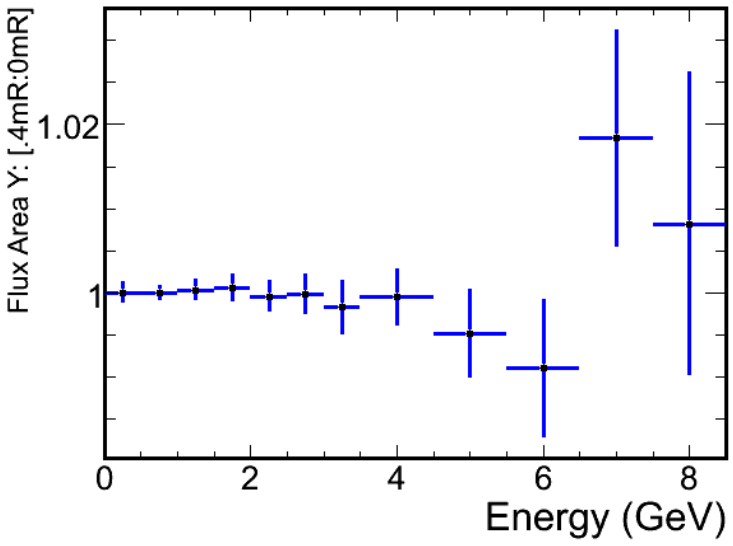

Figure 3–2: Ratio of the flux on-axis to the flux 0.4 mrad off-axis at the Far Detector position.

flux changes by 2%. To keep the change in the neutrino beam less than 1% in all energy bins, the beam direction must be known to a precision of approximately 0.2 mrad. Because the muon monitors will be located approximately 275 m from the beam target, this requires a measurement of the muons to an accuracy of approximately 5 cm.

The rate of muons crossing the monitors will be quite high, with preliminary LBNE beam simulations suggesting approximately 50 million muons per cm^2 for a pulse of 10^{14} protons-on-target. The muon monitors must also be capable of operating in a high-radiation environment. For example, the expected dose in the area downstream of the NuMI absorber is as high as 100 MRad per year [15].

3.2.3 Hadron Measurements

Hadron measurements, in particular, measurements of the kaons, pions and muons, could reveal the impact on LBNE sensitivities due to uncertainties in hadron-production in the beam. A complete knowledge of the momenta and decay points of these particles would be sufficient to completely predict the un-oscillated flux of neutrinos at the Near and Far Detector locations. This requires knowledge of:

- the phase-space distribution of the initial proton beam
- details of all materials present in the target, horn and decay pipe areas
- the electromagnetic focusing characteristics of the magnetic horn

- the detailed development of the hadron cascade, spawned by the the initial proton, that passes through the target/horn/decay tunnel
- the meson-to-neutrino decay rates

With careful engineering design and careful control of the materials in the target area, all of these items can be simulated accurately except the hadronic cascades in the target, horn and decay tunnel. The simulation of the hadronic cascade requires accurate knowledge of the hadron-production cross sections, for which there are no first-principle calculations. These cross sections must therefore rely on models, which in turn require hadron-production measurements that span particle type, particle energy and the various materials found in the target, horn and decay tunnel.

Uncertainties on hadron production translate into uncertainties in the neutrino fluxes in the LBNE detectors, since the hadrons decay into neutrinos in the decay tunnel. At the present time, a sufficient body of hadron-production measurements does not exist to achieve LBNE's desired accuracy of 3-4%, as determined by the irreducible error on the statistical uncertainty for the appearance-measurement background, although this is expected to improve over time. Certainly at the conclusion of LBNE operations, the experiment will have collected sufficient data to pin it down to that level.

In order to keep the uncertainty in the near/far event-rate ratio from being limited by systematic uncertainties in the flux, the LBNE flux simulation must be accurate at the 4-5% level. Efforts at this stage are intended to understand the effect of the uncertainties in hadron-production in the beamline on overall LBNE sensitivities, to determine what further measurements may be needed by LBNE and to estimate their potential cost to the Project.

3.3 Muon-Measurement Facilities

The muon measurements are carried out in the region immediately following the hadron absorber at the end of the decay tunnel, below the absorber service building (LBNE 30). A top view of the service building is shown in Figure 3–3. An elevation view of the absorber area and the muon alcove is shown in Figure 3–4. The axis of the decay pipe cuts across the muon alcove at an angle and the size of the alcove is largely determined by the requirement that it contain the shadow of the four-meter-diameter decay pipe, projected through the alcove, as shown by the blue lines in the elevation view of Figure 3–4.

Figure 1–2 in Chapter 1 shows the downstream side of the absorber and a conceptual layout of the muon systems described in various sections of this chapter. The absorber itself is encased in concrete. The first set of muon-measurement devices, from left to right, is the 5×5 ion-chamber array which is mounted directly to the rear wall of the absorber. Following

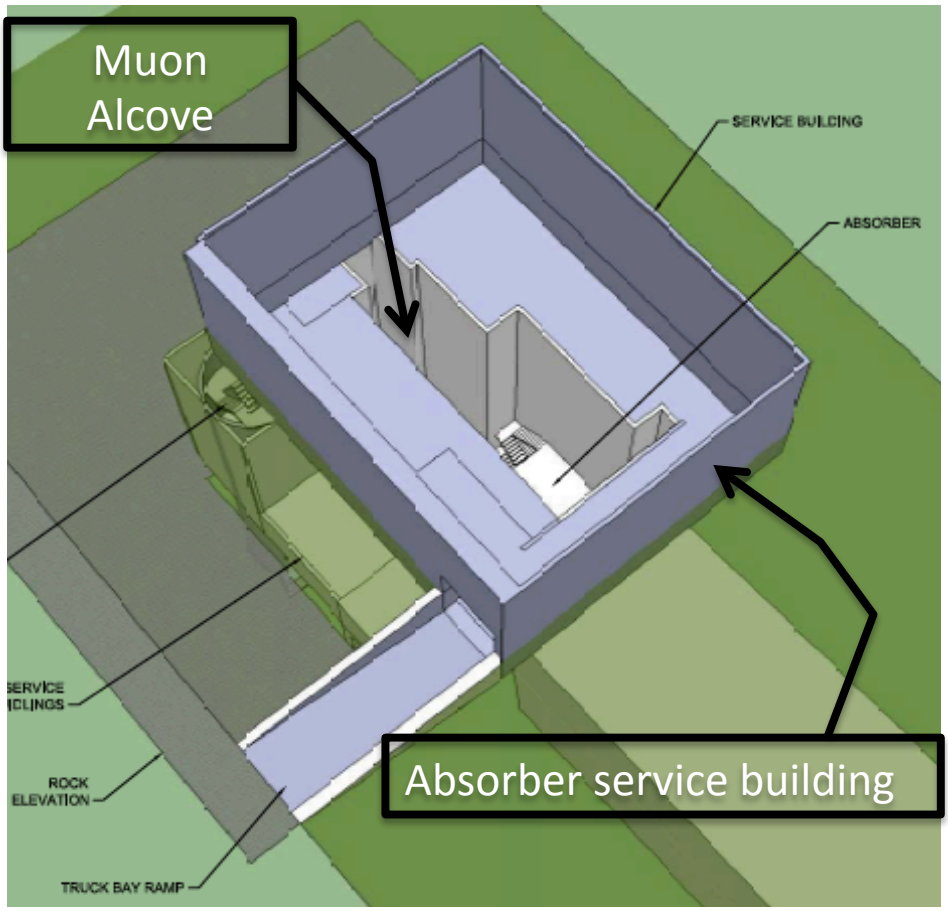

Figure 3–3: The absorber hall service building showing the location of the muon alcove and absorber.

that, a set of three variable-pressure gas Cherenkov counters, and finally a set of stopped-muon counters which are interspersed between walls of steel "blue blocks". The blue blocks are there to provide several depths at which to monitor the stopped muons as they range out in the material.

It is important to have precise knowledge of the amount of material muons pass through before they are registered in the muon systems. The absorber itself is a complex, heterogeneous assembly of various materials. Figures 3–5 and 3–6 show the absorber conceptual design (more detail is available in Volume 2 of this CDR). A hole in the front side of the absorber, at left, is both surrounded and followed by the aluminum core of the absorber. The core is then surrounded by steel and standard steel "blue blocks" which is in turn surrounded by concrete. This complex geometry must be carefully understood and simulated in order to make the muon measurements effective.

Figure 3–7 shows the energy lost by a horizontal muon as it traverses the absorber, as a

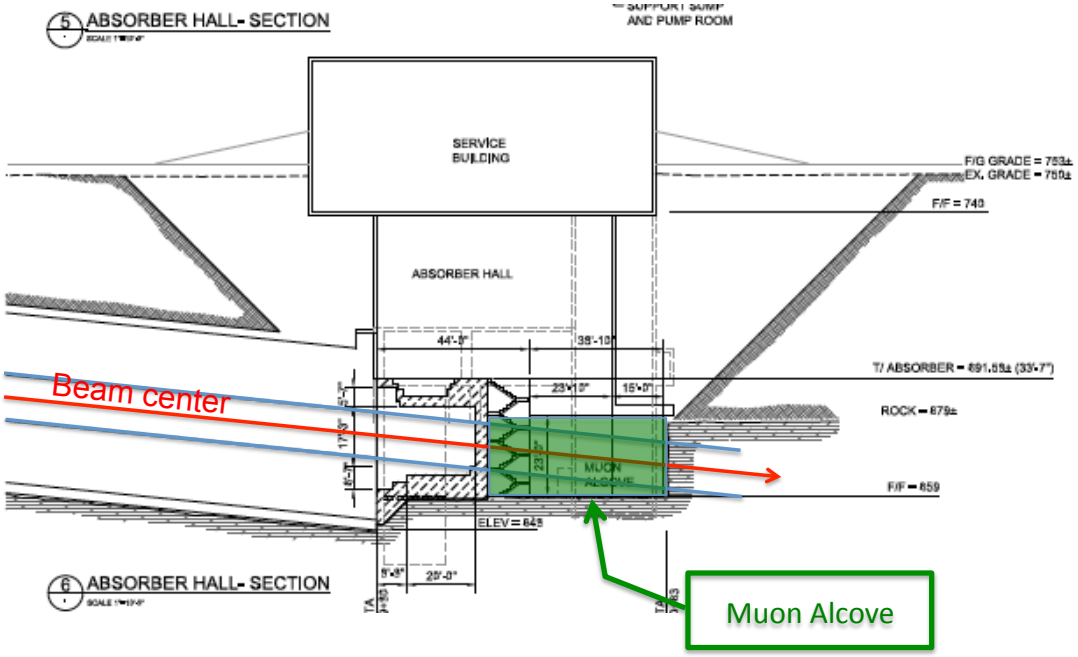

Figure 3–4: The absorber hall elevation view. The service building is on the surface and allows for crane access to the absorber hall. The muon alcove is directly behind the absorber.

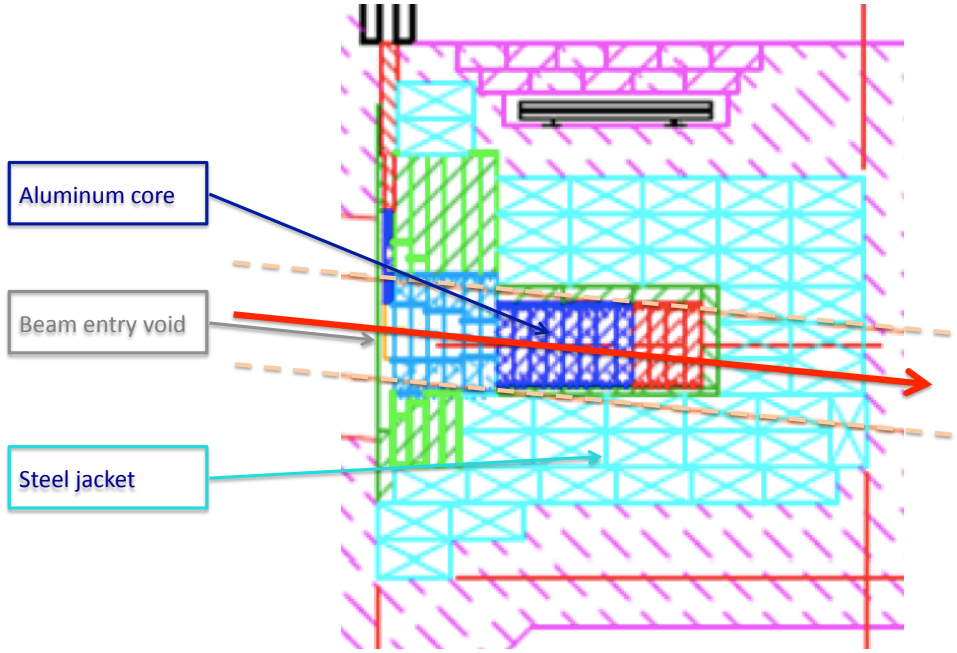

Figure 3–5: Absorber conceptual design. The figure shows the elevation view of the absorber at the end of the decay tunnel. The beam direction is shown by the red arrow. The absorber is constructed of several different materials as shown: aluminum (dark blue), concrete (magenta), and steel (other colors).

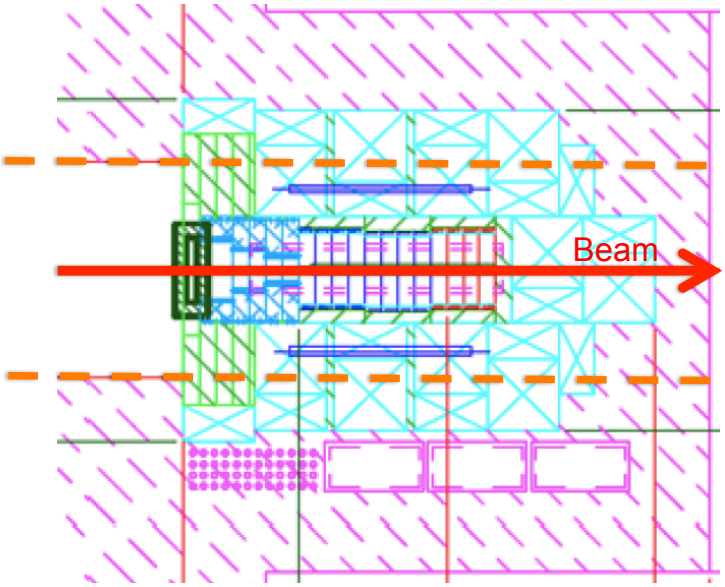

Figure 3–6: Absorber conceptual design, similar to Figure 3–5 but shows the plan view of the absorber.

function of the horizontal distance from the center. In the central region, out to a radius of roughly 50 cm, the muons lose roughly 5.6 GeV, so that the lowest-energy muons leaving the absorber at that point correspond to neutrino energies of $\sim$ 1.5 GeV. At a radius of roughly 70 cm, the full thickness of steel causes the muons to lose nearly 10 GeV, corresponding to neutrino energies of $\sim$ 2.6 GeV. From the perspective of the muon systems it would be desirable to lower these thresholds if possible. This might be accomplished by using more aluminum in the front part of the absorber. Of course the first concerns must be the containment of the radiation field induced by the proton beam, and the integrity of the absorber itself.

3.4 Muon-Ionization Measurements (WBS 130.03.03.03)

3.4.1 Introduction

Post-absorber muon measurements in most of the recent neutrino-beam experiments have typically employed a planar array of ionization counters to measure the muon profile and intensity. The NuMI beamline [15] and the K2K [16] [17] and T2K [18] [19] experiments have all utilized parallel-plate ionization chambers. These counters have been shown to work in the high-radiation environment.

K2K and T2K have also deployed solid-state silicon detectors [17] [20]. The advantage of

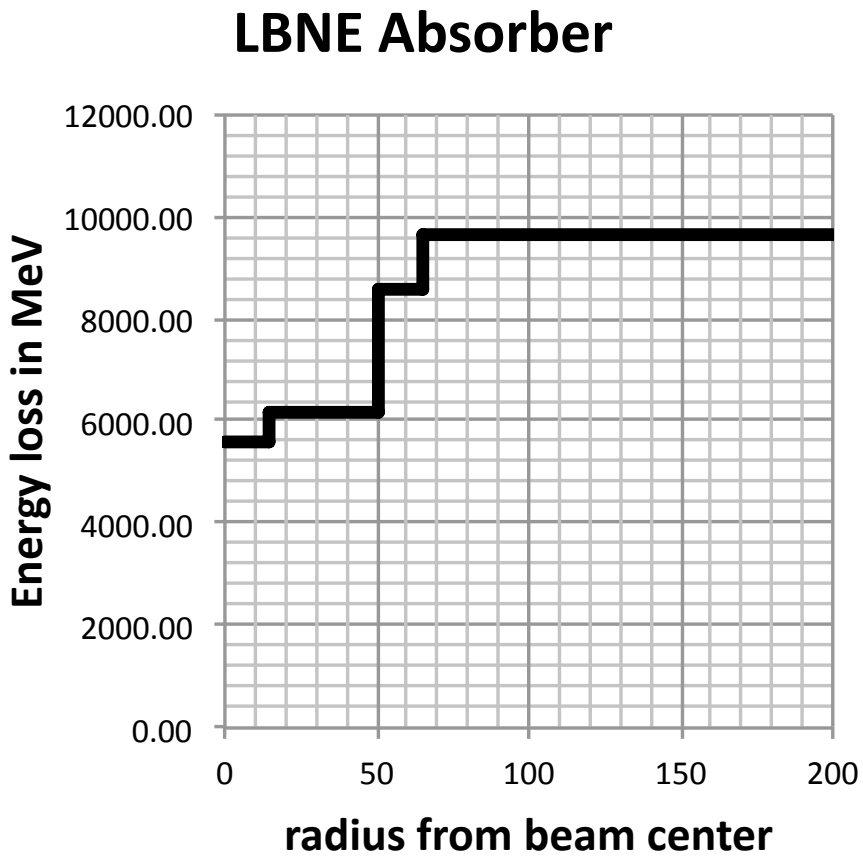

Figure 3–7: The absorber's approximate energy loss versus horizontal radius provides an indication of the variation in the depth of the absorber. Muons lose between 6 and 10 GeV depending upon where they cross the absorber.

silicon is that it is less sensitive to changes in the air temperature and pressure. However, these sensors are not as radiation-tolerant as the parallel-plate ionization chambers and will only be used in T2K for the initial beam operation.

One disadvantage to ionization counters is that they measure the total ionization deposited from all particle species (including the delta-ray electrons produced by the muons), making it challenging to convert the ionization signal into an absolute muon flux. The LBNE NDC plans to use the ionization counters to monitor the beam stability, direction and shape, but not to determine the absolute flux of muons or to determine the muon-energy spectrum. Instead, the stopped-muon counters (WBS 130.03.03.02) and gas Cherenkov detector (WBS 130.03.03.04) will be used, respectively, to determine the flux and energy spectrum of the muons.

3.4.2 Reference Design

The conceptual design for the LBNE muon-ionization chambers is similar to that used in NuMI, K2K and T2K. Due to their high radiation tolerance, sealed ionization counters are the default technology. For example, the CERN neutrino beam to Gran Sasso (CNGS) system uses an array of Large Hadron Collider (LHC) beam-loss monitors. For LBNE, it might be desirable to investigate solid-state devices besides silicon, such as diamond detectors (which are approximately an order of magnitude more radiation-tolerant than silicon counters [20][21]), to deploy as a cross-check of the gas ionization counters.

Figures 3–8 and 3–9 show the conceptual design for the ion-chamber array. Our conceptual design is based on commercial ion chambers by LND, Inc. model 50343. This chamber operates at 400 V and is designed to be sensitive to muons and insensitive to backgrounds such as neutrons. The chambers will be mounted in a 5×5 grid, four meters by four meters. Radiation-hardened cables will be used to carry the signal to waveform digitizers, providing a complete spill-by-spill record of the muon beam.

Unlike the NuMI muon monitors, the current design for LBNE only includes a single plane of ionization counters instead of multiple layers located at different depths within the rock. The array will be spread across a 2-m $\times$ 2-m area. LBNE wants to achieve a precision in the beam center of .2 milliradians (5 cm for a 250 m decay pipe). A quick study has determined the optimal arrangement of 25 ionization counters. For comparison, the NuMI monitor planes consist of a 9×9 array, and the T2K monitors use a 7×7 array of counters. The decision to use 25 counters for LBNE was motivated by a desire to see if a 7x7 array with some of the diagonal counters removed could achieve the desired sensitivity, thus reducing the total number of needed counters.

Several different designs for the counter arrangement were studied and the area covered by the detectors was varied. A toy Monte Carlo model was developed to estimate the precision

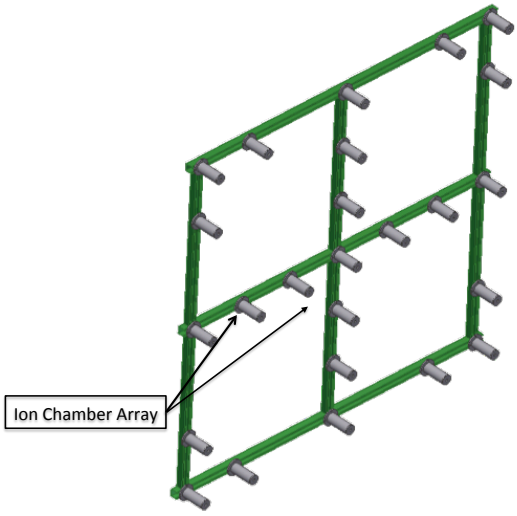

Figure 3–8: A model of the ion chamber layout on the back wall of the absorber showing the 5×5 grid configuration and supporting Unistrut rails.

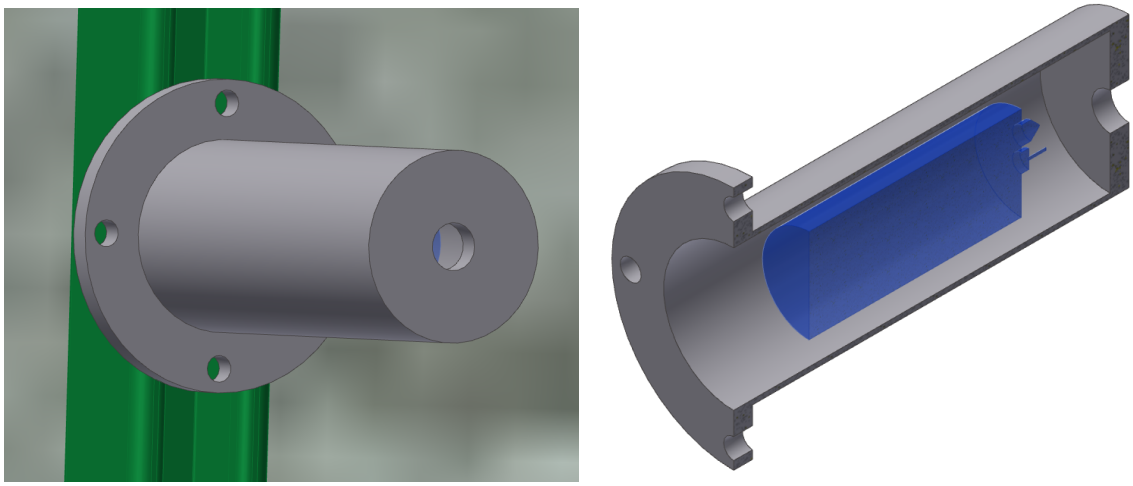

Figure 3–9: A model of the ion chamber housing and a section showing the commercial ion chamber inside the housing.

of each design. The muon profile was assumed to be a Gaussian with a spread of 130 cm in the x and y dimensions and a center at the origin. The standard deviation on the beam center was studied as a function of array coverage for several designs and for 2%, 5% and 10% random systematic error offsets. Figure 3–10 shows the precision of the detector array as a function of the width of the detector for a grid design and with 5% offsets. Figure 3–11 shows the same plot for a the "cross with corners" layout.

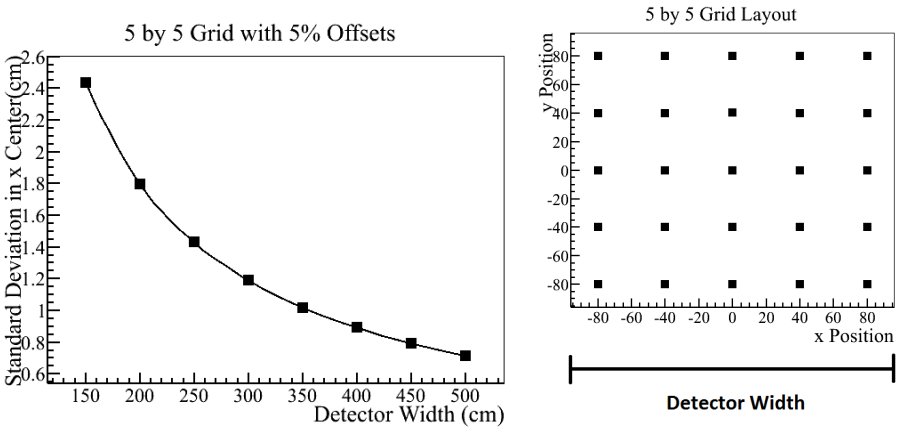

Figure 3–10: On the left: Precision as a function of detector width for a grid shaped detector with 5% random calibration offsets. On the right: The arrangement of ionization counters for the "5 by 5 grid" layout.

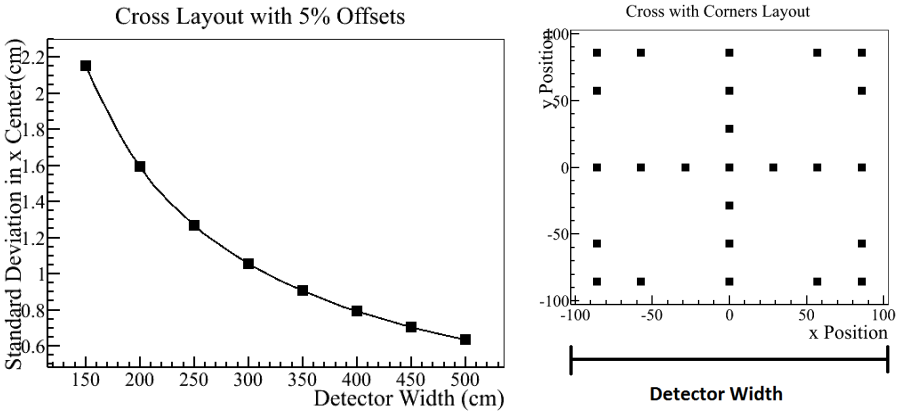

Figure 3–11: On the left: Precision as a function of detector width for a cross-shaped detector with 5% random calibration offsets. On the right: The arrangement of ionization counters for the "cross with corners" layout.

The results show that the width of the detector array affects the precision more than the layout of the detector. Increasing the array size improves the precision greatly. Concentrating the ionization counters to the outside of the layout gave the best precision for this simple model, but only by a small amount. Even for the layouts with 10% offsets and a width of 150 cm, the standard deviation on the beam center was less than our goal of 5 cm.

3.4.3 Prototype Design and Testing

For the gas ionization detectors, material irradiation tests may be done to determine how long the materials (such as the alumina ceramic in the counters) can survive in the intense radiation environment. Once suitable materials are identified, small prototype counters can be built and potentially operated in the existing NuMI alcoves to determine the optimal design and operating conditions for the LBNE monitors. This could be done prior to or following the long shutdown for the NOvA upgrade that will begin in June 2012, and extend through May 2013. That will provide a good field test in roughly the same environment as expected during LBNE operations. It can also be cross-checked against the existing NuMI muon-monitoring system.

3.4.4 Installation

The system installation will begin following completion of the Absorber Hall and the installation of the stopped-muon counter system (described in Section 3.5).

3.4.5 Operation

The muon-monitor-system data will be displayed in the control room on a spill-by-spill basis to monitor the beam stability. Because the system will be located in a radiation-controlled environment that will not be accessible during the beam operation, it is essential that the electronics be designed for remote operation.

3.5 Stopped-Muon Detector (WBS 130.03.03.02)

3.5.1 Introduction

An option being developed for measuring muons is stopped-muon counters, also called Michel-electron detectors. This method is still conceptual; however, in principle, it could measure the muon flux without suffering from some of the disadvantages intrinsic to systems that detect through-going muons. The strategy employed here is to stop muons in a material with significant carbon content and, via muon capture, to produce ^{12}B that will in turn undergo β decay. The high-carbon material, in this case graphite, surrounds a Cherenkov radiator material which is sensitive to electrons from muon decay or high-energy beta decays. Figure 3–12 shows a conceptualization of a single stopped-muon counter.

The detectors would only operate in the lower-rate environment that is present many mi-

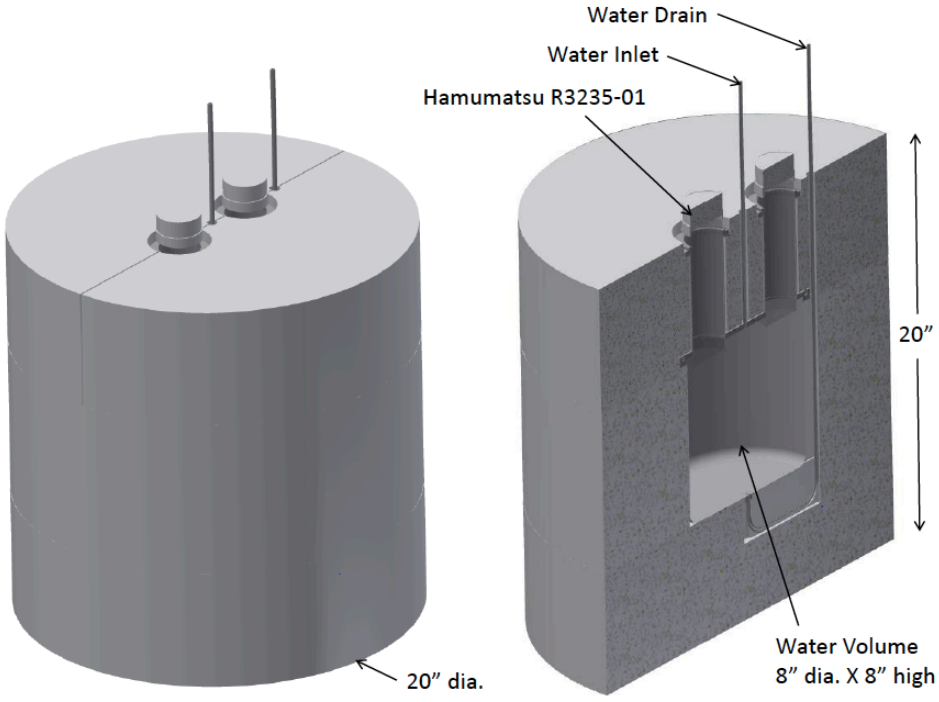

Figure 3–12: A conceptualization of a single Michel-electron detector (stopped-muon counter).

croseconds after the beam pulse is over. There are two possible modes for this type of system. The first is an integrating mode where the characteristic decay time of 2.2 μs for muon decay and corresponding beta-decay lifetimes is used to unfold the total number of decays. The other mode under investigation uses the ability to record individual decays rather than an analog current measurement. This mode may allow a more precise absolute normalization of the flux and fit the muon lifetime in the Michel-electron detector. This would provide a more robust cross-check on the muon signal than would ionization detectors, which are sensitive to delta rays, photon conversions and other charged particles.

Although this technique has never been tried on a large scale, a small demonstration project in K2K was able to see Michel decays with a 10^3 signal/background ratio and to measure the absolute rate with 30% precision[21].

3.5.2 Reference Design

If a stopped-muon detector system is included in the NDC subproject, it will be modular and based on a Cherenkov radiator of minimum size to contain a 53-MeV electron and distinguish it cleanly from lower-energy radioactivity. This conceptual design employs a liquid H_2O radiator, although mineral oil and aerogel are other possible radiator materials.

The radiator would be coupled to a photomultiplier tube (PMT) or other photon counter. Graphite has been chosen for the material surrounding the radiator as it provides the ^{12}C necessary for producing ^{12}B via muon capture. The entire module should be encased in a material that provides both a uniform-density stopping target for muons and some shielding from incoming neutrons. One or two signal channels will be associated with each module, and the full waveform from each channel over approximately 100 ms will be recorded on each beam pulse.

Approximately nine modules would be placed at multiple depths in the shielding or rock behind the absorber in order to sample the muon flux from different energies as shown in Figure 3–13. The shielding would simultaneously act to range out the muons and shield the detectors from neutrons. The Cherenkov light from Michel-decay electrons would exit the counter and be collected by either nearby PMTs or by a light guide which would guide the light to a remote optical sensor.

To probe the muon flux at lower energies, it may also be feasible and/or desirable to place some additional modules within the downstream part of the absorber or in the outermost radii of the decay-pipe shielding. The ability to do this may be limited, however, by the presence of muons from stopped, positively charged pion decays due to nearby hadron showers.

Besides the Michel decays of stopped muons, the system will independently measure both the μ^+ and μ^- stopped rates. While the 2.2 μs decay time of the μ^+ is a reliable signature, in graphite roughly 8.5% of the μ^- undergo capture on the ^{12}C nucleus, and 15% of those leave behind a ^{12}B ground state nucleus. That ^{12}B nucleus will undergo β decay with a half-life of 20.20 ms and an electron spectrum with an endpoint of 13 MeV. With a graphite layer around the detector, this signal may well be measurable and yield a reliable measurement of the spectrum of μ^- in the decay region.

3.5.3 Prototype Development and Testing

Prototype development activity for the Michel-electron detectors will be divided into studies of the rate and radiation environment where the detectors will be located and development of the counters themselves.

The radiation environment will be studied both with Monte Carlo and by measurements from initial prototype detectors in the NuMI muon alcoves [15]. Studies will be performed to determine if the photon sensors can survive the radiation environment at the location of the Michel detector. If the sensors can survive, they can be attached directly to the Cherenkov medium; if not, optical guides will have to bring the light to a lower-radiation area to the side of the beam. Potential radiation damage to the Cherenkov radiator itself will also be studied.

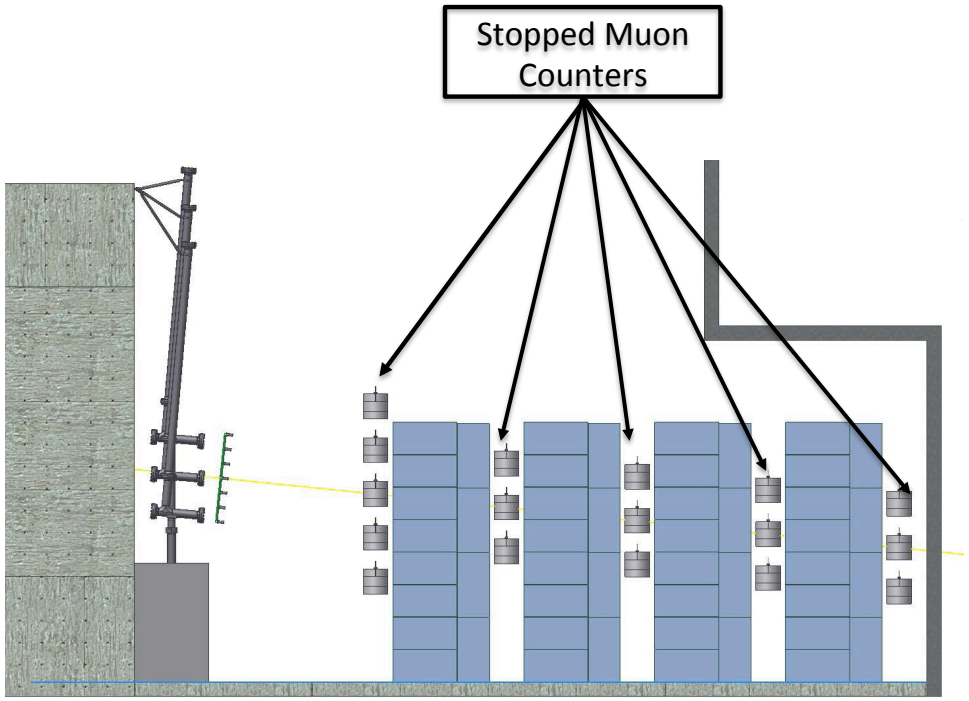

Figure 3–13: A possible arrangement of "blue blocks" and Michel-decay detectors. In this case there is roughly 2 GeV of energy loss per wall of blue blocks. The counters can be moved between layers and within a single layer.

The detector design will focus on selecting radiator and shielding material, photon-detection technology and control/readout hardware. Possible radiators include aerogel, which may be designed to be replaced periodically, and flowing liquids such as H_2O or mineral oil. Long-timescale saturation from the very high-rate environment of the beam spill could affect the photon-counting devices [22]. Thus, it will likely be necessary to design fast-switching, high-voltage circuits that turn on the photon counters in the first few microseconds after the spill is over. A similar system was developed in the 1990s for the Brookhaven Muon (g-2) Experiment [23] .

3.5.4 Installation

The stopped-muon counters will be installed after completion of the absorber area excavation and installation of the absorber. They will be lowered into the spaces between the blue-block walls on support frames. If needed, they could then be moved around to measure the stopped-muon rates across the muon beam.

3.5.5 Operation

The muon-monitor-system data will be displayed in the control room on a spill-by-spill basis to monitor the beam stability. Because the system will be located in a radiation-controlled environment that will not be accessible during the beam operation, it is essential that the electronics and gas-handling system be designed for remote operation.

3.6 Muon Cherenkov Detectors (WBS 130.03.03.04)

3.6.1 Introduction

As mentioned in Section 3.2.2, one disadvantage of an ionization system for the muon monitors is that it measures the ionization due to all particles, including delta-ray electrons and neutrons. This makes it difficult to determine the muon flux. Furthermore, the ionization system is unable to measure the momentum distribution of the muons. To resolve this problem, T2K is considering the idea of deploying a Cherenkov counter downstream of the absorber. If deployed by LBNE, a Cherenkov counter would not image individual Cherenkov rings, but rather would see the integrated signal from many muons due to the very large instantaneous flux. In addition, by varying the radiator gas pressure, and hence the Cherenkov threshold, the system's index of refraction would vary, allowing it to map out the muon momentum distribution.

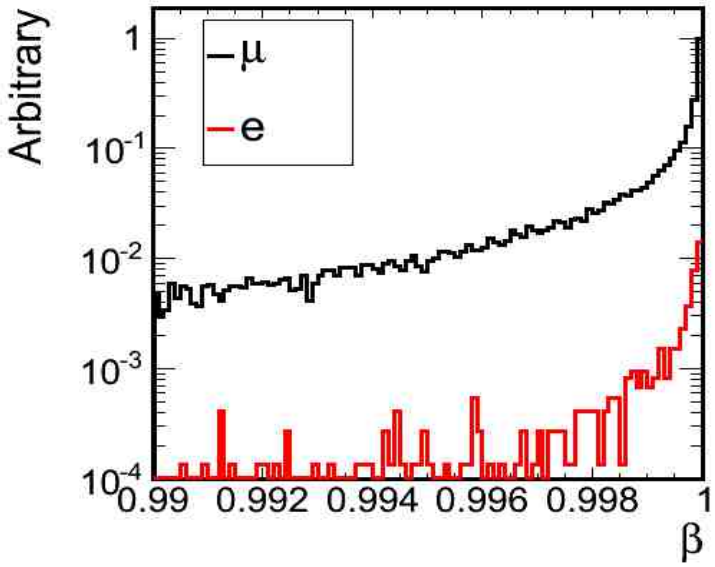

Figure 3–14: Simulated electron and muon velocities exiting the absorber. This plot is based on a simulation gnumi[24] of the LBNE beamline.

Figure 3–14 shows the expected distribution of velocities, β (v/c), for muons and electrons after exiting the absorber. Figure 3–15 shows the expected angle with respect to the beam for electrons and muons with similar velocities (implying that both are visible above the same Cherenkov threshold). Despite the similar velocities, the muons are much more likely than the electrons to be directed parallel to the beam. Therefore, a detector that takes advantage of the directional nature of Cherenkov light will have less background contributions from electrons and other isotropic background particles such as neutrons, than will an ionization system, for example.

3.6.2 Reference Design

There are a number of possible designs for Cherenkov counters. The conceptual design is based on a traditional beamline Cherenkov counter, where a gas radiator is contained in a pressurized tube. The Cherenkov light in a narrow cone is collected at the end of the tube by a mirror that reflects the light 90 degrees towards a photosensor located outside the high-radiation field of the alcove. The gas pressure, varied from vacuum to several atmospheres, would determine the index of refraction, and hence the muon-momentum threshold. Several such tubes could be constructed in an array transverse to the beam direction. The resulting pressure scan would give the momentum distribution of the muons at an array of points across the end of the absorber.

Figure 3–16 shows conceptually how the Cherenkov system might be constructed. Safety

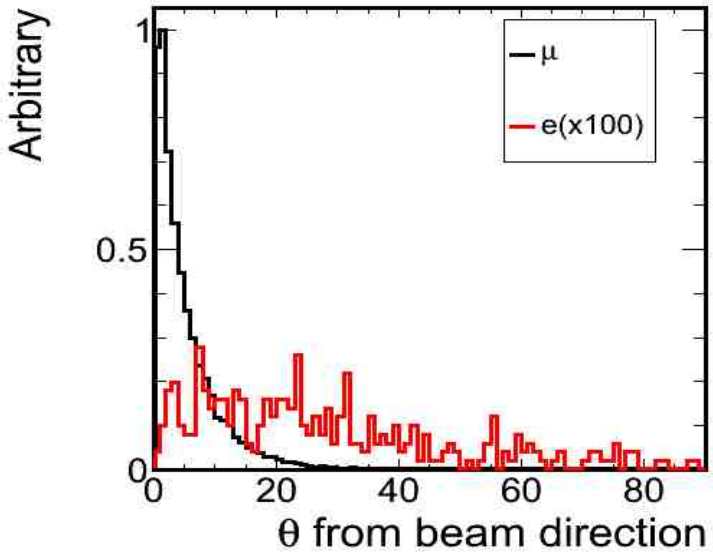

Figure 3–15: Simulated plot of angle with respect to the beam for electrons and muons exiting the absorber. This plot is based on a gnumi simulation of the LBNE beamline.

considerations suggest that the diameter of the radiator tube and light-guide tube be six inches or less. The use of a noble gas, e.g., argon, as the Cherenkov radiator would enhance the radiation hardness of the system. A photosensor, located outside the direct radiation field of the muons, would view the primary mirror through a telescopic optical system focused on the mirror.

The layout of the Cherenkov counter system is shown in Figure 3–17.

The preferred option is to use a gas Cherenkov system containing a noble gas with a high index of refraction, where the density of the gas can be varied to change the Cherenkov threshold. The noble gas will reduce potential degradation due to reactivity in the high radiation field of the post-absorber environment. Varying the pressure will provide more information about the momentum spectrum of the muons.

The combination of a flat mirror and a 90^0 mirror will reflect light out to a PMT. The UV-sensitive PMT will collect light from normal incidence on the primary mirror to $\sim$5 mrad. Figure 3–18 shows that, with a 5 mrad acceptance, the light yield per particle will be approximately one photon near threshold. That is more than ample light for the system where the particle flux is of order 10^8 per cm^2 on a PMT.

One possible background is transition radiation, which occurs when a charged particle moves between materials with different indices of refraction. This process can generate light in the visible region, and it can occur even when there is a vacuum inside the gas Cherenkov system. Figure 3–18 also shows that the transition radiation emitted from the mirror surfaces

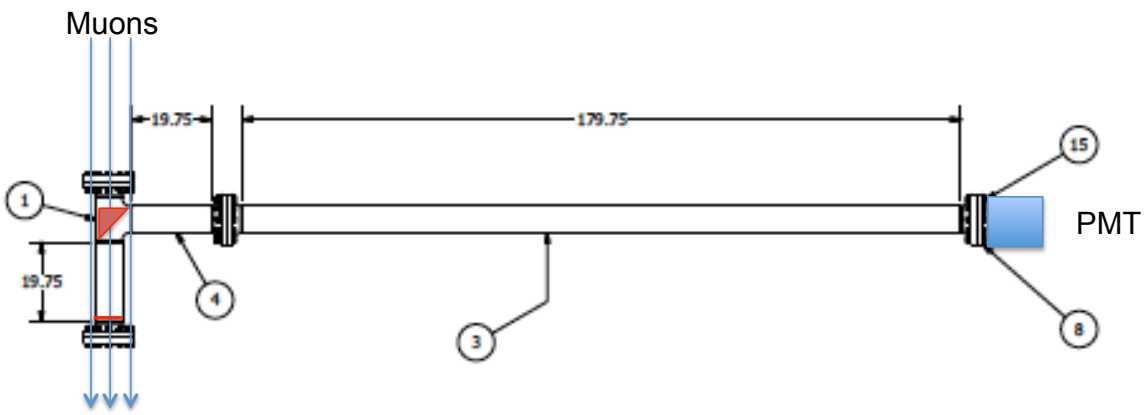

Figure 3–16: The Cherenkov counter conceptual design. Muons at threshold momentum emit forward Cherenkov light which is reflected via two flat mirrors to a PMT located outsie of the muon radiation field.

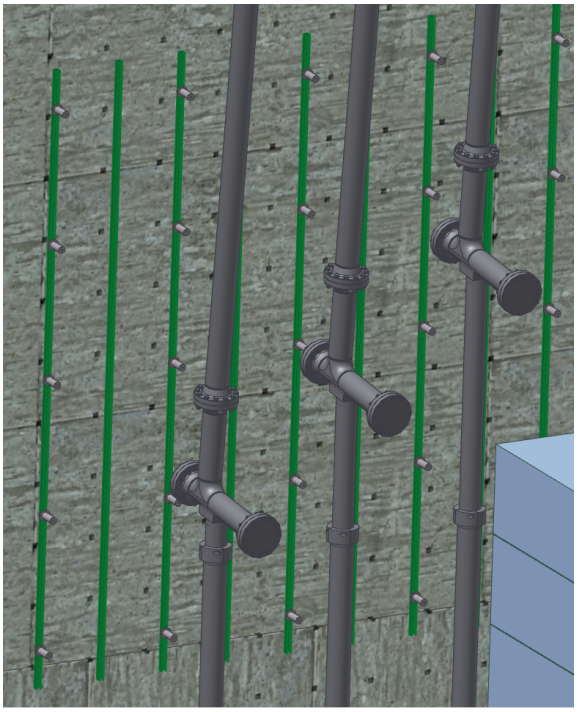

Figure 3–17: The layout of one of the muon Cherenkov counters behind the rear of the absorber.

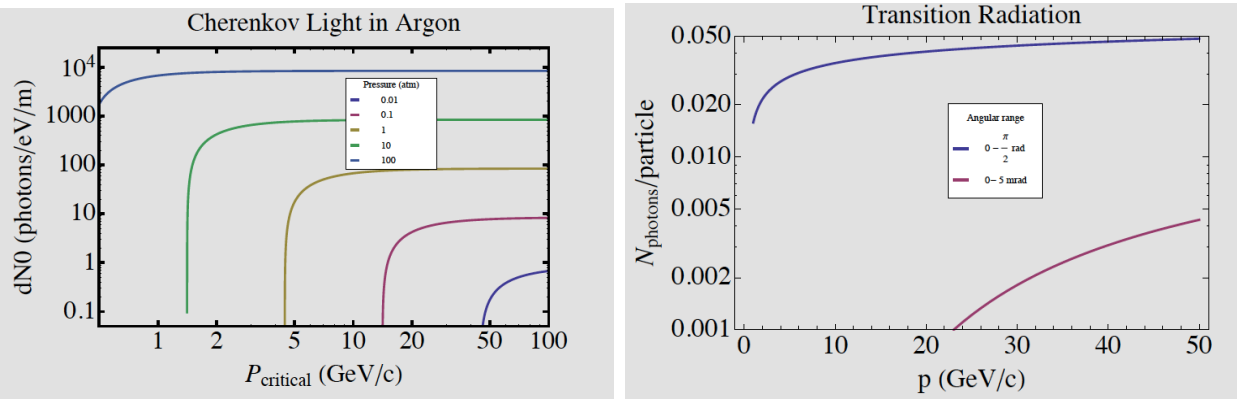

Figure 3–18: The calculated light yields for Cherenkov radiation (left) and transition radiation for muons in argon gas.

is at least two orders of magnitude lower than the Cherenkov light yield and thus does not introduce a significant background.

A standalone Geant4 [25] simulation for a proposed gas Cherenkov detector for the LBNE muon monitors was developed to investigate various mirror shapes. Based on this work, a conceptual design has been developed, shown in Figure 3–19. Here the muons enter on the right, Cherenkov photons are produced in a region of a dense gas*, and the light is bounced off of two mirrors towards a photosensor that sits in a lower-radiation environment. Based on fits to a Geant3 [26] simulation of the muons exiting the absorber, the following angular distribution was used to describe the probability of observing a muon with a given angle θ with respect to the beam axis

$$Prob(\theta) = A \times \theta e^{\frac{-\theta^2}{2\sigma(p)}} \tag{3.1}$$

where A is an arbitrary normalization and the width, a function of the momentum p, is given by

$$\sigma(p) = 5.903 p^{-0.681}. \tag{3.2}$$

Thus, as the momentum increases, $\sigma(p)$ decreases, and the muons become more forward-going.

Several different mirror shapes were examined, including spherical and conical. But flat mirrors, much simpler, were found to be adequate.

Figure 3–20 shows a simulation of the number of photons collected at the photosensor versus muon energy for a range of indices of refraction. Varying the gas density will allow sensitivity of the photon measurements to different parts of the muon-energy spectrum.

*Freon was used in the simulations, but this choice is not final.

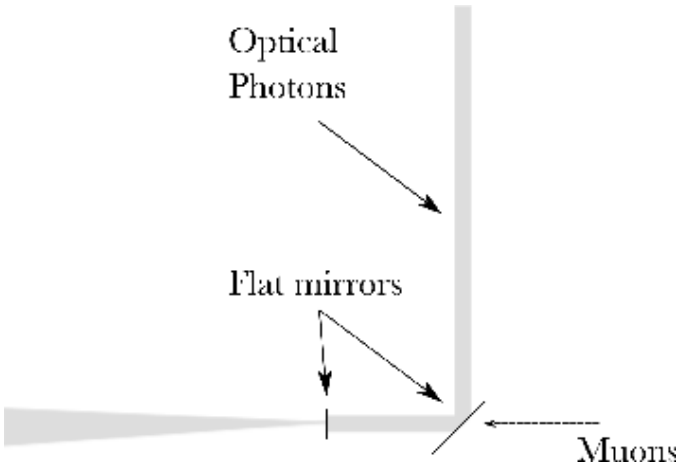

Figure 3–19: Conceptual design for the muon gas Cherenkov detector for LBNE. Muons will travel through an L-shaped pipe filled with a dense gas, and mirrors will direct the optical photons to a photodetector.

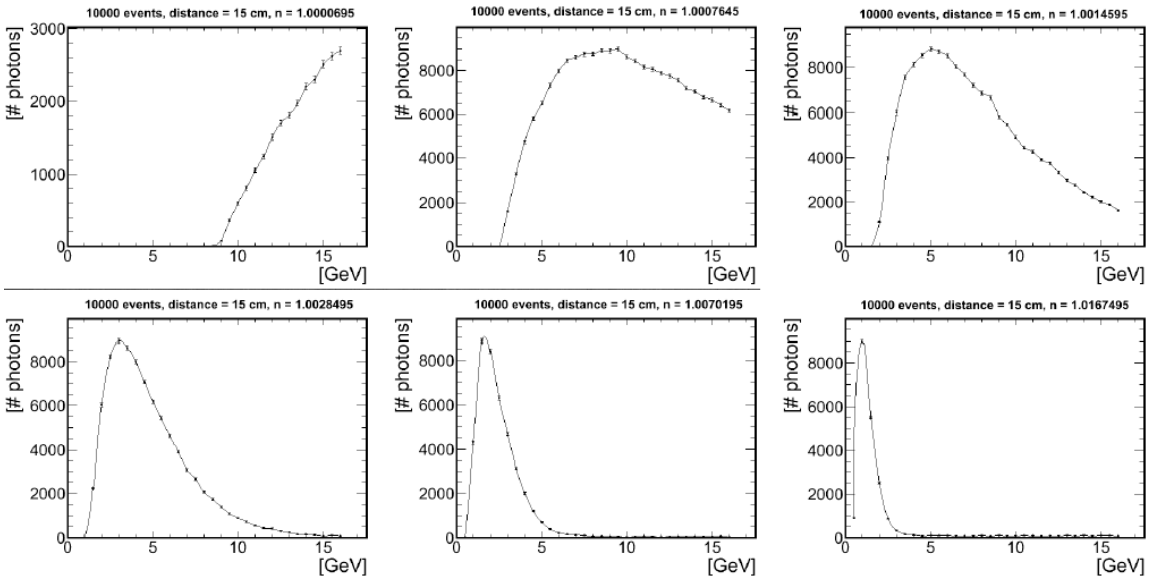

Figure 3–20: The number of photons detected in the photosensor vs. muon energy. Here 10,000 muons have been simulated at each energy. The gas density increases from 0.05 atm in the upper left to 12 atm in the lower left.

3.6.3 Prototype Development and Testing

Because this type of system has not previously been deployed for a muon monitor, significant design work and testing will be required. It will be important to understand the noise and background light from non-Cherenkov sources, such as fluorescence and scintillation in the gas and transition radiation. A small prototype system could be tested in the exiting NuMI beam alcoves, and a larger prototype could be tested following the NuMI year-long shutdown for the NOvA upgrade.

3.6.4 Installation

If this system is included in the LBNE near detector, installation would begin following the installation of the ionization and Michel systems. The system will need to be designed to fit inside the access shaft near the absorber.

3.6.5 Operation

Because the system will be located in a radiation-controlled environment that will not be accessible during beam operation, it is essential that the electronics and gas handling system be both robust and designed for remote operation.

3.7 External Hadron Measurements

3.7.1 Introduction

As discussed in Section 3.2.3, external hadron production measurements are expected to play a critical role once the Far Detectors have accumulated sufficient statistics toward the end of their running period to make systematic errors on the flux a dominant source of error in the oscillation measurement. The types of measurements foreseen begin with the primary hadron-production cross sections in the proton-target material, followed by similar studies in thick targets, and finally hadron yields after the complete target and focusing-horn system. In addition, hadron-interaction cross sections on materials in the decay tunnel and absorber can be important in flux calculations.

3.7.2 Motivation

Historically, a number of hadron-production experiments have contributed directly to the outcome of neutrino experiments by measuring meson production from the proton targets used by those experiments, and hence providing a constraint on their neutrino fluxes. For example, the HARP data[27] contributed directly to MiniBooNE and the SPY[28] experiment contributed directly to NOMAD. Since their contributions were crucial to those neutrino experiments, it is also expected that LBNE will require some dedicated hadron-production measurements. In the future, the MIPP experiment at Fermilab is planning to contribute its measurements to the NOvA experiment, and the NA61 experiment[14] is contributing to the T2K experiment.

3.7.3 Candidate Experimental Apparatus

The most suitable apparatus for LBNE's hadron-production measurements is the collection of equipment and detectors used by the MIPP experiment at Fermilab [13]. Again, once the MIPP collaboration has published its results, LBNE can decide whether to move in this direction. A full suite of LBNE-related hadron-production measurements would require the installation of the LBNE horn-focusing elements and associated power supplies in front of a future incarnation of MIPP in the meson area at Fermilab. This kind of effort could be within the scope of the LBNE Project and could be postponed until after LBNE construction or even after LBNE operations have stopped.

A proposal for using the NA61 experiment is also being developed since it is currently operating in the H2 beamline at CERN. NA61 does not have the complete suite of particle identification that MIPP does, but it could provide very useful hadron-production data for predicting neutrino fluxes at LBNE.

4 Neutrino Detectors (WBS 130.03.04)

4.1 Introduction

This chapter discusses the conceptual design for the Near Detector neutrino-measurement system. The reference design is a liquid argon TPC Tracker (LArTPCT). An alternative design, a straw-tube Fine-Grained Tracker (FGT) is also being considered because it offers some capabilities that are superior to those of the reference design. A final decision on the design for the Near Detector neutrino-measurement system will be made prior to CD-2. In both configurations, detector systems are located inside a large 0.4 T dipole magnet. The magnet is instrumented with scintillator planes for measuring outgoing muons.

4.1.1 Motivation

In order for LBNE to achieve the desired neutrino-oscillation sensitivity, the signal and background events in the LBNE far detector (LAr-FD) must be precisely predicted as a function of the parameters and variables that affect oscillations. These include energy, leading lepton (which tags the neutrino flavor) and the momentum and identification of particles generated by neutrino interactions. It is, therefore, crucial to measure the un-oscillated neutrino fluxes and their interactions at the near site. At the LAr-FD, the first and the second oscillation maxima signals occur at about 2.4 GeV and 0.8 GeV, respectively – an energy regime where neutrino cross sections and fluxes have large uncertainties.

In addition to the oscillation signal, it is critical to identify and measure processes that can mimic oscillation signals at the LAr-FD. Thus, the principal focus of the neutrino detector will be on the neutrino-oscillation energy range of $E_\nu < 5$ GeV, as well as higher neutrino energies that produce background to the oscillation signal. Clearly, the measurements must be comparable to those made in the LAr-FD, whose target material is liquid argon (LAr).

Finally, the neutrino detector must measure nuclear effects, including short-range correlations, pion-exchange currents, pion absorption, initial-state interactions, and final-state interactions. These nuclear effects have an impact on neutrino cross sections and energy de-

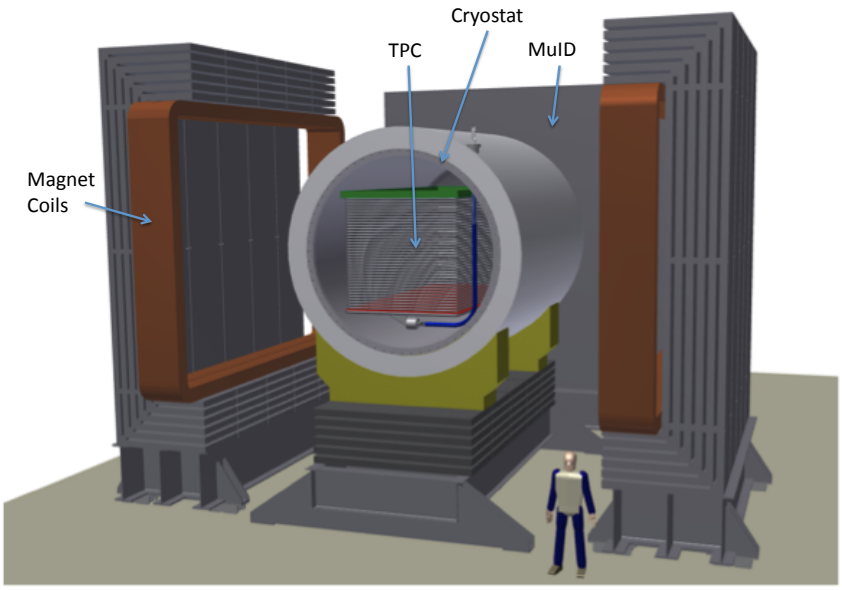

Figure 4–1: A schematic drawing of the LArTPCT reference design.

terminations, and differences between neutrinos and antineutrinos must be fully understood when searching for CP violation.

The proposed detector will constrain the systematic uncertainties in the LBNE oscillation measurements. Regardless of the process under study, the systematic error should be less than the corresponding statistical error.

4.1.2 Overview of Reference and Alternative Designs

A schematic of the reference-design LArTPCT is shown in Figure 4–1 (also in Chapter 1) and for comparison, the alternative-design fine-grained tracker (FGT) in Figure 4–2. In both configurations the detector system is located inside a large 0.4 T dipole magnet. The magnet is instrumented with scintillator planes for measuring outgoing muons. Table 4–1 provides a comparison of the performance for the two reference configurations. With a 120-GeV proton beam, the neutrino event rates in both detectors will be $\sim 0.35 \times 10^{-14}$ events/ton/proton on target [29]. Assuming 0.5×10^{14} protons per beam spill, this corresponds to 3 events per spill in the 18 ton active volume of the LAr TPC reference design. Overlaps between interactions are expected to be manageable.

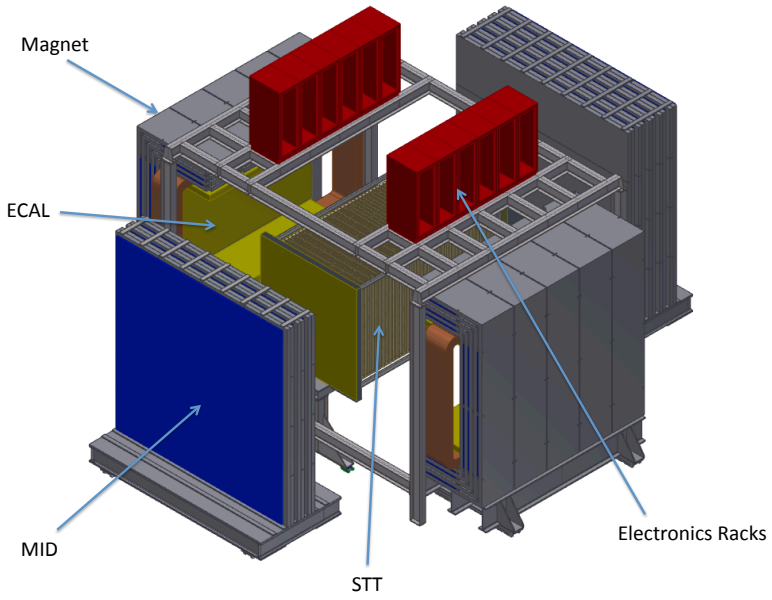

Figure 4–2: A schematic drawing of the fine-grained tracker (FGT) alternative design.

Table 4–1: A comparison of the performance for the reference configuration (LArTPCT) and the alternate configuration (FGT).

Performance Metric	TPCT	FGT
Tracking Detector Volume	1.8m x 1.8m x 4m	2.5m x 2.5m x 4m
Tracking Detector Mass	18 tons	2.5 tons
Vertex Resolution	1 mm	0.1 mm
Angular Resolution	10 mrad	2 mrad
E_e Resolution	10%	5%
E_μ Resolution	xi105%	5%
$\nu_\mu/\bar{\nu}_\mu$ ID	Yes	Yes
$\nu_e/\bar{\nu}_e$ ID	Yes ($E < 1.5$ GeV)	Yes
NCπ^0/CCe Rejection	1%	0.1%
NCγ/CCe Rejection	1%	0.2%
CCμ/CCe Rejection	0.1%	0.01%

The sides and ends of the dipole magnet, for either configuration, will be instrumented with a muon-identifier detector (MuID), discussed in Section 4.3.8. The MuID is only meant to provide the identification of the muon; the muon momentum will be measured by the TPC inside the magnetic field. The dipole magnet and MuID will have different dimensions for the two configurations, but will be basically the same.

4.2 Reference Design: Liquid Argon TPC Tracker (WBS 130.03.04.02)

4.2.1 Introduction

The LArTPCT is designed to measure the neutrino event rates and cross sections on argon for ν_e, $\bar{\nu}_e$, ν_μ and $\bar{\nu}_\mu$ CC and NC scattering events. The LArTPCT will make use of the expertise gained from the MicroBooNE experiment [30] by building a 1.8-m × 1.8-m × 4-m TPC and a 2.7-m-diameter × 5-m-long LAr cryostat inside of a large dipole magnet. An LArTPC with a magnetic field has the advantage of allowing measurement of the momentum of both particles that are contained in the tracker and those that exit. In addition, magnetization allows for measurement of the sign of charged particles that travel at least 50 cm in the tracker, which will be used in distinguishing muon-neutrino interactions from muon-antineutrino interactions. Automated event reconstruction for LArTPCs is still under development. Generally speaking, particle identification would be done by the density of tracks, and the total energy estimate would rely on total charge for fully contained tracks or the transverse and longitudinal deposition profile for partially contained tracks [31].

The LArTPCT, as shown in Figure 4–1, will consist of the following components:

- a cryostat to contain the cryogenic liquid-argon volume
- a time projection chamber (TPC) immersed in the LAr volume
- read-out electronics and data acquisition, also immersed, for the TPC with hermetic feed-throughs
- a 0.4-T dipole magnet surrounding the cryostat to enable measurements of particle momentum and charge
- a muon-identifier detector (MuID) on the sides and ends of the magnet

These will be described in the following sections.

4.2.2 Design Considerations

The LArTPCT must measure the neutrino fluxes and the individual backgrounds at the Near Site so that these fluxes and event rates can be extrapolated to the Far Detector location. The backgrounds must be measured individually because different backgrounds have different extrapolations. Specific design considerations for the LArTPCT include the following. First, a LAr TPC is chosen as the central tracker so that the neutrino cross sections and event rates are measured on argon and that the vertex resolution is sufficiently good (< 1 cm) to determine whether a track comes from the vertex (in the case of an electron) or is displaced from the vertex (in the case of a gamma). The LAr TPC also allows the reconstruction of the incident neutrino energy for CCQE events with good resolution in order to measure the neutrino fluxes as a function of energy and the reconstruction of neutral and charged pions produced in NC and CC scattering events. This is important because π^0 events constitute the largest background to ν_e and $\bar{\nu}_e$ appearance and π^+ and π^- events constitute the largest background to ν_μ and $\bar{\nu}_\mu$ disappearance. The muon identifier detector (MuID) is required in order to fully identify muons and separate them from pions. Finally, a magnetic field is needed for the separation of neutrino and antineutrino events. Such a magnetic field also improves the identification of gammas through pair conversion, $\gamma \rightarrow e^+e^-$.

4.2.3 Cryostat (WBS 130.03.04.03.01.02)

The cryostat, as illustrated in Figure 4–3, is a scaled-down version of the MicroBooNE design [30]. It will have an inner diameter of 110 in (2.794 m) and an inner length of 201 in (5.106 m), corresponding to a total LAr mass of 56 tons. The cryostat will be made of stainless steel with a wall thickness of 0.5 in. As with the MicroBooNE design, no internal or external supporting ribs will be allowed, which simplifies the modeling and analysis of particles exiting the cryostat. The cryostat will be insulated with a 16-in layer of insulating foam. The outer diameter and length will be 143 in (3.63 m) and 234 in (5.93 m), respectively.

The cryostat will be supported by hard polyurethane-foam saddles, again inspired by MicroBooNE.

An insulated catch basin surrounds the cryostat to contain any LAr that might be spilled in an accident. Pipes drain the catch basin into an insulated trough in the floor, keeping the cryogenic liquid away from any uninsulated material. The volume of the trough is sufficient to contain the entire contents of the cryostat in a worst-case accident scenario. The trough is insulated with the same foam used for the cryostat in order to prevent rapid boiling of any spilled cryogen.

An LAr purity monitor is part of the cryogenics system. The principle is to measure the electron-drift time in a tiny one-channel TPC. The design will be based on monitors used for ICARUS, ArgoNeut, and the LAPD [32]. The purity could also be monitored using the

drift times of long tracks in the detector itself, but the cryogenics system monitors are the primary method for real-time monitoring. At present, the purity goals are the same as for MicroBooNE ($<$ 100 ppt for O2 and $<$ 1 ppm for N2) and are such that variation at levels below those goals should not pose a big problem. Furthermore, any variation of charge-per-MeV with purity will be taken out by calibration using the charge-per-MeV observed for long, minimum-ionizing tracks.

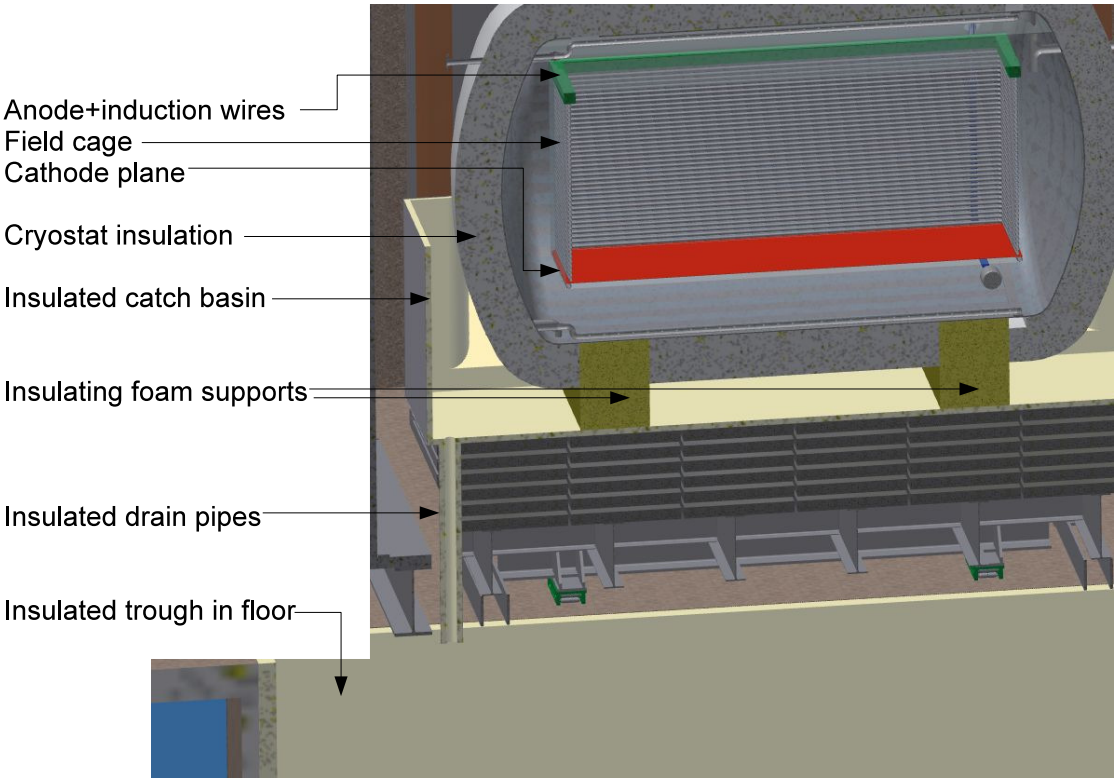

Figure 4–3: Cutaway drawing of the LArTPCT, showing field cage, cryostat, and supports and spill-containment system

The layout of the LAr cryogenics in the near detector hall is shown in Figure 4–4. The layout is based on the MicroBooNE design and includes a Filter Skid, a Pump Skid, a Heat Exchanger, a Molecular Sieve, and a Compressor.

4.2.4 Time Projection Chamber

The Time Projection Chamber (TPC) will have an active volume of 1.8 m $\times$ 1.8 m $\times$ 4 m. A schematic drawing of the TPC inside the cryostat and magnet is shown in Figure 4–5. The total mass of LAr in the TPC will be 23 tons. The argon impurity is required to be $<$ 30 ppb in order to ensure that electrons can travel the maximum drift length, cathode to anode, of 1.8 m. Purity-monitoring systems will operate continually.

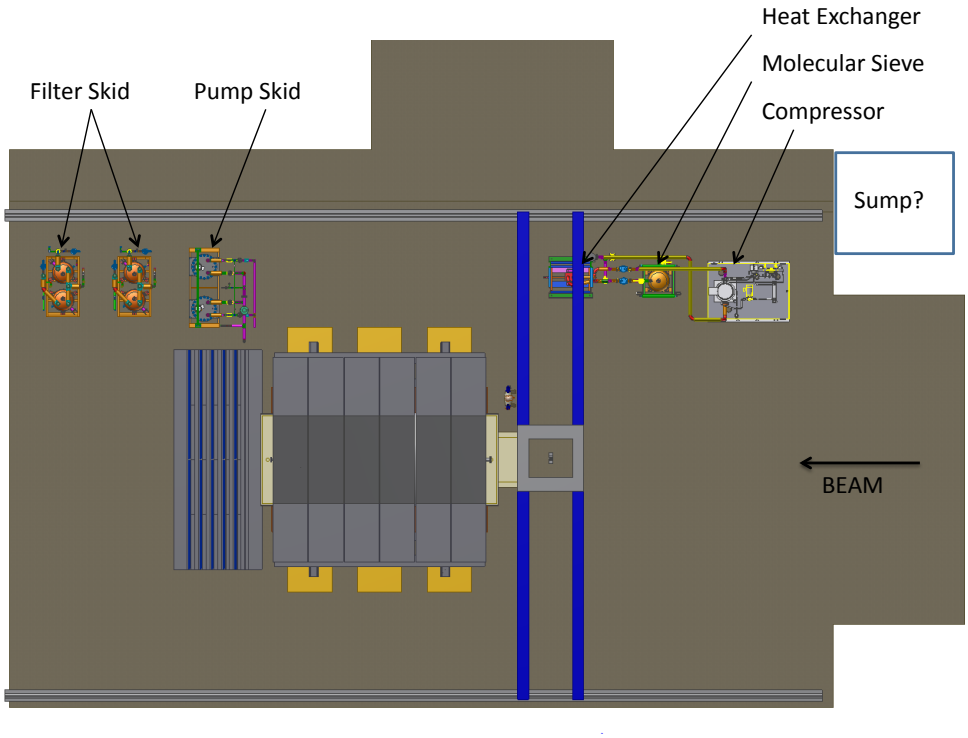

Figure 4–4: The layout of the LAr cryogenics in the near detector hall.

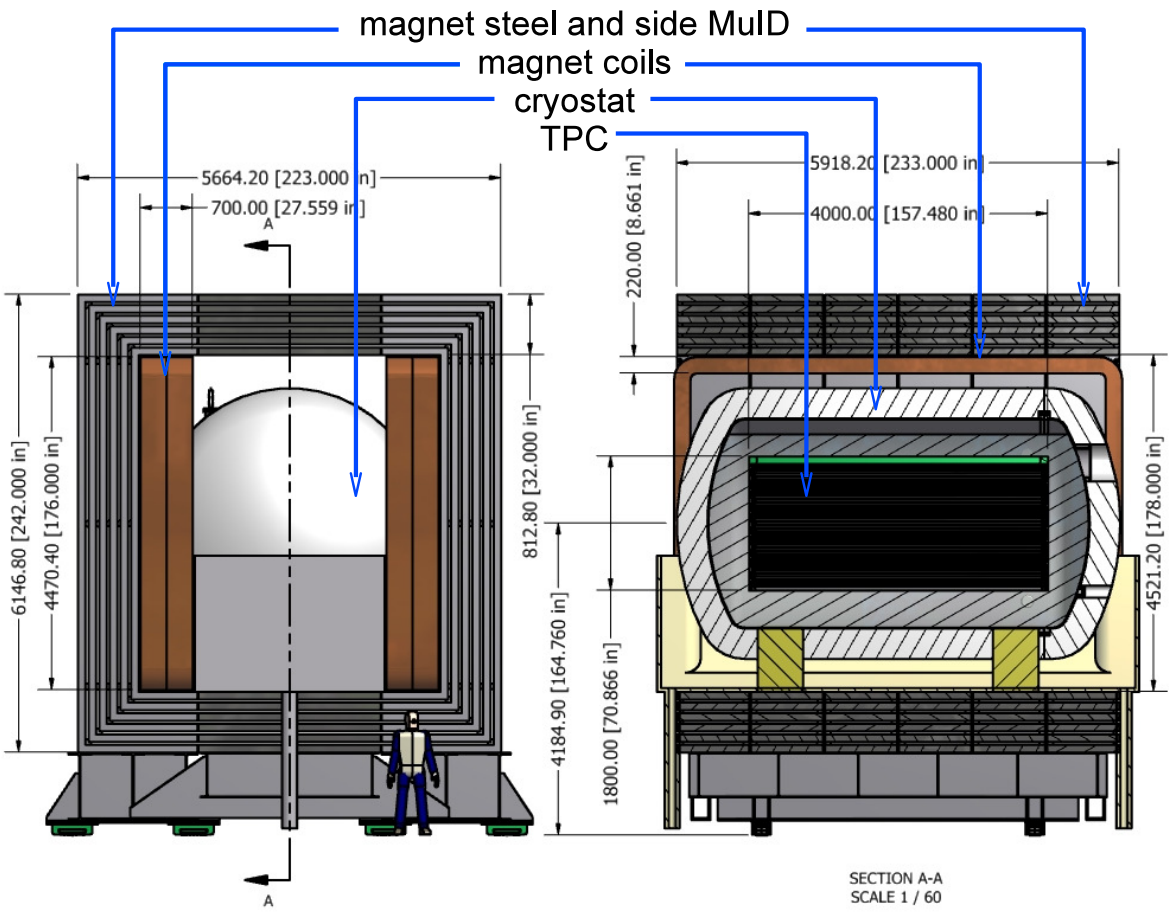

Figure 4–5: Schematic drawing of the LArTPCT inside the cryostat and magnet

A uniform field of 500 V/cm is produced by a field cage consisting of a cathode plane at −90 kV with respect to ground, an anode plane consisting of three readout wire planes spaced by 3 mm, near ground potential, and an array of stainless-steel tubes serving as field-shaping electrodes. (See Figure 4–3.) The ion drift velocity is 1.6 mm/μs. The wire planes consist of two induction planes (U, V) with wires running at 30 deg and 150 deg with respect to the beam direction (z-axis) as shown in Figure 4–6 and one collecting plane (Y) at 90 deg. The wire spacing is 3 mm. There are 1,333 Y wires of length 1.8 m, and 1,184 U and and 1,184 V wires with a maximum length of 3.6 m, resulting in a total of 3,701 TPC channels.

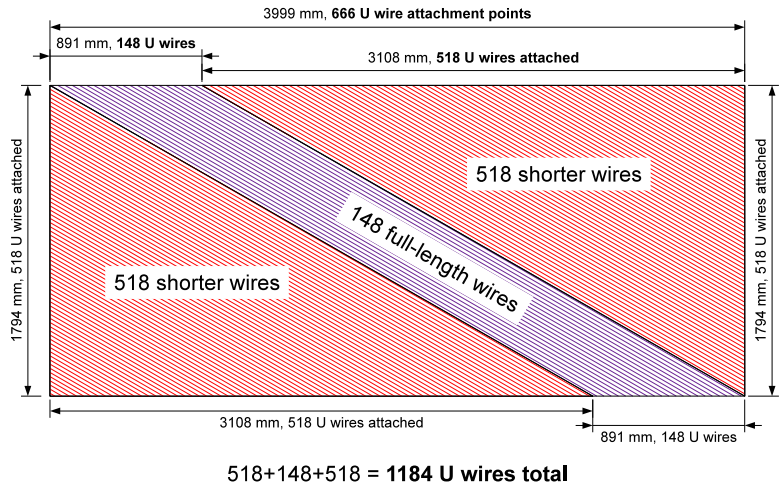

Figure 4–6: The arrangement of U wires in the LArTPCT. The arrangement of V wires is similar.

4.2.5 Cold Electronics and Hermetic Feed-Throughs (WBS 130.03.04.03.01.04)

The TPC digitizing electronics will be the same as that designed for use in the LAr1 prototype [33,34] and LAr-FD reference design, which is discussed in more detail in Chapter 3 of Volume 4 of this CDR. The entire electronic signal-processing chain is located at the wire plane in the LAr. This "cold electronics" system comprises all the detector electronics inside the cryostat, including the front-end preamplifier, shaper, ADC, digital multiplexers, and optical driver. A block diagram of the cold electronics can be seen in Figure 4–7. The output of two 20:1 multiplexers can carry the digitized data for all 3,701 wires in the TPC through a single cryostat feedthrough.

Hermetic feed-throughs are necessary for transporting the signals, calibration lines, preamplifiers, power, high voltage and monitoring lines from inside the cryostat to outside of it. These feed-throughs will be located at the top of the cryostat.

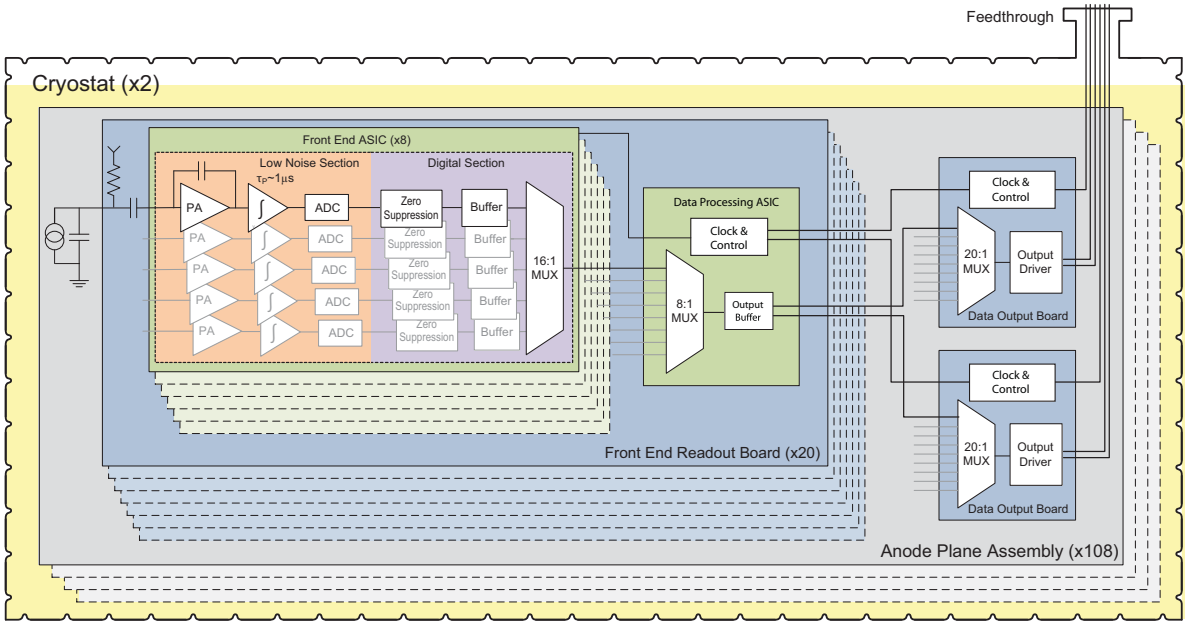

Figure 4–7: Block diagram of TPC cold electronics.

4.2.6 Dipole Magnet for the LArTPCT (WBS 130.03.05)

The LArTPCT will reside inside a 0.4-T dipole magnet with inner dimensions (inside the coils) of 4-m wide, 4-m high and 6.0-m long. The magnet, schematically illustrated back in Figure 4–19, is modeled after the CERN UA1 magnet with vertically stacked Al coils producing a horizontal magnetic field. The thickness of the magnet steel will be 60 cm, consisting of 6 × 10-cm thick plates. The magnet-power requirement with Al coils is ∼ 2.4 MW, corresponding to 6 A at 400 V. The water flow required for cooling is 20 l/s.

The momentum resolution is dominated by multiple scattering in the liquid argon, and is given by $\delta p/p = 0.053/\sqrt{(LX_0)B}$. For B = 0.4 T, L = 3 m, and $X_0 = 0.14$ m, the expected momentum resolution is ∼ 20%. This resolution is sufficient to distinguish μ^+ events from μ^- events, as required. Tests of a magnetized LArTPCT have been presented elsewhere. [31]

The magnet is discussed in more detail in Chapter 5.

4.2.7 Muon-Identifier Detector (MuID) (WBS 130.03.04.03.02.01)

The sides and ends of the dipole magnet will be instrumented with a muon identifier detector (MuID). The side MuID will consist of inexpensive scintillator planes interspersed

between 2 × 10-cm-thick steel plates of the dipole magnet, and the end MuID modules will be interspersed between 20-cm-thick steel plates at the upstream and downstream ends of the magnet. The MuID is only meant to provide the identification of the muon; the muon momentum will be measured by the TPC inside the magnetic field. A schematic drawing of the MuID is shown in Figure 4–20.

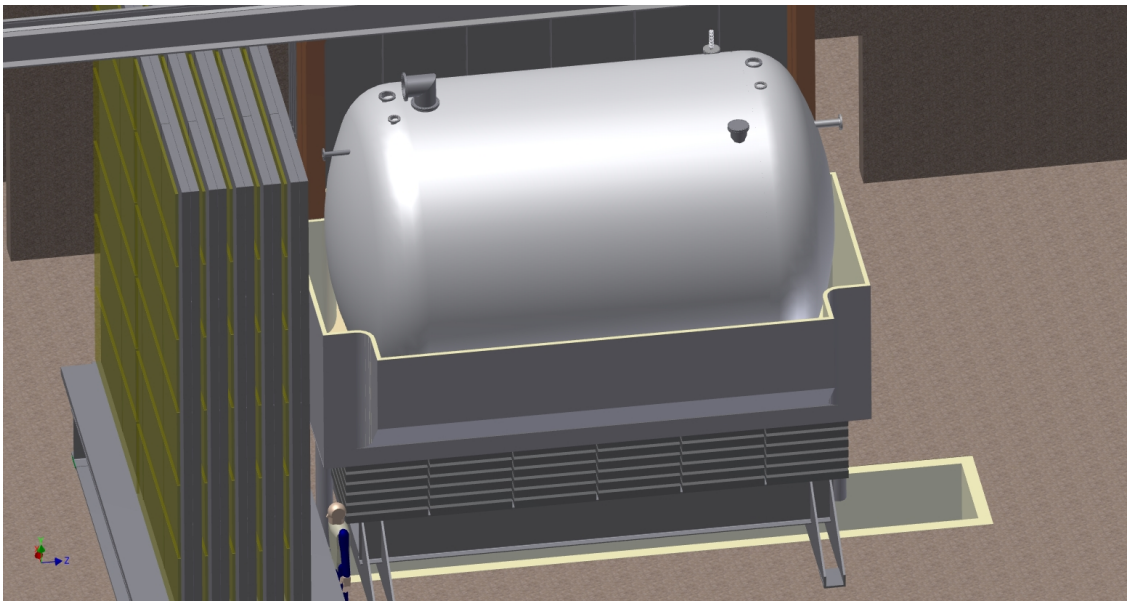

Figure 4–8: Drawing of the LArTPCT with MuID. The detector is shown with the magnet coils retracted. The downstream MuID is on the left in this view. The side MuID is interspersed in the magnet steel below and around the TPC.

The dimensions of the barrel and end scintillator planes will be 5 m × 6 m and 6 m × 6 m, respectively. The scintillator planes consist of layers of triangular scintillator bars, similar to those used in the MINERvA experiment [9], where each bar has a base width of 3.3 cm and a height of 1.74 cm. (No detailed design has been made yet; however, the narrow scintillator bars can accommodate many different geometries. To be conservative, the width of the barrel planes is assumed to be 5 m.)

The scintillator bars will be extruded at Fermilab with 0.7-mm diameter Kuraray wavelength-shifting (WLS) fibers fitted into a hole in the middle of the bars. The fibers will be read out by photosensors at each end. The scintillator position resolution of $\sim$ 5 mm matches well the deflection due to multiple scattering through 20 cm of steel: $y^{rms}_{plane} = 11.6$ mm for a 500-MeV/c muon and $y^{rms}_{plane} = 2.3$ mm for a 2500-MeV/c muon. There will be two scintillator planes for the upstream end of the magnet, corresponding to 2.4 interaction lengths, three scintillator planes for the barrel end of the magnet, corresponding to 3.6 interaction lengths, and five double-scintillator planes for the downstream end of the magnet, corresponding to 6.0 interaction lengths. In total this comes to 24 scintillator planes (ten planes at the downstream end, 2 planes at the upstream end, and 12 planes in the steel of the magnet). The total

Table 4–2: Specifications for the MuID

MuID Section	Scintillator Dimensions (cm^2)	Number of Planes	Interaction Lengths
Forward	600 x 600	10	6.0
Barrel	500 x 600	12	3.6
Backward	600 x 600	2	2.4

number of scintillator bars and electronics channels will be 8,000 and 16,000, respectively. Each channel will have a multi-hit time-to-digital converter (TDC) for measuring the time of the hits. A schematic drawing of the MuID interspersed in the magnet steel is shown in Figure 4–8, and the MuID specifications are given in Table 4–2.

A brief description of the MuID system fabrication is outlined below. First, the scintillator materials are mixed and extruded in the FermiLab NICADD facility to form isosceles triangular cross-sectioned bar scintillator stock of 3.3-cm base, 1.74-cm height, and up to the 5 or 6 meter lengths required. Similar to previous extrusions, the bars have a hole centered down the length for insertion of a wavelength-shifting fiber for readout, and are coated with Titanium Dioxide for light-tightness and light capture.

Second, the mechanical frames for the modules are procured. The modules are 5- or 6-m long by $\sim$ 1-m wide by $\sim$ 4-cm thick scintillator arrays. The long edges will fit into a "C" channel of aluminum side rails, and the short edges will fit to end caps supporting the optical coupling and readout electronics of MPPCs to the readout fibers at both ends of each scintillator. The side frames are longer than the scintillator to provide protection to the end pieces where the optical couplings are made. Attachment points are built into the side rails for placing and securing the completed modules in the magnet yokes or the end module assemblies.

Third, the Lexan or carbon fiber reinforced sheet for the modules are procured. The plastic sheets (0.1-cm thick) are glued to the face of planes of scintillator bars to provide a rigid, light-tight sandwich assembly for each module. Each sheet must be flat to specifications.

Fourth, the readout fiber and sensors for the scintillators are procured. The scintillators are readout via a Kuraray wavelength-shifting fiber inserted the length of the bar through a hole provided in the extrusion process, which is connected to a multi-pixel photon counter (MPPC) at each end. The MPPCs can be bought from Hamamatsu.

Fifth, the ferrules, shrouds, spacers, and springs for fiber termination are procured. The materials needed to complete the scintillator assembly and to make them optically functional will be bought from different sources in the US.

Next, individual planes are fabricated. A thin plastic membrane is laid out on a large flat tooling plate. On this a pre-cut sheet of Lexan or carbon fiber is laid out and registered with an alignment jig. Triangular scintillator bars are carefully glued to the sheet (e.g., using

Araldite 2011) and aligned with jigs. Care must be taken to prevent glue from entering the WLS holes. Using the triangular nature, up-pointing and down-pointing planes of triangular bars are interleaved and glued to each other to form a single plane with flat top and bottom faces. A layer of Lexan or carbon fiber sheet is glued to the upper surface. The glued assembly is âĂIJvacuum-baggedâĂİ using another thin sheet of plastic (to minimize the formation of bubbles and gaps as the glue sets) and allowed to cure for a few hours. After curing, the WLS fibers are inserted and glued to their ferrules. After this glue cures, all fibers are connected to a test readout system of MPPCs and electronics for testing with a sealed source, typically 137Cs. In this way damaged, fibers are located and replaced. Multiple planes (typically two) are stacked and aligned with aluminum side frames, where they fit into a "C"-channel, providing longitudinal rigidity and straightness. The two side frames are connected across the faces by transverse braces, providing rigidity and straightness in that dimension. The end frames consist of aluminum plates supporting the optical couplings and readout systems.

As each module is finished, the readout sensors, and front-end electronics are routed, hooked up, and tested. Each completed MuID module is then moved to a testing area. The electronics are connected to a well-characterized bench-test readout and analysis system. The counters are oriented to face the zenith to use the natural flux of cosmic-ray-induced muons in the module to measure and analyze the performance of each bar, MPPC, and front-end board comprising the module. QA criteria are checked and recorded.

4.2.8 Electronics and Data Acquisition

The electronics and data acquisition (DAQ) system shown in Figure 4–9 will be used for the MuID detector system. and is based on the electronics and DAQ design for the T2K near detector [5]. The electronics will receive signals from the photosensors, digitize and zero-suppress the data, and transmit the data to the DAQ system. The photosensor gain will be $\sim 10^5 - 10^6$ per photoelectron with a 1-1000 photoelectron dynamic range and a noise rate of 0.1 MHz at a 1.5 photoelectron threshold. The electronics are designed around the TRIP-t ASIC that was developed at Fermilab for use in MINERvA [9]. The TRIP-t ASIC is a 32-channel device that integrates and stores signals in a 48-channel-deep analog pipeline. Each channel has its own discriminator with a global programmable threshold, but only the outputs from 16 channels in parallel can be selected for output at any one time.

A picture of the T2K front-end board (TFB) is shown in Figure 4–10. Each TFB has four TRIP-t ASICs and reads out 64 signals. The TRIP-t ASICs are controlled by a Field Programmable Gate Array (FPGA), which runs at 100 MHz. Each discriminator signal is time-stamped with a resolution of 2.5 ns, and the integrated charges are measured with 14-bit ADC bandwidth on each channel. All charges above a programmable readout threshold are stored and sent to the back-end board (BEB), shown in Figure 4–11. The BEB collects the data from up to 48 TFBs and sends them to the DAQ over optical gigabit ethernet protocol.

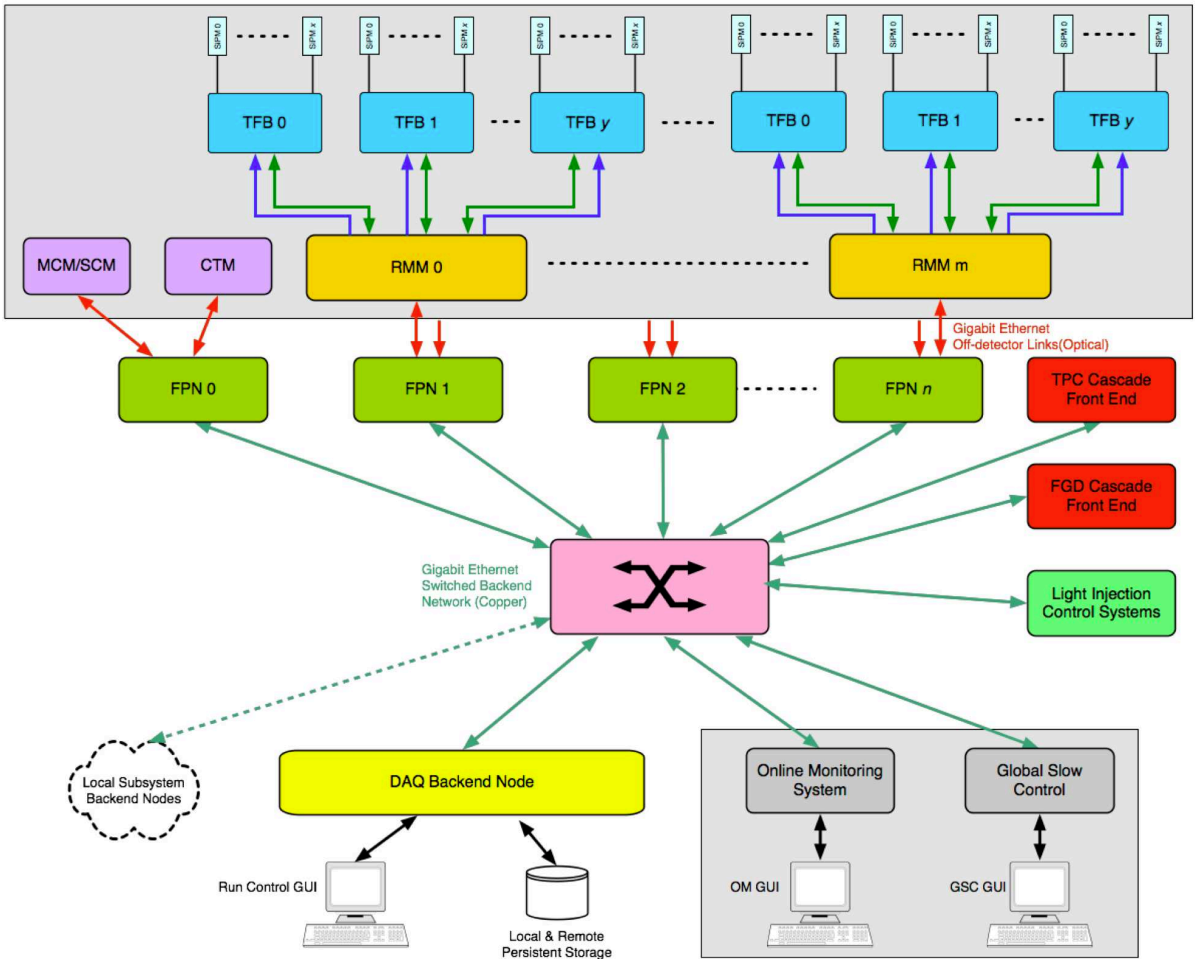

Figure 4–9: A schematic overview of the T2K electronics and DAQ system

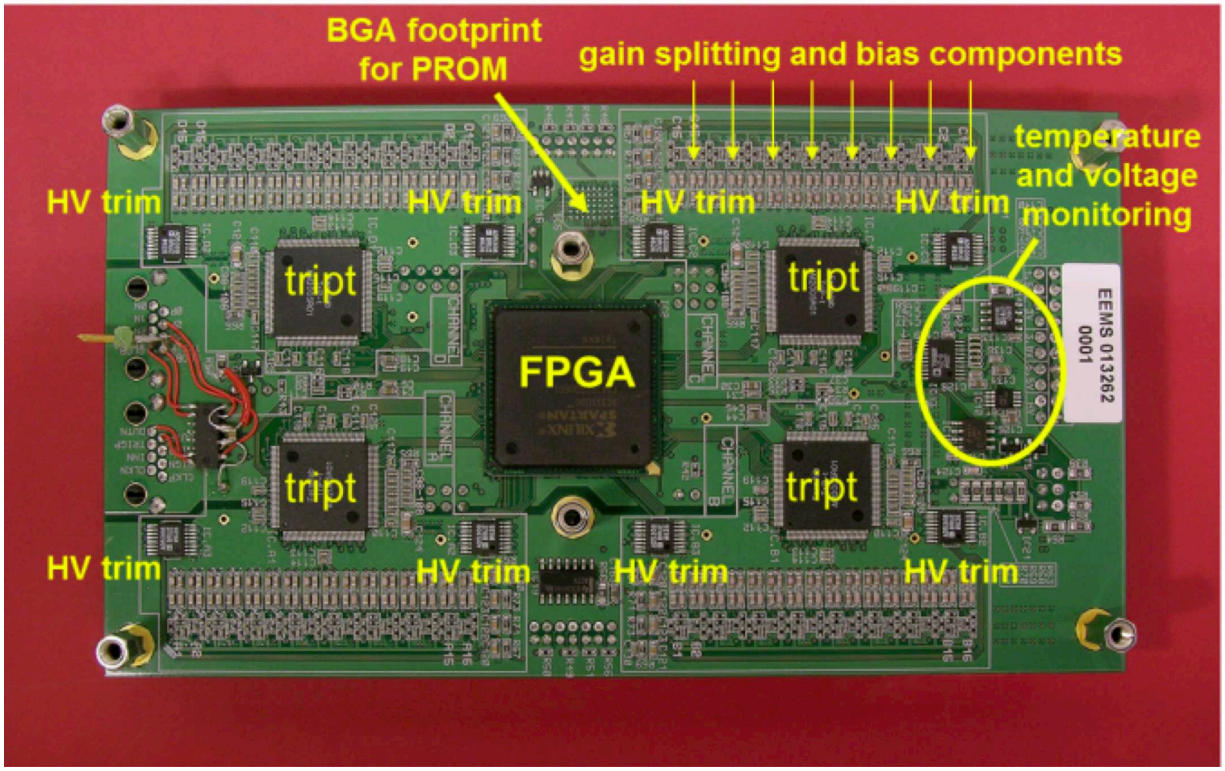

Figure 4–10: A photograph of the T2K front-end board (TFB) with labeling added

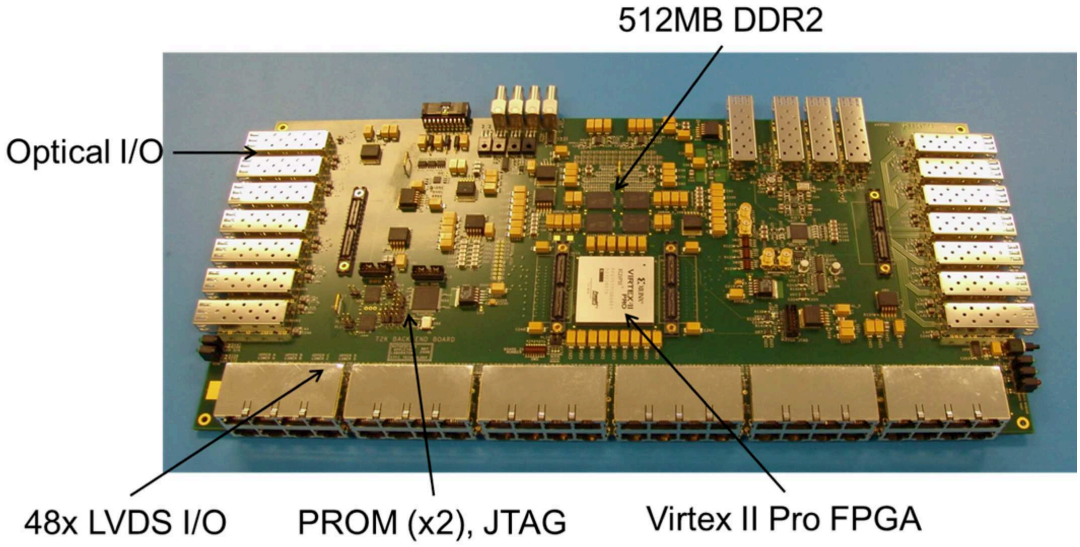

Figure 4–11: A photograph of the T2K back-end board (BEB) with labeling added

4.2.9 Assembly and Installation

The conceptual designs from MicroBooNE and LAr1/LAr40 are reused, including those for the TPC, cryostat, foam supports, cryogenics, HV, and DAQ. Additional conceptual design efforts are expected to be small (copying and scaling drawings, for example). The only completely new design is the LAr spill containment system. New or adapted preliminary designs are needed for the cryogenic plumbing, LAr spill containment and dump, and mechanical interface of the hard foam support to the magnet. The preliminary designs for other subsystems will already be available. Due to the dissimilarities of the installation, it is assumed that no final design work can be reused, even where existing conceptual and preliminary designs are reused.

The procurement and assembly model is based on that developed for MicroBooNE. The cryostat vessel will be purchased from a vendor and delivered on the vendor's truck. The parts for the TPC will be prepared, machined, cleaned, and readied for assembly at the participating universities and national labs. All parts will be quality inspected and approved for shipment by the TPC crew. All TPC parts will be stored at Fermilab in a clean and secure manner. Procurement of components for the TPC electronics will be done by the responsible laboratory. Liquid argon will be purchased from vendors and delivered by vendor's truck. The cryogenics system uses components commonly in use in low temperature systems everywhere, to be procured by the responsible lab (Fermilab), as informed by the experiences of ArgoNeuT, the Fermilab Liquid Argon Purity Demonstration (LAPD), and MicroBooNE.

The cryostat vessel will be delivered on the vendor's truck to an assembly building at Fermilab. Large tent structures similar to (or identical to) those used for MicroBooNE will be used for preparing the vessel and TPC and inserting the TPC into the vessel. A professional cleaning company will clean the vessel following the procedures successfully employed on the Fermilab Liquid Argon Purity Detector (LAPD) vessel. The TPC will be assembled and inspected in the clean tent area outside of the cryostat vessel. The finished TPC assembly will be inserted into the vessel with a cart. After all pre-closure testing procedures have been completed, the cryostat end cap will be positioned onto the vessel and attached. A dry gas purge will be used to protect the detectors until the vendor can weld on the end cap. A code certified contract welder will execute this task, perform the vessel pressure test, and administer the ASME 30.1 stamp of approval. The preceding assembly sequence is adapted from the MicroBooNE TDR, and will be adjusted if necessary according to MicroBooNE experience.

The fixed bottom part of the magnet will be assembled over the trough, and the foam saddles installed, prior to the arrival of the TPC detector (defined as the TPC assembly inside its cryostat). A professional off-site rigging crew will be contracted to relocate the assembled detector to the near detector hall using an appropriate truck and trailer. The detector will be lowered into the hall using the shaft crane, then moved into position using the hall crane. A contract insulation specialist will then apply the insulation to the detector.

Cryogenic system components that have been procured and inspected will be brought to the near detector enclosure, placed into their respective positions, secured, and connected. After the components have been positioned within and outside of the experimental hall, testing and safety inspection will be performed. After this, they will be connected to the cryogenic fluid supply vessels.

Racks of electronics made operational at the assembly building will be brought to the near detector hall and installed. Cables will be attached to the vessel and cable trays will be mounted for their runs from the vessel to the racks.

Appropriate testing procedures will be defined by the WBS managers to assure safety and quality of the assembled detector in accordance with Fermilab guidelines.

4.3 Alternative Design: Fine-Grained Tracker (WBS 130.03.04.03)

4.3.1 Introduction

The straw-tube fine-grained tracker (FGT) alternative design would measure the neutrino-event rates and cross sections on water and argon targets for both ν_e and ν_μ charged current (CC) and neutral current (NC) scattering events. Our FGT design is based on CERN's Neutrino Oscillation Magnetic Detector (NOMAD) [35] and will consist of a straw tube tracker (STT), water and argon targets, and an electromagnetic calorimeter inside of a dipole magnet. In addition, muon detectors (scintillator planes) will be embedded in the steel of the magnet. The FGT has excellent position and angular resolutions due to its lower-density ($\sim$ 0.1 g/cm^2) and high-precision STT. This high resolution is important for determining the neutrino vertex and determining whether the neutrino interaction occurs in the water or argon target. The proposed $2.5 \times 2.5 \times 4$ m^3 tracker will be positioned inside a dipole magnet with magnetic field, $B = 0.4$ T for particle tracking. The nominal fiducial volume corresponds to 2.5 tons of mass. A schematic drawing of the FGT concept is presented in Figure 4–12.

4.3.2 Requirements and Specifications

The FGT must measure the neutrino fluxes and the individual backgrounds at the near location so that these fluxes and event rates can be extrapolated to the far detector location. The backgrounds must be measured individually because different backgrounds have different extrapolations. Specific design considerations include the following. First, a straw-tube tracker (STT) with pressurized argon targets is chosen as the central tracker so that the neutrino cross sections and event rates are measured on argon and that the vertex resolution is sufficiently good (< 1 cm) to determine whether a track comes from the vertex (in the

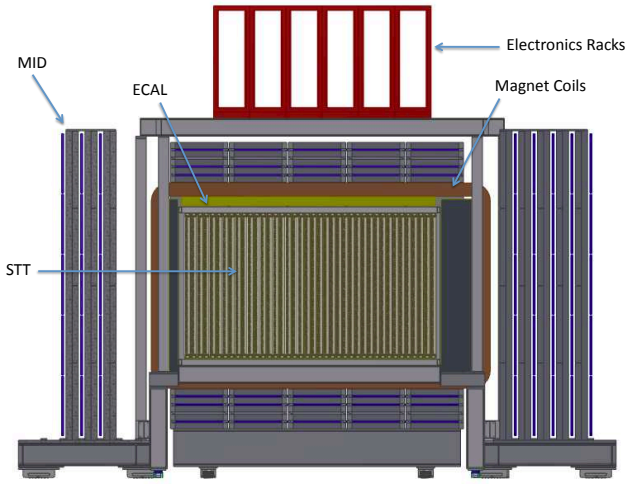

Figure 4–12: A schematic drawing of the FGT concept, including straw tubes, electromagnetic calorimeter, dipole magnet and muon-identifier detector

case of an electron) or is displaced from the vertex (in the case of a gamma). The STT also allows the reconstruction of the incident neutrino energy for CCQE events with good resolution in order to measure the neutrino fluxes as a function of energy and the reconstruction of neutral and charged pions produced in NC and CC scattering events. This is important because π^0 events constitute the largest background to ν_e and $\bar{\nu}_e$ appearance and π^+ and π^- events constitute the largest background to ν_μ and $\bar{\nu}_\mu$ disappearance. The electromagnetic calorimeter (ECAL), which surrounds the STT, is required to detect and identify gammas from neutrino interactions occurring outside the tracker. This ECAL also helps with the identification of gammas produced from neutrino interactions inside the tracker. The muon identifier detector (MuID) is required in order to fully identify muons and separate them from pions. Finally, a magnetic field is needed for the separation of neutrino and antineutrino events. Such a magnetic field also improves the identification of gammas through pair conversion, $\gamma \rightarrow e^+e^-$.

Table 4–3 lists the specifications for the FGT.

4.3.3 Straw Tube Tracker (WBS 130.03.04.02.01)

The straw-tube tracker (STT) is located at the center of the FGT and will be composed of straw tubes with an outer diameter of 19.4 mm. Vertical (YY) and horizontal (XX) planes of straws will be alternated and arranged in modules, with each module containing close-packed double straw layers of vertical and horizontal straws (XXYY). A carbon composite

Table 4–3: Specifications for the FGT

Item	Specification
Inner Magnetic Volume	3m x 3m x 5m
Tracking Detector	2.5m x 2.5m x 4m; 40 modules; 20,000 straws
Targets	10 x 1.27-cm thick water and argon targets
Transition Radiation Radiators	10 x 1.08-cm thick radiators
ECAL	X_0 = 9.8 barrel & 17.5 forward; 7680 scintillator bars
Dipole Magnet	0.4T; 1 MW; 60 cm thick steel
MuID	25 scintillator planes interspersed in magnet steel

sheet ($< 250\mu$m thick), as shown in Figure 4–13, will provide support for each plane of straws, while a carbon composite frame around the perimeter of the module will provide support for the wires under tension, as shown in Figure 4–14. The dimensions of each module will be approximately 250 cm $\times$ 250 cm $\times$ 10 cm.

Readout will occur from both ends of the straws to resolve ambiguities in the hit assignment. On the upstream side of each double module, there will be water or argon targets (for the upstream half of the tracker) and a set of plastic foils called "radiators" (for the downstream half of the tracker). The targets and radiators will constitute $\sim$ 82% of the mass of the tracker. The radiators, which are made mostly of carbon and and located in the downstream part of the tracker, will allow measurement of the transition radiation (TR), which will yield continuous identification of electrons through the tracking volume.

It is proposed to use a mixture of xenon (Xe) and carbon dioxide (CO_2) gas in the straw tubes to maximize the amount of transition radiation (TR), which will be used for electron identification. The straw tubes are run at a voltage of approximately 2 kV, and the straw tube material for both the inner (19.06-mm diameter) and outer (19.4-mm diameter) foils is Kapton 100HN (25 μm thick). The inner and outer foils are aluminum-laminated and coated with carbon during manufacturing to provide electrical conductivity. The two-foil design insulates the inner foil and provides mechanical rigidity to the straw tube. Each straw will have a 30-μm diameter gold-plated tungsten wire positioned in the center of the straw by spacers and end plugs.

There are a total of 20,000 straws, corresponding to 500 straws per module and 40 modules. Both ends of the straw tubes will be read out, so that the total number of electronics channels will be 40,000. Each channel will have two 8-bit TDCs and an 8-bit ADC. The total mass of the STT is approximately 2.5 tons, corresponding to an average density of 0.1. The thickness of the entire 4-m-long STT is about one radiation length.

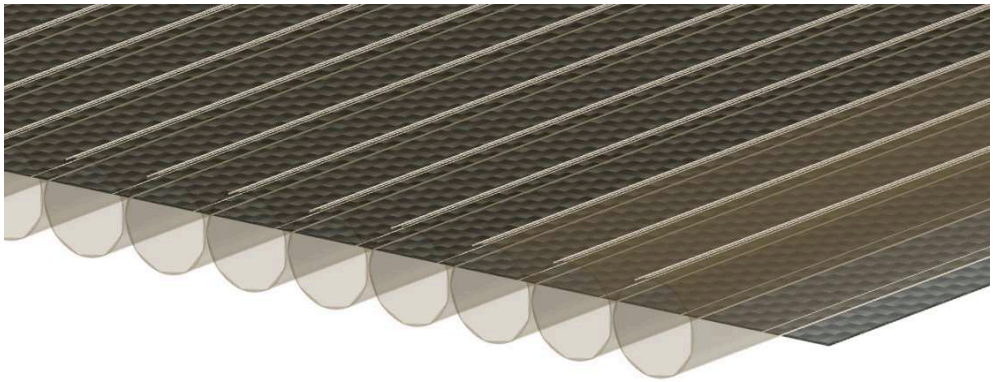

Figure 4–13: A schematic drawing of a plane of straw tubes that is glued to a carbon composite sheet

4.3.4 Radiator Targets

The radiators placed in the downstream half of the tracker will serve as a target for both neutrino interactions and TR production. Each radiator target is composed of 38 layers of 40-μm polypropylene $(C_3H_6)_n$ films alternating with 37 sheets of 250-μm tulle fabric spacers. The mass of each radiator is $\sim$ 2.2 kg and the thickness is $\sim$ 10.8 mm.

4.3.5 Water and Argon Targets

We will implement both water and argon as target materials for neutrino interactions. The targets will be positioned directly upstream of individual double modules without radiators. The targets, shown in Figure 4–15, will consist of ten planes of 0.5-in diameter, 2.5-m-long aluminum tubes filled either with water or with argon gas pressurized to 140 atm. We will place 195 tubes in each plane, spaced 0.505-in apart. The tube wall thickness will depend on the fill material; 0.065 in for the pressurized Ar and 0.028 in for water.

For the targets filled with water, half the targets can will be filled with H_2O and the other half with D_2O, so that the neutrino CCQE cross sections can be measured from both deuterium and oxygen. Also in this case, we may replace the water targets in the upstream region with graphite (C) and plastic (CH) targets in order to measure the antineutrino CCQE cross sections from hydrogen.

The density of Ar gas increases from 0.001662 at 1 atm to 0.233 at 140 atm, so the mass of Ar per plane is expected to be $\pi(0.00635)^2(2.5)(0.233)(195) = 0.014$ tons, yielding 0.14 tons for ten planes. For ten water planes the mass is quite a bit more, 0.62 tons. The total neutrino event rate will be $> 1 \times 10^6$ events/year for Ar and $> 6 \times 10^6$ events/year for water.

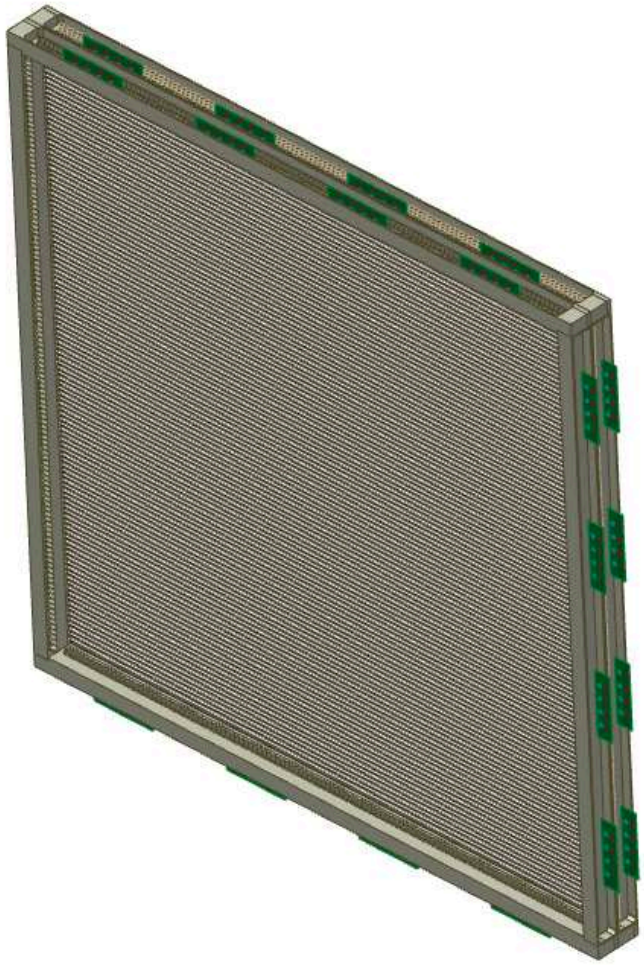

Figure 4–14: A schematic drawing of a straw tube tracker double module with its carbon composite frame

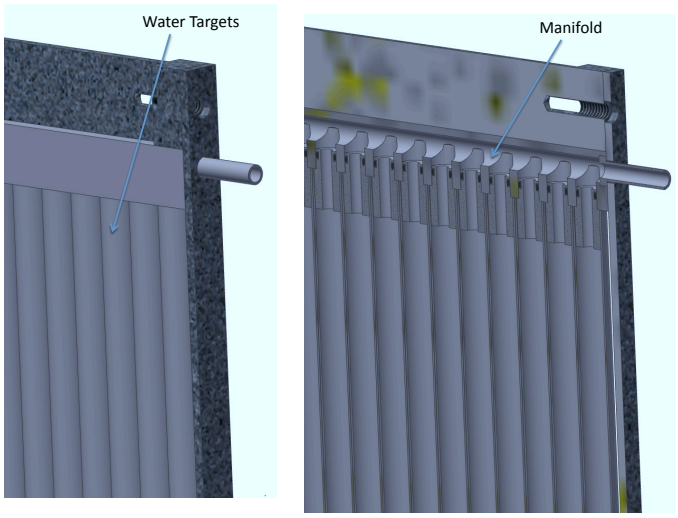

Figure 4–15: Schematic drawing of the water or pressurized-argon targets, made from 0.5-in diameter aluminum tubes

4.3.6 Electromagnetic Calorimeter (WBS 130.03.04.02.02.01)

An electromagnetic calorimeter (ECAL) will surround the tracking volume on all sides and consist of three separate pieces: Forward ECAL, Barrel ECAL, and Backward ECAL. Our ECAL conceptual design is based on the design of the T2K [5] ECAL and will consist of layers of 3-mm-thick lead sheets and 5-cm-wide by 5-mm-thick plastic scintillator bars, as shown in Figure 4–16. The scintillator layers alternate as XYXYXY... The Forward ECAL will consist of 33 layers of scintillator bars, where each bar has dimensions 3 m $\times$ 5 cm $\times$ 0.5 cm. The Backward ECAL will consist of 19 layers of scintillator bars, where each bar has the same dimensions, 3 m $\times$ 5 cm $\times$ 0.5 cm. The Barrel ECAL will also consist of 19 layers of scintillator bars, where each bar has different dimensions, 4 m $\times$ 5 cm $\times$ 0.5 cm. The total numbers of scintillator bars in the Forward, Backward, and Barrel ECAL are 1980, 1140, and 4560, respectively, with a total of 7680 bars.

The scintillator bars will be extruded at Fermilab with 0.7-mm-diameter Kuraray wavelength-shifting (WLS) fibers fitted in a hole in the middle of each bar, similar to those for the MuID. The fibers will be read out by photosensors at each end, making the number of readout channels twice the number of scintillator bars for a total of 15,360.

Candidate photosensors include metal-resistor-semiconductor avalanche photodiodes (MRS-APD) and multi-pixel photon counters (MPPC). Each channel will have two 8-bit TDCs and an 8-bit ADC. Overall, the forward ECAL will be 17.5 radiation lengths thick and the Barrel and Backward ECAL will be 9.8 radiation lengths thick. As shown in Figure 4–17,

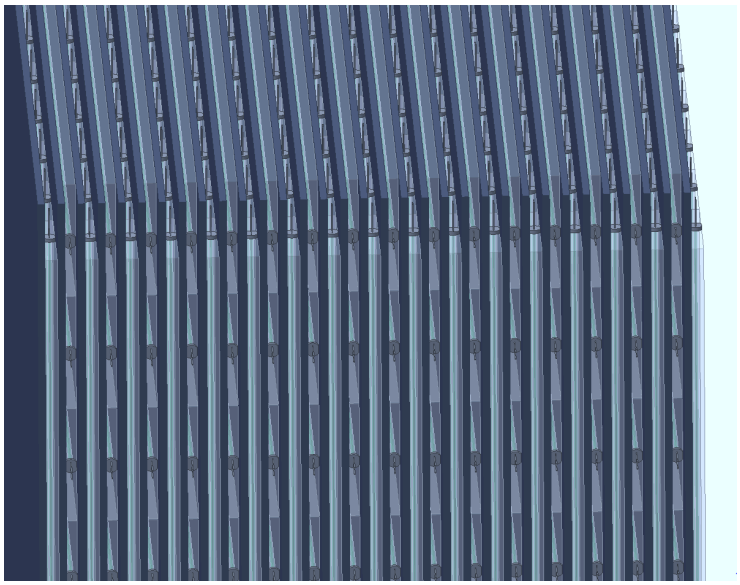

Figure 4–16: Schematic drawing of the ECAL, which is made up of alternating planes of plastic scintillator and Pb sheets

Table 4–4: Specifications for the ECAL

ECAL Section	Dimensions of Scintillator Bar (cm)	Lead Thickness	Number of Bars	Number of Radiation Lengths
Forward	300 x 5 x 0.5	3 mm	1980	17.5
Backward	300 x 5 x 0.5	3 mm	1140	9.8
Barrel	400 x 5 x 0.5	3 mm	4560	9.8

this means that the Forward ECAL should contain about 99% of the electromagnetic shower, while the Barrel and Backward ECAL should contain about 80% of the shower. Figure 4–18 shows that the ECAL should have an energy resolution of 10% or better for gamma energies > 1 GeV. The ECAL specifications are given in Table 4–4.

4.3.7 Dipole Magnet for the FGT (WBS 130.03.05)

The STT and ECAL modules will reside inside a 0.4-T dipole magnet for the measurement of particle momentum and charge. The magnet will have inner dimensions (inside the coils) 3-m wide $\times$ 3-m high $\times$ 5-m long. The magnet, as shown in Figure 4–19, is modeled after the CERN UA1 magnet [5] with vertically stacked Al coils producing a horizontal magnetic field. The thickness of the magnet steel will be 60 cm, consisting of six $\times$ 10-cm-thick plates. The magnet power requirement with Al coils is $\sim$ 2.4 MW, corresponding to 6 A at 400 V. The water flow required for cooling is 20 l/s.

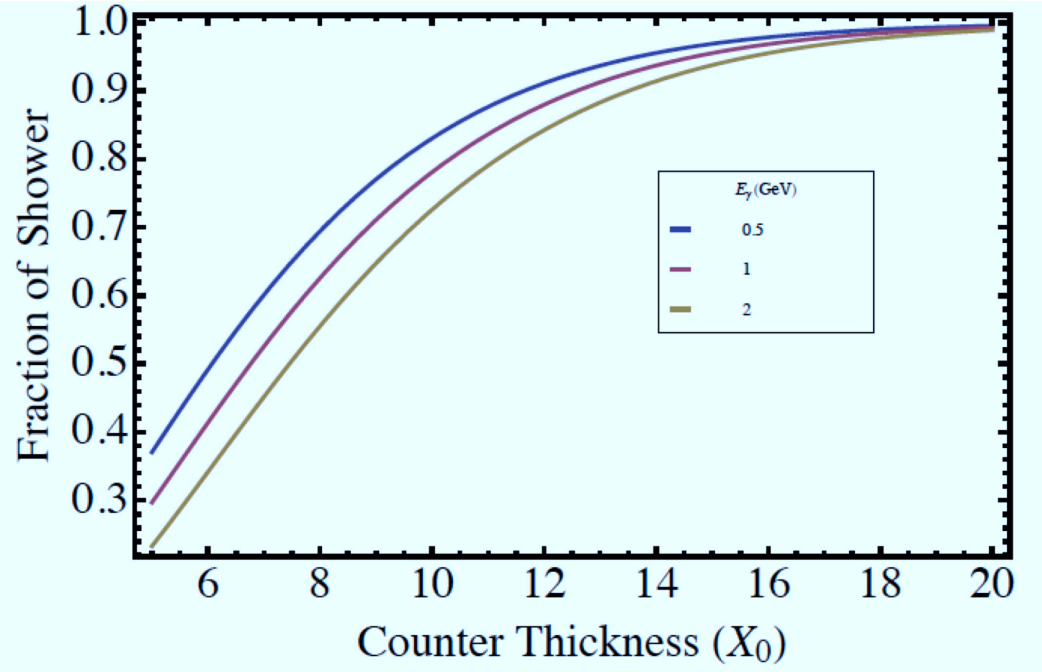

Figure 4–17: The fraction of the electromagnetic shower contained as a function of the ECAL thickness in radiation lengths

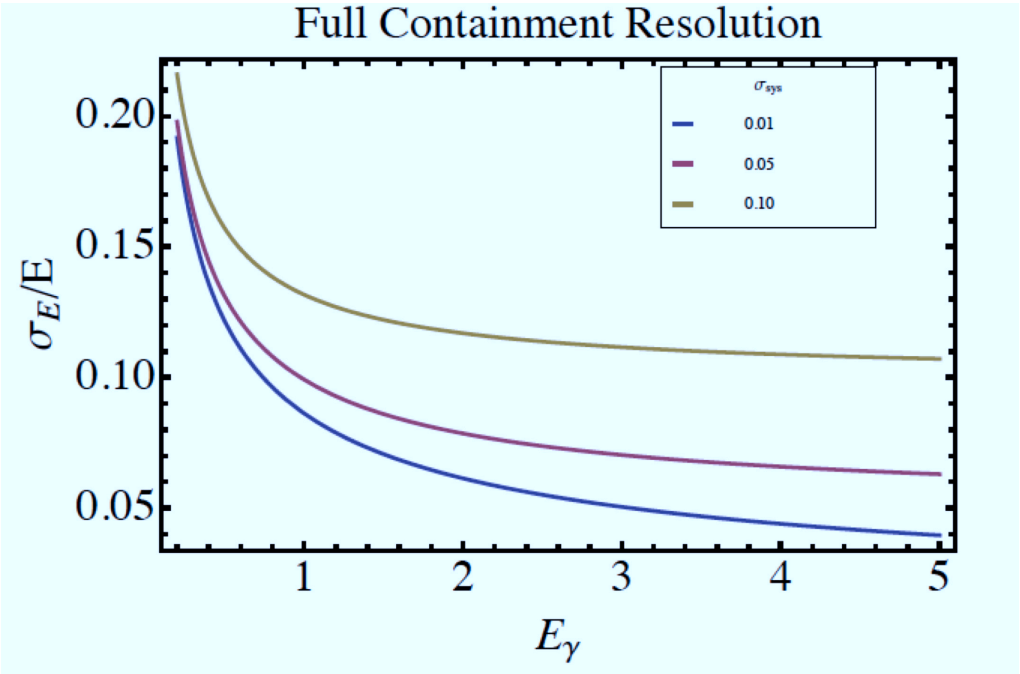

Figure 4–18: The ECAL energy resolution as a function of gamma energy for fully contained showers

The momentum resolution is dominated by multiple scattering in the STT. The momentum resolution is, therefore, given by $\delta p/p = 0.053/\sqrt{(LX_0)B}$. For B = 0.4T, L = 3m, and $X_0 = 4$m, the expected momentum resolution is $\sim 3.8\%$.

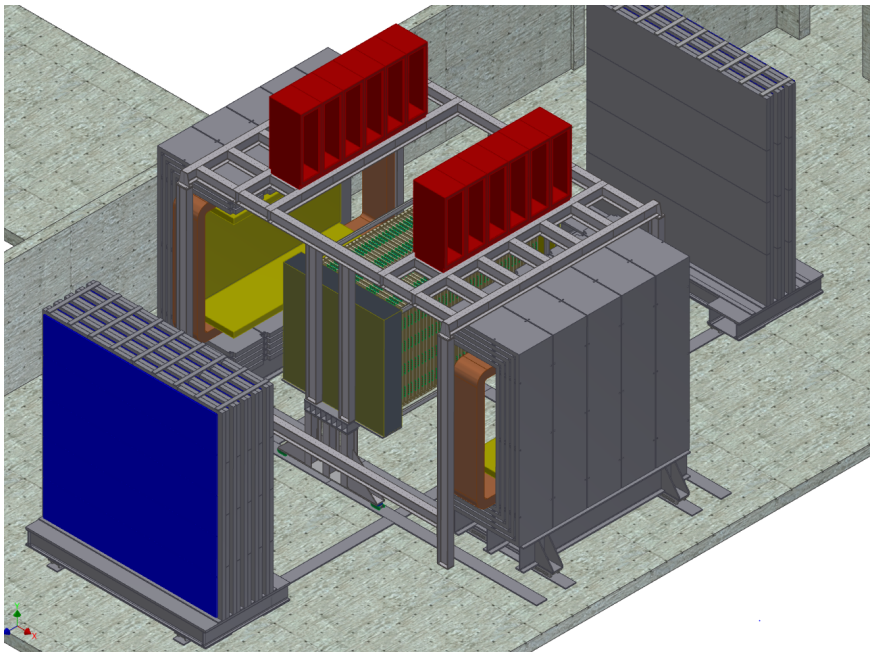

Figure 4–19: Schematic drawing of the FGT in the Near Detector Hall with the magnet opened up to show the STT, ECAL, and MuID

The magnet is discussed in more detail in Chapter 5.

4.3.8 MuID for the FGT (WBS 130.03.04.02.02.02)

The sides and ends of the dipole magnet will be instrumented with a muon identifier detector (MuID) for tracking particles from the neutrino-interaction vertex. The MuID will consist of inexpensive plastic-scintillator planes interspersed between 2 × 10-cm-thick steel plates of the dipole magnet and between 20-cm-thick steel plates at the upstream and downstream ends of the magnet. The MuID is only meant to provide identification of the muon; the muon momentum will be measured by the STT inside the magnetic field. A schematic drawing of the MuID is shown in Figure 4–20.

The dimensions of the barrel- and end-scintillator planes will be 4 m × 5 m and 5 m × 5 m, respectively. The scintillator planes consist of layers of triangular scintillator bars, similar to those used in the MINERvA experiment [9], where each bar has a base width of 3.3 cm and

Table 4–5: Specifications for the MuID

MuID Section	Scintillator Dimensions (cm^2)	Number of Planes	Interaction Lengths
Forward	500 x 500	10	6.0
Barrel	400 x 500	12	3.6
Backward	500 x 500	3	3.6

a height of 1.74 cm. (No detailed design has been made yet; however, the narrow scintillator bars can accommodate many different geometries. To be conservative, the width of the barrel planes is assumed to be 4 m.)

Again, the scintillator bars will be extruded at Fermilab with 0.7 mm diameter Kuraray wavelength-shifting (WLS) fibers fitted in a hole in the middle of each bar. The fibers will be read out by photosensors at each end. The scintillator position resolution of $\sim$ 5mm matches well the deflection due to multiple scattering through 20 cm of steel: $y^{rms}_{plane} = 578/p$ cm/MeV or $y^{rms}_{plane} = 11.6$mm for a 500 MeV/c muon and $y^{rms}_{plane} = 2.3$mm for a 2500 MeV/c muon.

There will be three layers of scintillators for the barrel and upstream end of the magnet, corresponding to 3.6 interaction lengths, and five double layers of scintillators for the downstream end of the magnet, corresponding to 6.0 interaction lengths. The total number of scintillator planes will be 25 (13 planes at the downstream and upstream ends and 12 planes around the barrel). The total number of scintillator bars and electronics channels will be 6848 and 13,696, respectively. Each channel will have a multi-hit time-to-digital converter (TDC) for measuring the time of the hits. A schematic drawing of the MuID interspersed in the magnet steel is shown in Figure 4–21, and the MuID specifications are given in Table 4–5.

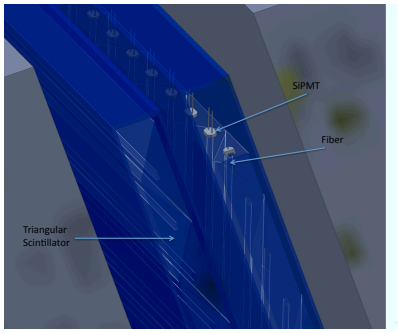

Figure 4–20: Schematic drawing of the MuID, consisting of triangles of plastic scintillator

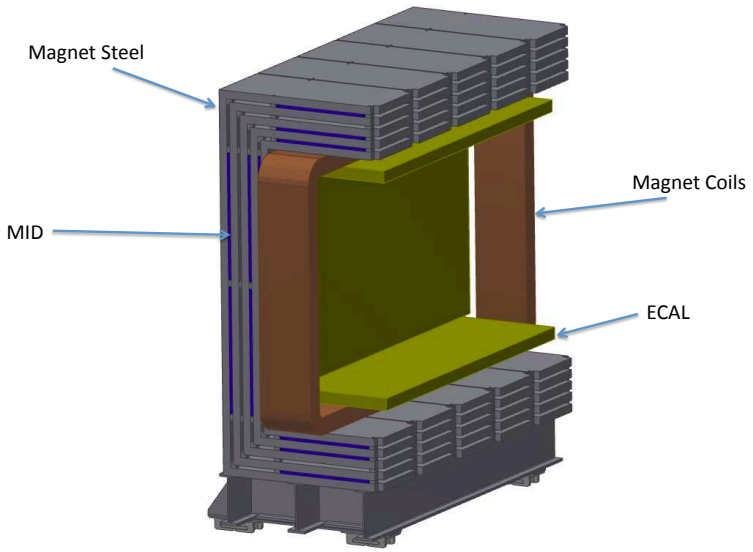

Figure 4–21: Schematic drawing of the MuID interspersed in the magnet steel

4.3.9 Electronics and Data Acquisition

The same basic electronics and data acquisition (DAQ) system, as shown in Figure 4–9, will be used for all three detector systems (STT, ECAL, and MuID) of the FGT and is based on the electronics and DAQ design for the T2K near detector [5]. The electronics will receive signals from the straw tubes or photosensors, digitize and zero-suppress the data, and transmit the data to the DAQ system. For the ECAL and MuID, the photosensor gain will be $\sim 10^5 - 10^6$ per photoelectron with a 1-1000 photoelectron dynamic range and a noise rate of 0.1 MHz at a 1.5 photoelectron threshold. The electronics are designed around the TRIP-t ASIC that was developed at Fermilab for use in MINERvA [9]. The TRIP-t ASIC is a 32-channel device that integrates and stores signals in a 48-channel-deep analog pipeline. Each channel has its own discriminator with a global programmable threshold, but only the outputs from 16 channels in parallel can be selected for output at any one time.

A picture of the T2K front-end board (TFB) is shown in Figure 4–10. Each TFB has four TRIP-t ASICs and reads out 64 signals. The TRIP-t ASICs are controlled by a Field Programmable Gate Array (FPGA), which runs at 100 MHz. Each discriminator signal is time-stamped with a resolution of 2.5 ns, and the integrated charges are measured with 14-bit ADC bandwidth on each channel. All charges above a programmable readout threshold are stored and sent to the back-end board (BEB), shown in Figure 4–11. The BEB collects the

data from up to 48 TFBs and sends them to the DAQ over optical gigabit ethernet protocol.

5 Near Detector Magnet (WBS 130.03.05)

5.1 Introduction

This chapter describes the conceptual design for the dipole magnet that will surround the Near Site neutrino detector (ND). It is based on the magnet that was developed for the CERN UA1 experiment and recycled for the T2K experiment [5]. The magnet is intended to provide a 0.4-T horizontal magnetic field and thus enable the measurement of particle momentum and charge.

5.2 Design Considerations

To enable the neutrino detector to accomplish its primary purposes, namely determination of the beam flux at the Near Site and the measurement of ν_e-appearance backgrounds, a magnetic field is required within the detection volume to measure the momentum and charge-sign of the reaction products μ, e, π, and p, from neutral current (NC), charged current (CC) and charged current quasi-elastic (CCQE) interactions. Electron and positron momentum measurements are also important for characterization of the neutral-current π^0 background. A magnetic field of 0.4 T over the length of the tracker is sufficient to allow for the determination of the charge-sign of the muons.

5.3 Overview of the Magnet used as Design Basis

We have chosen a dipole magnet candidate design based on the large-aperture UA1 magnet. This magnet design is well known, having been reused on the NOMAD and T2K experiments [5]. A photograph of the UA1 magnet yoke is shown in Figure 5–1.

The UA1 magnet consists of two halves that are mirror-symmetric about the vertical plane containing the beam axis. This magnet consists of eight C-shaped steel flux-return yokes

Figure 5–1: UA1 Magnet steel return yokes

and four magnet coils. The four coils provide a very uniform field in the magnetic volume. The external dimensions of the magnet are 7.6 m long by 6.1 m high by 5.6 m wide. The internal measurements (in the same order) are 7.6 m by 3.6 m by 3.5 m and the total weight of the yoke is 850 tons. Figure 5–2 is an illustration showing the two halves of the magnet separated with the internal coils visible. The magnet would have been in this position only during assembly of the inner detectors; during normal operation the two halves would have been in contact. The coils consist of aluminum conductors of square cross-section, 54.5 mm $\times$ 54.5 mm. The configuration of the UA1 magnet coils, shown in Figure 5–3, provided a uniform horizontal field orthogonal to the beam axis. The UA1 magnet was designed to operate with a current of 10 kA, providing a field of 0.67 T, with a power consumption of 6 MW.

5.4 The ND Magnet Reference Design

5.4.1 Magnet Parameters

A UA1-style magnet for the neutrino-detector reference design, the LArTPCT, will be made up of two halves that each consist of six C-shaped yokes made of low-carbon steel plates. The external dimensions of the magnet are designed to be 6.1 m wide by 6.5 m high by

Figure 5–2: A schematic of the UA1 magnet, as used in the T2K experiment, but shown in the opened position. Interior components shown in brown, grey and green are coils. The exterior C-shapes in red and blue are magnet yokes. Both assemblies are shown on rollers and rails.

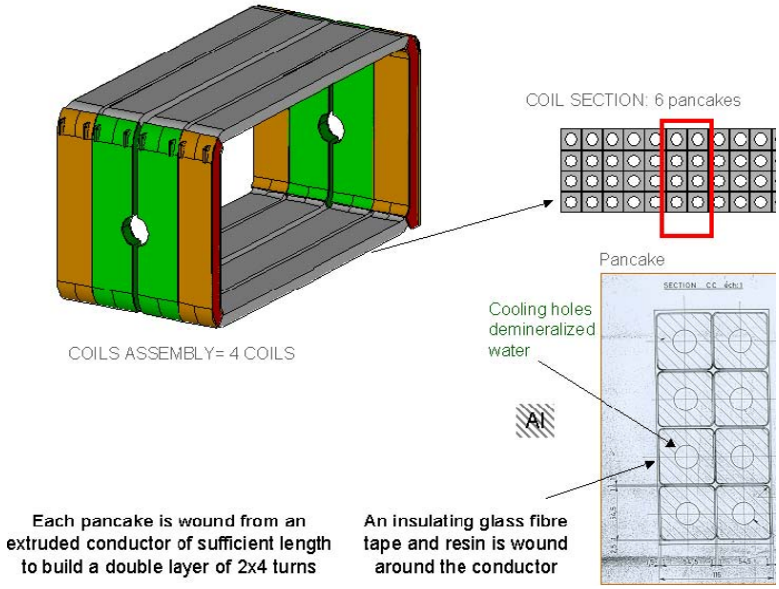

Figure 5–3: The UA1 magnet Coils; the coils are made of six double pancakes, each pancake consisting of eight 54.5 mm $\times$ 54.5 mm aluminum turns

6 m long, with an aperture of $4 \times 4 \times 6$ m^3. The conceptual design for this magnet consists of coil packages identical to the UA1 design, but with only two coils, rather than the UA1 magnet's four. This simplifies the support-structure design of the tracker and electromagnetic calorimeter (ECAL) subsystems. However, it decreases the field uniformity in the magnet volume while increasing the current density in the coils. Use of an accurate field map is likely to mitigate the effects of a nonlinear field but the increase in current density may be a problem. A recent calculation of the field of the ND magnet design is shown in Figure 5–4 for a two-coil system and in Figure 5–5 for a four-coil system. The current density is 2.0 MA/m^2 for the four-coil package and 5.0 MA/m^2 for the two-coil package. These both represent the 2D field for one quarter of the magnet.

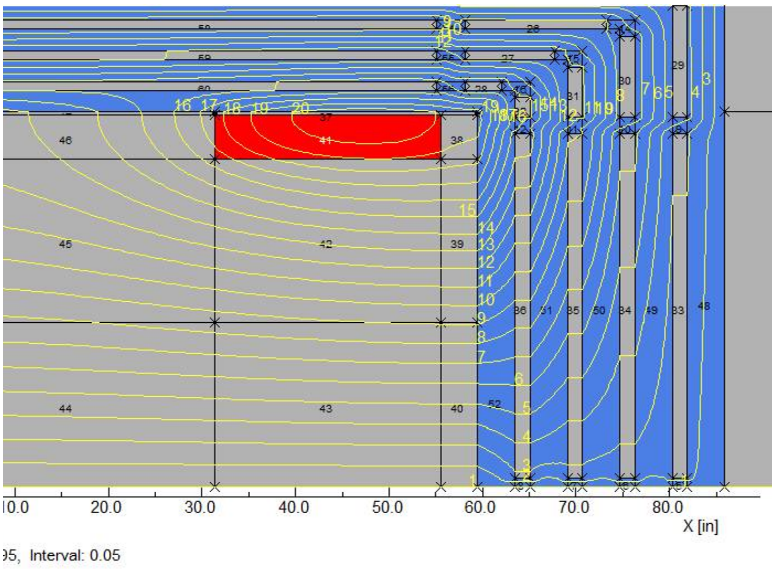

Figure 5–4: A recent calculation of the magnetic field of the ND magnet design for a two-coil system; the field uniformity is degraded from the the magnet with four coil packages

5.4.2 Magnet Configuration

In the reference design, the magnet coils and the LAr cryostat containing the TPC will sit inside the magnet, as shown in Figure 5–6. The magnet C-shaped yoke will be modified from the UA1 design to allow space for the support structure for the cryostat. Missing in the figure is the top piece of the magnet yoke.

The reference design will require two coils and magnet inner dimensions that will provide a larger inner magnet apperture than the UA1 magnet. albeit with a reduction of the number of spaces in the magnet steel. The spaces will be instrumented with scintillator planes for identifying muons; this will be the MuID system.

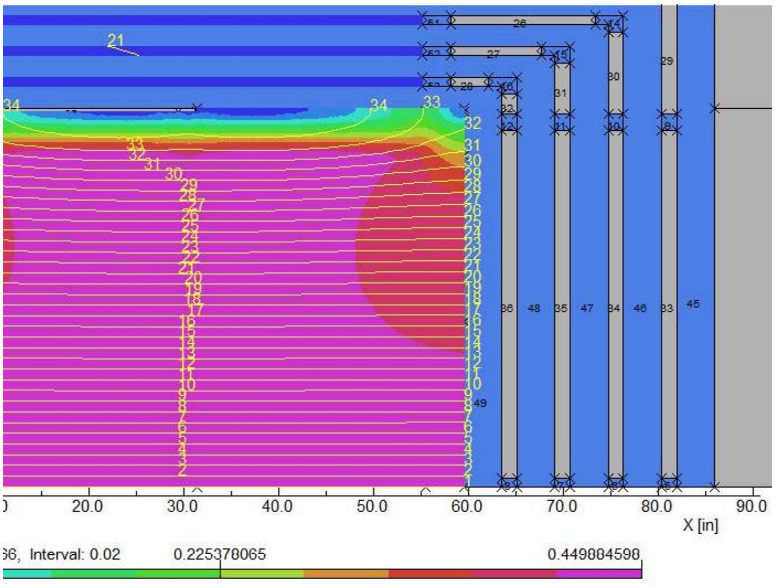

Figure 5–5: A recent calculation of the magnetic field of the ND magnet design for a four-coil system. The field uniformity in the bulk of the magnet is good to a few percent

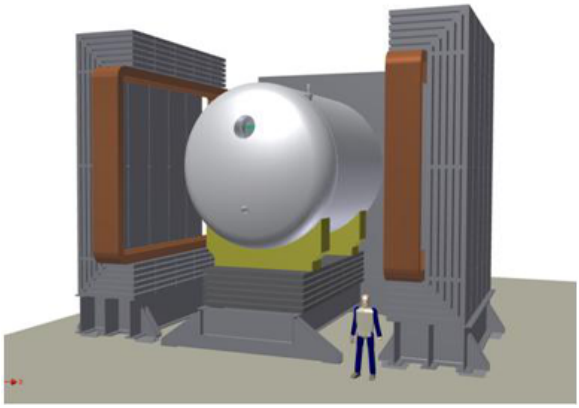

Figure 5–6: The LArTPCT magnet in the open position; LAr cryostat is shown as a cylinder in the center

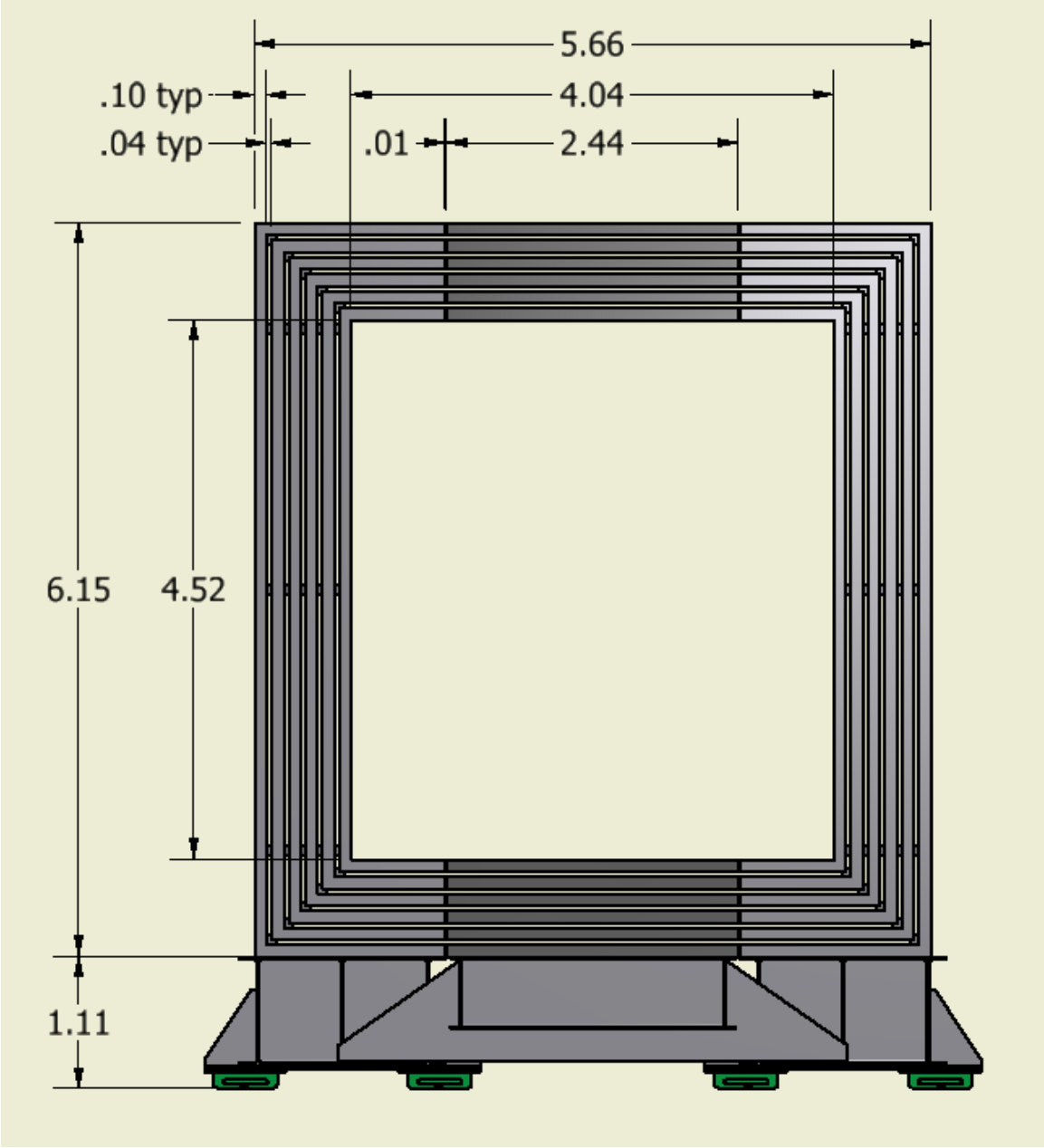

Figure 5–7: The LArTPCT magnet's yoke made up of six pairs of C-shaped component yokes; dimensions are shown in meters

Table 5–1: Parameters for the UA1, NOMAD, and T2K magnet systems

Magnet	Field	Power	Max Current	Voltage	Water Flux	Delta T
UA1	0.7 T	5500 kW	10.0 kA	555 V	50 L/s	30^oC
NOMAD	0.4 T	2400 kW	6.0 kA	400 V	20 L/s	30^oC
T2K	0.2 T	600 kW	3.3 kA	188 V	15 L/s	10^oC

The magnet will be mounted on rails (similar to that shown in Figure 5–2), providing support in both closed and open positions.

5.4.3 Cooling and Electrical Systems

The cooling and electrical systems will be designed to allow either flexible supply lines or removable connections when the magnet is opened.

5.5 Magnet Power Supply

The ND magnet power supply design is based on previous experience with the UA1 magnet. The power requirements for UA1, NOMAD and T2K magnets are summarized in Table 5–1.

6 Near Detector Global DAQ and Global Computing (WBS 130.03.06)

6.1 Introduction

The purpose of the Global Data Acquisition System (GDAQ) is to collect raw data from each detector system in the Near Detector Complex (NDC), issue global triggers, add timing data from a global position system (GPS), and build events. Each NDC detector has its own data acquisition system that connects to the GDAQ.

The GDAQ is made up of three parts: Master Global DAQ (M-GDAQ), Neutrino Global DAQ (N-GDAQ), which connects to the neutrino-measurement detectors (ND), and Beamline Global DAQ (B-GDAQ), which connects to the BLM.

The computing system encompasses two major activities: online computing (the required slow-control systems) and offline computing for further development of the measurement strategy and for simulation work on technical systems.

6.2 Global DAQ

6.2.1 Master Global DAQ

6.2.1.1 Introduction

The Master Global DAQ (M-GDAQ) is generally controlled by the LBNE Central Run Control to start and stop runs. It also has its own run control and event builder so that it can run independently of the LBNE Central Run Control, e.g. while the beam is off or for calibration or test runs. It communicates with the Neutrino GDAQ and Beamline GDAQ, and provides two-way trigger processing to and from the Near Detectors and beamline. Based

on the T2K Near Detector DAQ [36], the proposed system will use Gigabit Ethernet as the primary data-transfer medium.

The M-GDAQ incorporates a GPS system for precision time-stamping of beam spills and/or detector events and to provide clock and synchronization signals to the individual detector and beamline DAQs.

6.2.1.2 Design Considerations

The detailed M-GDAQ requirements will have to be developed and specified over time once details of each Near Site subdetector have been established. The M-GDAQ will need to provide typical DAQ functions including triggering, event-building, data monitoring, transfer, storage, logging, and so on. The general system requirements of the M-GDAQ can be found in the NDC requirements documentation [11].

In addition, the M-GDAQ will need to allow standalone data-taking of individual detector DAQs for debugging or calibration, and allow secure remote access, storage and monitoring capability via firewall to LBNE collaboration member institutions.

6.2.1.3 Reference Design

The central component of the M-GDAQ is a computer array serving as the back-end for the Near Detector Complex GDAQ. It will be a scalable and flexible system that can be expanded or upgraded as needed and as computer technology improves over time. The actual quantity of computers needed for this system and their specifications will depend on the number of channels and expected data rates of the individual neutrino and beamline detectors, for which the details have not yet been finalized. Using the T2K Near-Detector DAQ experience as a reference, it is safe to assume that a Gigabit Ethernet structure is more than sufficient for the data transmissions between the LBNE Near Detectors and the GDAQ.

Figure 6–1 shows the conceptual design of the M-GDAQ based on a computer array connected with the N-GDAQ and B-GDAQ via Gigabit Ethernet and other components for triggering and clock synchronization. For starting and stopping runs the LBNE Central Run Control connects to the M-GDAQ via optical fiber. A GPS subsystem is an integral part of the M-GDAQ; it provides precision time stamps of each global-trigger event. As an option, the GPS timing data can be transferred to the LBNE Far Detector via a private network (fiber) link to allow real-time processing of LBNE beam data with Far Detector data – as it is done at T2K with T2K's beamline (and near detector) and Super–Kamiokande as T2K's Far Detector.

A specially designed Global Trigger electronics module processes beam-spill trigger(s) coming

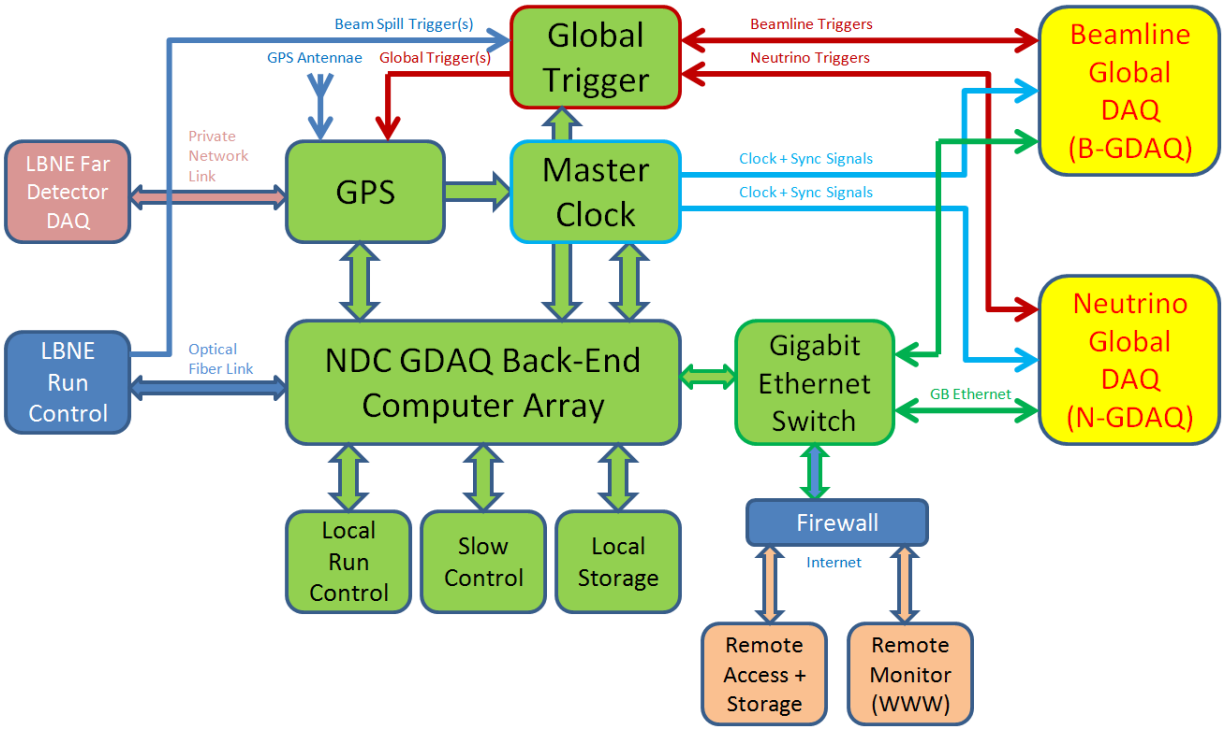

Figure 6–1: Near Detector Master Global DAQ (M-GDAQ) block diagram. The green and yellow blocks belong to the whole GDAQ. Green blocks are part of the M-GDAQ only, while the yellow blocks summarize the N-GDAQ and B-GDAQ. Other colored blocks are not part of the GDAQ, but shown here for presenting the connections between the GDAQ and other parts of the LBNE project.

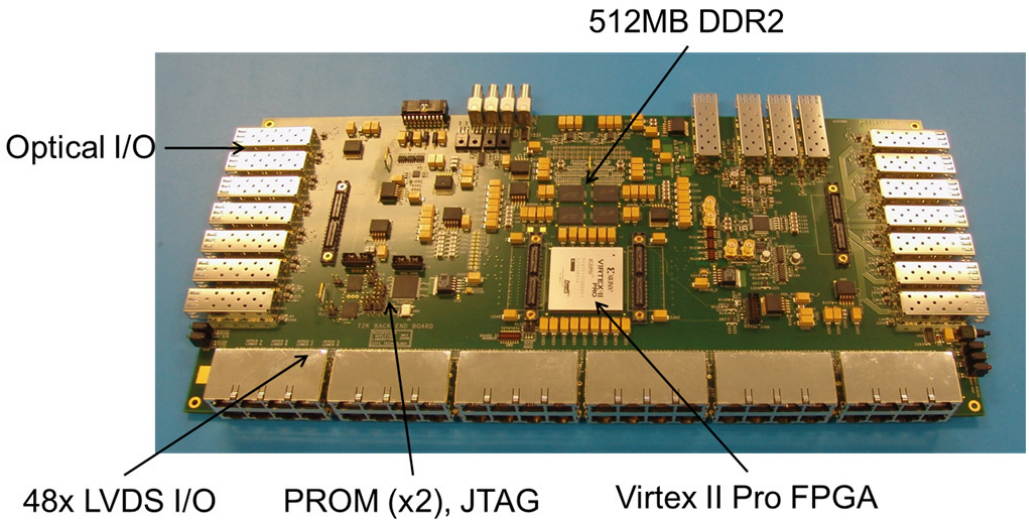

Figure 6–2: DAQ back-end module designed for T2K ND280, allowing four selectable functions via FPGA firmware

both from the LBNE central run control and from the beamline and neutrino GDAQs, then provides a global trigger for the GPS system. Then, depending on settings either from the M-GDAQ local run control or LBNE Central Run Control, it sends back trigger signals to the N-GDAQ and B-GDAQ. The Master Clock module, another specially designed electronics module, provides clock- and time-synchronization signals generated by the GPS system and forwards them to the N-GDAQ and B-GDAQ systems. These two special electronics modules can be made of commercial components based on Field Programmable Gate Arrays (FPGA) that can be programmed with high functional complexity and flexibility. For example, the T2K UK group designed and built a universal back-end board for the ND280 DAQ, shown in Figure 6–2, that used a Xilinx Virtex-II FPGA as its central smart-electronics component. The FPGA firmware was written such that the back-end board could be configured for four selectable functions: master clock, slave clock, global or cosmic trigger, and readout merger.

The M-GDAQ back-end computer array collects and sorts the detector data coming from the N-GDAQ and B-GDAQ, then builds the event, includes time stamps from the GPS, formats the event, then saves the result to local storage, e.g., disk arrays.

A local run-control option is added to the M-GDAQ to allow independent detector runs when the LBNE Central Run Control is not being used, e.g., when the beam is off for maintenance or repair or when detector calibration runs are scheduled. The local run-control system will consist of three or four desktop workstations with monitors and keyboards that can also be used for (near) real-time event displays of several detector sections and online data-processing and monitoring.

Slow-control electronics is included in the M-GDAQ with environmental sensors (temperature, humidity, etc.) to monitor the surroundings and status of the DAQ electronics.

Finally, a firewall between the M-GDAQ network and outside world allows remote access, monitoring and offline data storage of the GDAQ online system by LBNE collaboration institutes.

6.2.2 Neutrino Global DAQ

6.2.2.1 Introduction

The Neutrino GDAQ (N-GDAQ) will communicate with the data-acquisition systems of each neutrino-detector system in the Near Detector Hall and manage the local trigger information. It will collect triggers from each of these detector systems and make some local-trigger decisions. It will also pass on global-trigger information from the M-GDAQ or higher levels to each detector system. The N-GDAQ will have its own run control to allow for calibration or other special runs without requiring interaction with the M-GDAQ or LBNE Central Run Control. It will also have the capacity to build events using detectors located in the Near

Detector Hall exclusively (i.e., the neutrino detectors).

6.2.2.2 Reference Design

Similar to the M-GDAQ subsystem, the N-GDAQ will mainly consist of a scalable back-end computer array, inter-connected to the individual neutrino-detector DAQs via Gigabit Ethernet, plus electronics modules for trigger-processing and clock synchronization, as shown in Figure 6–3. The quantity of computers required for the back-end system is highly dependent on the number of channels and expected data rates of the individual neutrino detectors. Based on the T2K Near Detector DAQ experience, one back-end computer should be able to handle approximately 3,000 channels for sustainable and continuous runs. Assuming a total of 180,000 channels for all neutrino detectors combined, for example, 60 back-end computers would be needed.

Trigger signals from each neutrino detector will be collected and pre-processed by a trigger-electronics module, similar in design to the global trigger or master-clock modules of the M-GDAQ setup. Depending on the run mode, this module could feed local-trigger decisions back to the detector DAQs for data collection, or it could forward global triggers to the neutrino-detector DAQs from the M-GDAQ or higher levels.

A slave-clock electronics module, similar to the master-clock module in the M-GDAQ setup, distributes clock- and time-synchronization signals from the M-GDAQ to all neutrino detectors.

The N-GDAQ is usually controlled by the M-GDAQ or LBNE Central Run Control. But it will also have its own local run-control setup, consisting of several desktop workstations with displays to allow independent local runs that include neutrino detectors exclusively. This is useful during detector commissioning, calibration runs, standalone cosmic runs and other runs where the beam is stopped or not needed. The N-GDAQ will include the capability for event building, formatting, local data storage, and real-time event- and process-monitoring displays.

6.2.3 Beamline Global DAQ

6.2.3.1 Introduction

Similar to the Neutrino GDAQ and neutrino detectors, the Beamline GDAQ (B-GDAQ) collects information from all the beamline-measurement detectors. It manages trigger information and has the capacity to determine when to issue triggers local to the beamline-measurement system. It also has two-way communication with the M-GDAQ regarding trigger information.

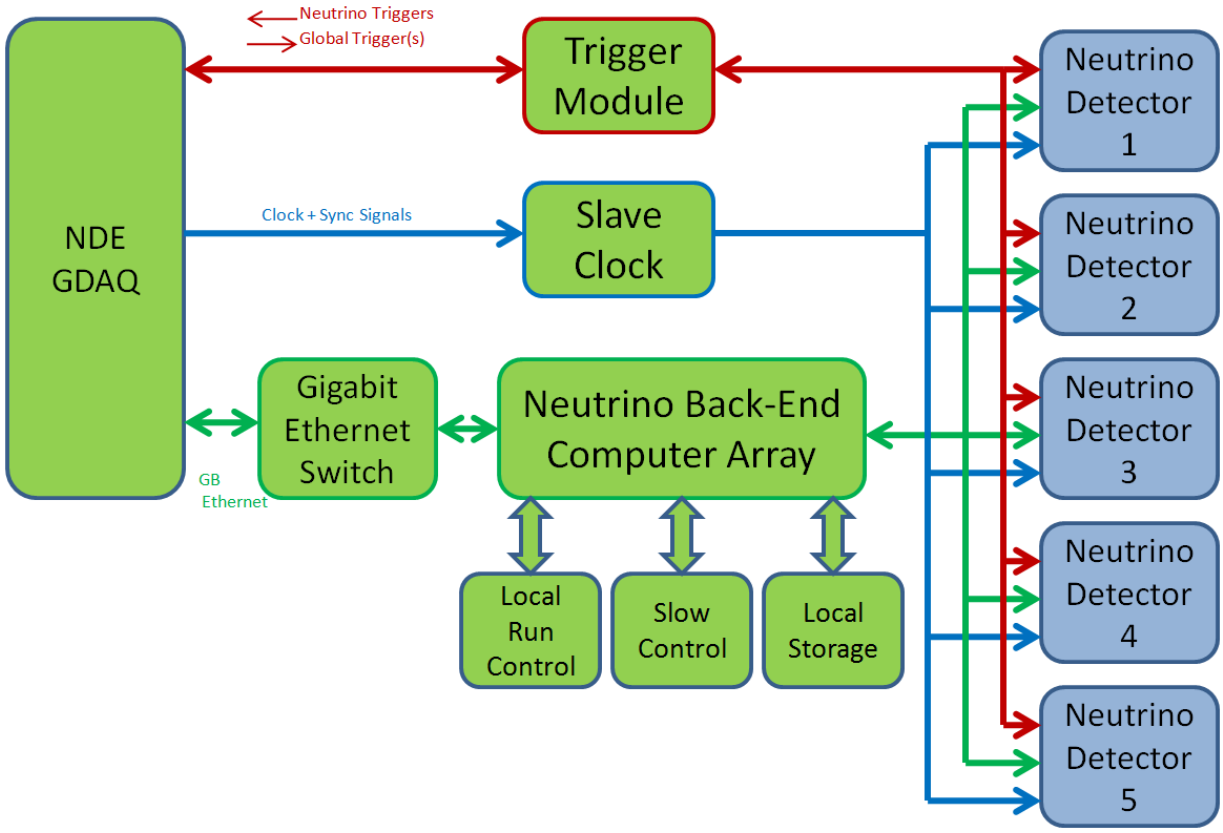

Figure 6–3: Neutrino Global DAQ (N-GDAQ) block diagram.

The B-GDAQ has its own run control and event builder to allow for runs that only include beamline detectors, and is illustrated in Figure 6–4.

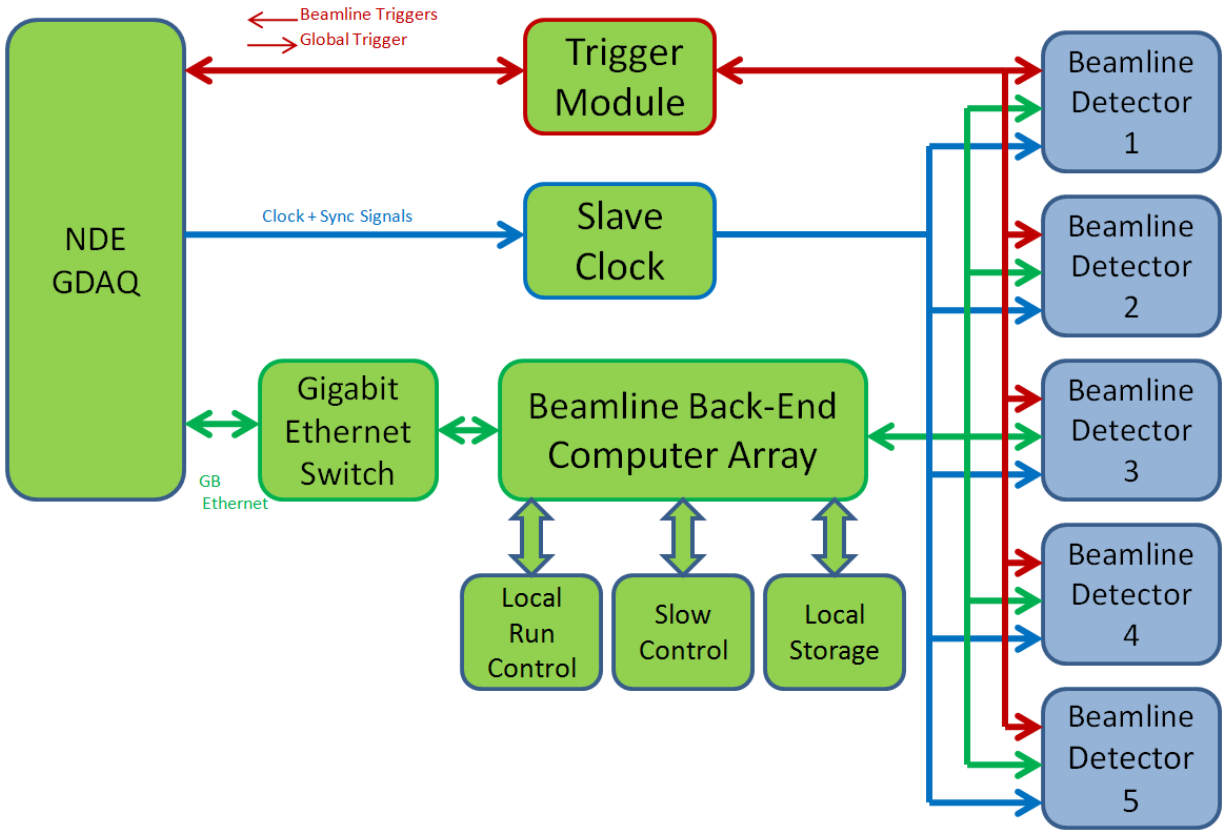

Figure 6–4: Beamline Global DAQ (B-GDAQ) block diagram.

6.2.3.2 Reference Design

The reference design of the B-GDAQ is identical to the N-GDAQ design, except that it is connected to the beamline-detector DAQs. As does the N-GDAQ, it consists of a back-end computer array with Gigabit Ethernet layer, and specialized electronics modules to process triggers from the beamline detectors, send back global triggers from the M-GDAQ to the beamline detectors, and distribute clock and synchronization signals. Again, a local run-control setup with its own event-building capability, data formatter, local storage and local event display and process-monitoring allows disconnection of the B-GDAQ from the

M-GDAQ or LBNE Central Run Control for standalone runs including beamline detectors exclusively.

6.3 Global Computing

The computing system encompasses two major activities: online computing (the required slow-control systems) and offline computing which is costed off-Project, but is important to consider. Offline computing is needed to complete the work outlined in the Measurement Strategy described in Chapter 2 and the simulation work for the technical systems.

The required slow-control (online) computing systems will be defined when the Project moves from the conceptual-design to the preliminary-design phase.

For offline computing, resources are currently being provided by Fermilab, LANL and various universities. Project-wide resources are currently being developed at Fermilab and Brookhaven.

References

[1] Particle Physics Project Prioritization Panel, "US Particle Physics: Scientific Opportunities; A Strategic Plan for the Next Ten Years," 2008. http://science.energy.gov/~/media/hep/pdf/files/pdfs/p5_report_06022008.pdf.

[2] LBNE Science Collaboration, LBNE Case Study Report, Liquid Argon TPC Far Detector, Draft Version 1.2, October 2, 2011.

[3] T. Akiri *et al.*, "The 2010 Interim Report of the Long-Baseline Neutrino Experiment Collaboration Physics Working Groups." arXiv:1110.6249.

[4] LBNE Project Office, "LBNE Project Management Plan," tech. rep., FNAL, 2011. LBNE Doc 2453.

[5] K. Abe *et al.*, "The T2K Experiment." arXiv:1106.1238 [phys.ins-det], 2011.

[6] http://www-numi.fnal.gov/.

[7] http://proj-cngs.web.cern.ch/proj-cngs/.

[8] http://www-boone.fnal.gov/.

[9] B. Osmanov, "MINERvA Detector: Description and Performance." arXiv:1109.2855 [hep-ex], 2011.

[10] UA1 Collaboration. http://library.web.cern.ch/library/archives/isad/isaua1.html.

[11] "Near Detectors Requirements Documentation," tech. rep. LBNE Doc 5579 http://lbne2-docdb.fnal.gov:8080/cgi-bin/ShowDocument?docid=5579.

[12] MINOS Collaboration, "Measurement of Neutrino Oscillations with the MINOS Detectors in the NuMI Beam," *Phys.Rev.Lett.*, no. 101:131802, 2008.

[13] D. Isenhower *et al.*, "Proposal to upgrade the MIPP experiment," *unpublished*, 2006. hep-ex/0609057.

[14] N. Abgrall *et al.*, "Measurements of Cross Sections and Charged Pion Spectra in Proton-Carbon Interactions at 31 GeV/c," *Phys.Rev.*, vol. C84, p. 034604, 2011.

[15] S. Kopp *et al.*, "Secondary beam monitors for the NuMI facility at FNAL," *Nucl. Instrum. Meth.*, vol. A568, pp. 503–519, 2006.

[16] M. H. Ahn *et al.*, "Measurement of Neutrino Oscillation by the K2K Experiment," *Phys. Rev.*, vol. D74, p. 072003, 2006.

[17] T. Maruyama, *First Observation of Accelerator Origin Neutrino Beam After Passing Through 250km of Earth.* PhD thesis, Tohuku University, 2000.

[18] K. Matsuoka *et al.*, "Development and production of the ionization chamber for the T2K muon monitor," *Nucl. Instrum. Meth.*, vol. A623, pp. 385–387, 2010.

[19] H. Kubo *et al.*, "Development of the muon beam monitor for the T2K Long Baseline Neutrino Oscillation experiment," *2008 IEEE Nuclear Science Symposium Proceedings*, pp. 2315–2318, 2008.

[20] D. Meier *et al.*, "Proton irradiation of CVD diamond detectors for high-luminosity experiments at the LHC," *Nucl. Instrum. Meth.*, vol. A426, p. 173, 1999.

[21] K. Hiraide, "Muon Monitoring Using the Decay Electrons," in *4th Workshop on Neutrino Beams and Instrumentation (NBI2003)*, 2003.

[22] Y. Semertzidis and F. Farley, "Effect of light flash on photocathodes," *Nucl. Instrum. Meth.*, vol. A394, p. 7, 1997.

[23] J. Ouyang and W. Earle, "Muon g-2 note no. 202," tech. rep., BNL, 1994.

[24] "GNUMI NuMI Beamline Simulation Code." `http://www.hep.utexas.edu/numi/beamMC/MC-code.html`.

[25] S. Agostinelli *et al.*, "GEANT4 — A Simulation Toolkit," *Nucl. Instrum. Methods*, vol. A, no. 506, pp. 250–303, 2003.

[26] R. Brun, F. Bruyant, M. Maire, A. C. McPherson, and P. Zanarini, "GEANT3." CERN-DD-EE-84-1.

[27] M. Catanesi *et al.*, "Measurement of the production cross-section of positive pions in p-Al collisions at 12.9-GeV/c," *Nucl.Phys.*, vol. B732, pp. 1–45, 2006.

[28] G. Ambrosini *et al.*, "Pion yield from 450-GeV/c protons on beryllium," *Phys.Lett.*, vol. B425, pp. 208–214, 1998.

[29] G. Zeller, "Expected Event Rates for an LBNE Near Detector at 459m." LBNE-doc-5337-v2, 2011.

[30] T. Katori, "MicroBooNE, A Liquid Argon Time Projection Chamber (LArTPC) Neutrino Experiment." arXiv:1107.5112 [hep-ex], 2011.

[31] A. Badertscher *New J. Phys.*, vol. 7, p. 63, 2005. arXiv:physics/0412080v1.

[32] B. Rebel, "LAPD Purge Results," tech. rep., FNAL, 2011. LBNE Doc 4380.

[33] C. Thorn, "LAr1 TPC Cold Electronics Design Summary." LBNE DocDB 4185-v4, 2011.

[34] C. Thorn, "LAr40 Cold Electronics Review." LBNE DocDB 5063-v3, 2011.

[35] J. Altegoer *et al.*, "The NOMAD experiment at the CERN SPS," *Nucl. Instrum. Meth.*, vol. A404, p. 96, 1998.

[36] M. Thorpe *et al.*, "The T2K Near Detector Data Acquisition Systems," *Real Time Conference (RT), 2010 17th IEEE-NPSS*, 2010.